2012

Potential drop and eddy current nondestructive evaluation problems

Yi Lu
Iowa State University

Potential drop and eddy current nondestructive evaluation problems

by

Yi Lu

A dissertation submitted to the graduate faculty

in partial fulfillment of the requirements for the degree of

DOCTOR OF PHILOSOPHY

Major: Electrical Engineering

Program of Study Committee:

John R. Bowler, Major Professor

Nicola Bowler

Jiming Song

Gary Tuttle

Jaeyoun Kim

Iowa State University

Ames, Iowa

2012

DEDICATION

I would like to dedicate this dissertation to my husband Sa Li without whose support I would not have been able to complete this work. I would also like to thank my family and friends for their loving guidance and assistance during the writing of this work.

TABLE OF CONTENTS

LIST OF TABLES

LIST OF FIGURES

ABSTRACT

Potential Drop (PD) and Eddy Current Testing (ECT) are two common Non-Destructive Evaluation (NDE) methods, which have been used for decades. The modeling research of these problems can help in designing and improving testing technologies, explaining inspection results, and even making the more complex problem solvable, like inverse analysis of flaws and cracks in ECT and case-hardening problem with alternating current potential drop (ACPD). In this dissertation, extensive theoretical modeling research work has been developed.

For direct current potential drop (DCPD) problems, first, an analytical solution of modeling edge effects of metal plates with finite thickness has been presented. When dealing with plates somewhat thicker than the probe dimensions, a method-of-images is applied with fast convergence. For thinner ones, a Fourier series summation method, which is obtained using expressions originally developed to evaluate lattice sums in solid-state physics, can overcome traditional slow convergence problem and effectively reduce the triple infinite summation that results from the method-of-images to a double one.

Next, an analytical model of DCPD on uniformly layered conductive cylinders of finite length is developed. The solution is expressed in terms of a Green's function, which satisfies Neumann boundary conditions, and can be extended to a conductive cylinder with an arbitrary number of uniform layers, like the common case-hardening problems. This model can be used to determine the thickness or the conductivity of layered cylinders, especially helpful in monitoring wall thickness in power or chemical plants due to its high sensitivity to the thin tube thickness.

For ECT problems, first, an analytical model of an axisymmetric eddy current ferrite-cored coil above a multi-layered conductive half-space is presented by radially truncating the domain of the problem. In this work, the reflection and transmission coefficient matrices due to the end effects of the ferrite core have been introduced, then by using a recursion relationship, the reflection coefficient of a conductor with an arbitrary number of uniform layers has been

determined. Furthermore, this approach can be extended to other axisymmetric ferrite core shapes, such as U-shape and E-shape. It is also possible to extend this approach to 3D problems in Cartesian coordinates using a double truncated series.

Then, a semi-analytical model of a differential bobbin coil impedance variation due to a common coaxial circular tube support plate has been developed. Within a truncated domain, the magnetic vector potential can be represented by a Fourier series and the effect of the tube support plate is evaluated theoretically. The close-form expression of the magnetic vector potential in a tube is critical for the more complicated 3D model for a support plate problem with a flaw or crack in the adjacent tube.

CHAPTER 1. GENERAL INTRODUCTION

1.1 Introduction

Non-Destructive Testing (NDT) is an interdisciplinary field consisting of a wide group of measurement and analysis techniques used in research and industry to characterize the properties of materials, tissues and structures without causing any damage to them. The common methods include ultrasonic, radiographic, acoustic, thermographic, electromagnetic, visual inspection and etc, which can be used to inspect the interior or characterize subsurface structures and contribute a lot in different applications, like manufacturing process control, oil pipeline, structure health monitoring.

1.2 Four-point Potential Drop Measurements

Four-point potential drop (PD) measurements are widely used in the field of NDT to characterize electrical conductivity or resistivity of of materials, determine the surface crack sizing or the depth of a long surface crack, monitor changes in the condition of metals due to heat treatments or the variation of tube wall thickness due to corrosion in plant or chemical plants. Furthermore, a new microscale Hall effect measurement method for fast characterization of the semiconductor thin film using colinear four-point probes has been developed. Recently, microscopic measurements have become possible with the advent of micron scale probes for the study of local material property variations.

In a common type of four-point probe, the current is passed through a specimen via a pair of spring-loaded pins while the potential drop is measured between a second pair of pin electrodes. The electrodes are often co-linear or can be placed at the corners of a rectangle. For any arrangement, the effect of contact resistance is minimized by connecting the voltage pick-

up pins to a relatively high impedance instrument to measure the potential drop accurately. Often, although not necessarily, the probe points are arranged in a straight line as shown in Figure 1.1. Generally, the current is injected and extracted via the outer two pins (P_1 and P_2) and the floating potential drop is measured across the inner two pins (Q_1 and Q_2) with a high input impedance circuit. Although most measurements use direct current (DC), tests can also be performed by injecting alternating current (AC) at selected frequencies and the observations can be analyzed with theoretical predictions of the time harmonic potential. In addition, the modeling work for the four-point probe potential drop with the transient current injected has been analyzed. Since the measured signal is inversely proportional to the conductivity, a good signal-to-noise ratio can be guaranteed for low-conductivity materials, for instance, in the semiconductor industry to determine the surface resistivity of semiconductor wafers. Besides, compared with other measurement methods such as the eddy current technology, PD can be applied to determine the conductivity and permeability of ferrous metals since both parameters are completely decoupled in the quasi-static regime which is very important and useful in measurements.

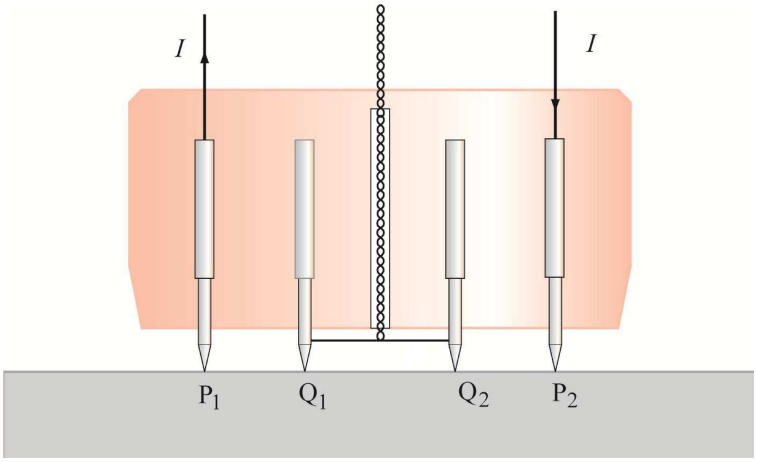

Figure 1.1 Co-linear four-point probe in contact with a conducting test-piece.

For the purpose of modelling the edge effect in four-point DCPD measurements on metal plates, several approaches have been brought forward. A solution via conformal transformation assumes that the specimen is thin compared to the probe spacing. An analytical solution of the Poisson equation (1) does not restrict the thickness of the specimen, but the form

of the solution is complex and the convergence of the solution is poor for thick samples. A conventional method-of-images solution yields a simple and elegant solution form, but generally converges slowly if at least one dimension of the specimen is small relative to the probe pin spacing. To improve upon numerical calculation of slowly converging infinite summations, Uhlir (2) evaluated some auxiliary functions and tabulated the potentials of several simple image systems. Hence, to establish an accurate theoretical model for the edge effect in DCPD with fast convergence, which can overcome the above restriction, is meaningful.

Using alternating current potential drop (ACPD) measurements to determine the case depth of induction-hardened steel rod is a very interesting and challenging topic and there are some related and preliminary studies given recently (3; 4). It is a critical and necessary step to solve this problem to derive the analytical expression of four-point DCPD on a uniform layered metal cylinder first. In addition, since the DCPD method has the advantage of being independent of magnetic permeability of the conductor, it is suitable for the measurements on ferrous tubes or layered rods. Besides, this method is very sensitive to the variation of the thin tube thickness and it can be used to determine the wall thickness in power or chemical plants.

1.3 Eddy Current Testing

Eddy current testing (ECT) is one of most popular NDT methods, which is applied to detect cracks or flaws and make measurements for conducting materials. ECT can help characterize a wide group of conducting material conditions, like defects, composition, hardness, conductivity, thickness, and etc. Generally, the ECT instruments are very portable, minimum efforts are required to set up the inspection, even for complex shapes and sizes of test piece, and immediate results can be given, so it widely applied in materials, nuclear, petroleum, aerospace and manufacturing process.

The basic principle of ECT is that when a coil excited by an alternating current is placed in proximity to a conducting test piece, the changing magnetic field generated by the coil can induce eddy current in the test specimen. Variations in the conductor, such as electrical conductivity, magnetic permeability or the presence of cracks or corrosions, will change the induced eddy current and then affect the impedance of the coil correspondingly. A typical

ECT application is as shown in Figure 1.2, in which an air-cored coil of rectangular cross-section above a conducting plate with a surface-breaking crack.

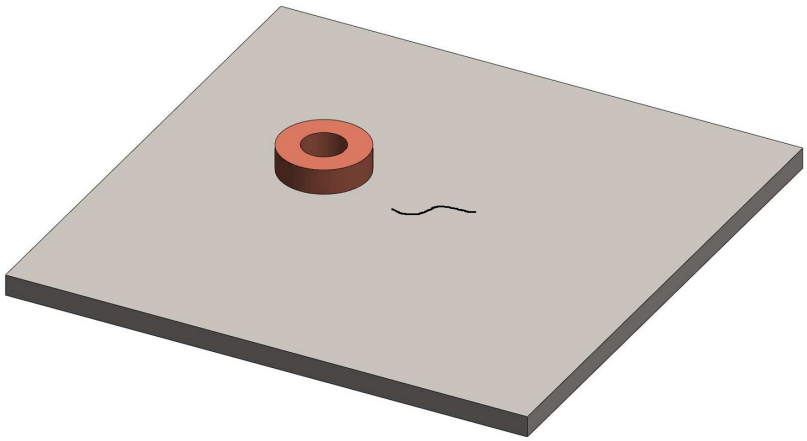

Figure 1.2 An air-cored coil above a conductive plate in the present of crack.

An air-cored coil above a multi-layered conducting half-space has been studied extensively due to the fact that the coil characteristics are relative easy to predict theoretically and measurements can be readily interpreted in terms of a well known model. A ferrite core in an eddy current probe usually improves the signal-to-noise ratio and resolution of defect detection, especially at a relatively low working frequency. Compared with air-cored probes, the ferrite cored probe usually has a better performance, particular for the detection and characterization of deep surface flaws. Although there are a number of numerical methods available to predict ferrite-cored probe fields, it is of great value to have instead an accurate analytical or semi-analytical method for finding the field and impedance of such probes, especially one that is relatively simple and easy to implement.

The problem of calculating eddy current probe signals of bobbin coils used for tube inspection has been studied extensively to simulate the testing heat exchangers. This is motivated by the use of numerical simulations to improve inspections and to aid in the interpretation of test data. Calculations can be time consuming if the numerical formulation leads to a large number of unknowns but the computational cost can be greatly reduced by using semi-analytical methods. In particular, calculations of the response due to a flaw in a tube can be carried out efficiently using integral methods because one can derive an integral kernel for an infinite tube

problem, in which case, the flaw signal can be determined accurately, efficiently and quickly. If there is a tube support plate, the probe signals caused by it are usually larger than those due to cracks, and can mask the flaws signals, so, it is critical to isolate its effect during the inspection.

1.4 Dissertation Organization

This dissertation can be divided into two parts based on the types of nondestructive technologies: the direct current potential drop measurements are studied in Chapters 2 through 3 and eddy current technologies are developed in Chapter 4 through 5.

Chapter 2 presents an analytical solution of modelling edge effects in DCPD measurements on metal plates with finite thickness. A method-of-images solution converges quickly for plates somewhat thicker than the probe dimensions. A Fourier series summation, obtained using expressions originally developed to evaluate lattice sums in solid-state physics, converges more quickly for thinner plates and effectively reduces the triple infinite summation that results from the method-of-images to a double infinite summation. The work of this chapter focuses on DCPD measurements, from which the metal conductivity can be deduced. In Chapter 3, the steady state electric field due to direct current flowing via point contacts at the cylindrical surface of a uniformly layered conductive rod of finite length has been determined. Green's function satisfying Neumann boundary conditions is applied to derive the theory solution. And a group of four-point DCPD experiments are used to verify the theory solution, showing good agreements between the theory and experiment. These analytic solutions offer a nondestructive determination of the thickness or electrical conductivity of the layered cylinder if the other parameters are given. Further, if using more than four electrodes or connecting electrodes in different configurations, one can determine the thickness and conductivity at the same time.

Chapter 4 presents an analytical model of an axisymmetric eddy current ferrite-cored probe above a multi-layered conducting half-space using a procedure in which the domain of the problem is truncated radially. Reflection and transmission coefficient matrices due to the end effects of the ferrite core have been introduced. By using a recursion relationship we

have determined the reflection coefficient of a conductor with an arbitrary number of uniform layers. This relationship is used, together with the ferrite core probe model to predict probe impedances for a simple ferrite core probe above a multi-layered conductor. For multi-frequency modeling only the reflection matrix changes with frequency and therefore the calculations can be done efficiently. Furthermore, this approach can be extended to other axisymmetric ferrite core shapes, such as U-shape and E-shape. It is also possible to extend this approach to 3D problems in Cartesian coordinates using a double truncated series. In Chapter 5, a semi-analytical model of a differential bobbin coil impedance change due to a coaxial circular tube support plate has been developed. Within a truncated domain, the axial dependence of the magnetic vector potential can be represented by a Fourier series and the problem is solved to account for effects of the tube support plate in which the expansion coefficients in this series is found. The theoretical calculations show an excellent agreement with the numerical results of FEM. Besides, the close-form expression of the magnetic vector potential in a tube is critical for the more complicated 3D model for a support plate problem with a flaw or crack in the adjacent tube. The approach can be extended to model other similar symmetric structures, such as an internal or external groove in a tube.

1.5 References

[1] Yamashita M and Agu M 1984 Geometrical correction factor for semiconductor resistivity measurements by four-point probe method *Jpn. J. Appl. Phys.* **23** 1499–504

[2] Uhlir A 1955 The potentials of infinite systems of sources and numerical solutions of problems in semiconductor engineering *Bell Syst. Tech. J.* **34** 105–28

[3] Takeo F, Nakajima K, Baba T, Aonahata Y and Saka M 2004 Arrangement of probes for measuring case depth by means of four-point probes *Key Eng. Mater.* **270273** 82–8

[4] Bowler J R, Huang Y, Sun H, Brown J and Bowler N 2008 Alternating current potential-drop measurement of the depth of case hardening in steel rods *Meas. Sci. Technol.* **19** 075204

CHAPTER 2. EDGE EFFECTES IN FOUR-POINT DIRECT CURRENT POTENTIAL DROP MEASUREMENTS ON METAL PLATES

A paper published in *The Journal of Physics D: Applied Physics*

Yi Lu, Nicola Bowler, John R. Bowler and Yongqiang Huang

2.1 Abstract

Four-point direct current potential drop measurements are commonly used to measure the conductivity (or resistivity) of semiconductors and ferrous or non-ferrous metals. The measured electrical potential difference is often interpreted in terms of analytic expressions developed for large plates that are either 'thin' or 'thick' relative to the probe length. It is well-known that the presence of the back surface of a plate leads to a solution expressed in terms of an infinite series representing the current source and its images. This approach can be generalized to account for multiple surfaces in order to obtain a solution for a finite plate, but convergence of the series is poor when the plate dimensions are similar to or smaller than the separation of the current injection and extraction points. Here, Fourier series representations of the infinite sums are obtained. It is shown that the Fourier series converge with many fewer terms than the series obtained from image theory, for plates with dimensions similar to or smaller than the separation of the current injection and extraction points. Comparing calculated results for the potential drop obtained by a four-point probe centered on finite plates of varying dimension, with those for a probe in contact with a large (laterally-infinite) plate, estimates are given of the uncertainty due to edge effects in measurements on small plates interpreted using analytic formulas developed for large plates. It is also shown that these uncertainties due to edge effects are reduced, for a given plate size, if the probe pick-up points are moved closer to the current

injection points, rather than adopting the common arrangement in which the four probe points are equally spaced. Calculated values of direct current potential drop are compared with experimental data taken on aluminium and spring-steel plates of various sizes and excellent agreement is obtained.

2.2 Introduction

The direct current potential drop (DCPD) technique is widely used to characterize electrical conductivity (or resistivity) of materials in the semiconductor industry (1), in biomedical research (2) and in geophysical applications (3). Compared with other measurement methods such as eddy-current technology, DCPD can be applied to measure the conductivity of ferrous metals, being independent of magnetic permeability. For DCPD measurements, the four-point probe is one of the most common probe configurations used in practice. Often, although not necessarily, the probe points are arranged in a straight line as shown in Figure 2.1. Generally,

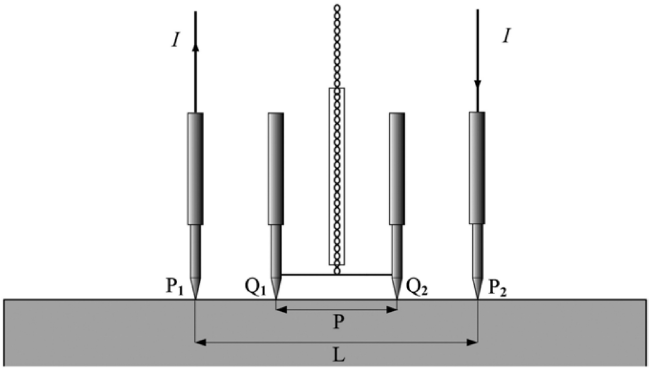

Figure 2.1 Co-linear four-point-probe in contact with a conductive test-piece. The pins are spring-loaded to ensure good electrical contact with the test-piece. Current is injected and extracted via the outer two pins. Floating potential difference is measured across the inner two pins.

the current is injected and extracted via the outer two pins (P_1 and P_2) and the floating potential drop is measured across the inner two pins (Q_1 and Q_2) with a high input impedance circuit. When the probe is sufficiently far from the boundary of the specimen (eight or nine times the probe length, to be shown here), the current distribution is not significantly disturbed by the specimen boundary. When the probe is close to the boundary, however, the current can

be significantly distorted which results in an increase in the measured potential drop. So, even for a homogeneous, uniformly-thick specimen, different voltages may be measured at different probe positions.

For the purpose of modelling the edge effect in four-point DCPD measurements, several approaches have been brought forward. A solution via conformal transformation (4; 5) assumes that the specimen is thin compared to the probe spacing. An analytical solution of the Poisson equation given in reference (5) does not restrict the thickness of the specimen, but the form of the solution is complex and the convergence of the solution is poor for thick samples. A conventional method-of-images solution (6) yields a simple and elegant solution form, but generally converges slowly if at least one dimension of the specimen is small relative to the probe pin spacing. To improve upon numerical calculation of slowly converging infinite summations, Uhlir (7) evaluated some auxiliary functions and tabulated the potentials of several simple image systems, for ease of reference.

This paper first establishes a theoretical model for the configuration in which the probe is close to one edge of a large plate with arbitrary thickness. In this case the test-piece has three bounding surfaces. Although the method of images gives a solution of simple form, it converges slowly for a plate thinner than the probe length. To overcome this disadvantage, a Fourier Series representation is established that gives much faster convergence for plates thinner than the probe dimension. Next, additional boundaries are considered and solutions given for a long plate of finite width (four bounding surfaces) and a plate that is finite in all three dimensions (six bounding surfaces). Comparison between theory and experiment on several aluminium and spring-steel plates of various sizes gives excellent agreement. Because measurements on 'thin' plates are commonly interpreted using analytic formulas that do not account for edge effects, estimates are given of the uncertainty due to edge effects in measurements on small plates interpreted using analytic formulas developed for large thin plates. Additionally, it is shown that these uncertainties are reduced, for a given plate size, if the probe pick-up points are moved closer to the current injection points, rather than adopting the common arrangement in which the four probe points are equally spaced.

2.3 Theory

The theoretical model presented here makes some assumptions. The current and voltage contacts are modelled as infinitesimal points on the specimen surface, which is assumed to be flat. In addition, the plate is assumed to be homogeneous and isotropic with linear material properties. These approximations are shown to be reasonable since the theory agrees well with experimental data, as shown later.

2.3.1 Half-space Conductor

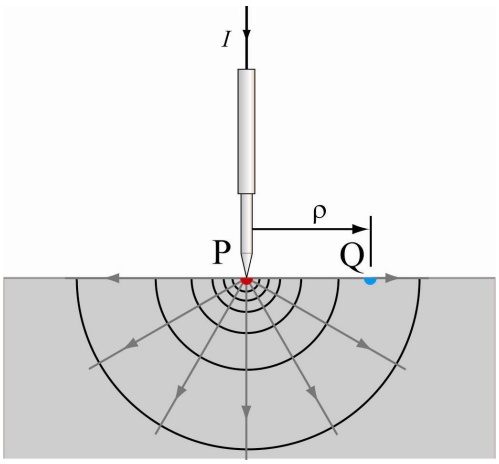

Figure 2.2 Injection of DC current at the surface of a half-space conductor.

First, consider the simple problem shown in Figure 2.2. Direct current I is injected into a half-space conductor at point P and diverges uniformly. This gives rise to the electric potential Φ for a point in the conductor given by

$$\Phi = \frac{I}{2\pi\sigma r}, \tag{2.1}$$

where σ is the conductivity of the test-piece and $r = \sqrt{(x-x')^2 + (y-y')^2 + (z-z')^2}$ is the distance from the injection point. Unprimed coordinates represent field points and the source coordinates are primed. Choosing the origin of the coordinate system at the surface of the conductor means that $z = z' = 0$ and $r = \rho = \sqrt{(x-x')^2 + (y-y')^2}$.

In a four-point probe problem, the potential at any one point on the surface of the test-piece results from the superposition of potentials due to both injected and extracted currents. So,

the potential of a field point Q due to a source of current at P_2 and a sink of current at P_1 on the surface is

$$\Phi(\rho) = \frac{I}{2\pi\sigma} f(\rho), \tag{2.2}$$

with

$$f(\rho) = \frac{1}{\rho_2} - \frac{1}{\rho_1}, \tag{2.3}$$

where $\rho_j = |\bar{Q} - \bar{P}_j| = \sqrt{\left(x - x'_j\right)^2 + \left(y - y'_j\right)^2}$ and $j = 1, 2$. In addition, the potential drop V between two points Q_1 and Q_2 on the surface of the specimen due to the current through P_1 and P_2, as shown in Figure 2.3, can be written with the general form

$$V = \Phi_{Q_2} - \Phi_{Q_1} = \frac{I}{2\pi\sigma} \left[f_2(\rho) - f_1(\rho) \right], \tag{2.4}$$

where

$$f_i(\rho) = \frac{1}{\rho_{i2}} - \frac{1}{\rho_{i1}}, \tag{2.5}$$

$\rho_{ij} = |\bar{Q}_i - \bar{P}_j| = \sqrt{\left(x_i - x'_j\right)^2 + \left(y_i - y'_j\right)^2}$ and $i, j = 1, 2$. Equation (2.4) provides a general form in which the potential drop V can be expressed for any test-piece geometry. The function $f(\rho)$ takes different geometry-dependent forms, with the form given in equation (2.3) for the conductive half-space being the simplest example.

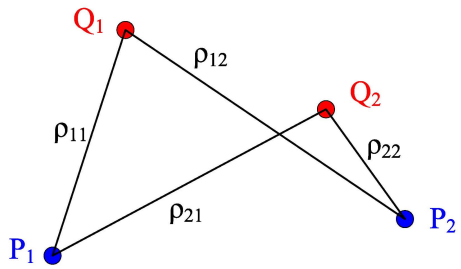

Figure 2.3 Contact points for current (P_i) and voltage (Q_i) electrodes on the surface of a planar specimen (plan view).

2.3.2 Finite Thickness Conductor

In the half-space problem, the potential due to a single injected current is given by equation (2.1), which satisfies the Von Neumann boundary condition $\partial\Phi/\partial z = 0$ on the surface

of the conductor, away from the current injection point. For a large plate of thickness $c/2$ whose upper surface is in the plane $z = 0$, Figure 2.4, there is a similar boundary condition at $z = -c/2$. The method of images is employed to satisfy the conditions on both of these surfaces.

Placing an image source at $z = -c$ of the same polarity as the actual source, yields two opposing currents whose z-components exactly balance in the $z = -c/2$ plane. Thus, with one image source added, the Von Neumann boundary condition at $z = -c/2$ is satisfied. But, the boundary condition at $z = 0$ is no longer satisfied because of the effect of the image source. This effect can be balanced by introducing another image source with the same polarity at $z = c$. In fact it is necessary to add images in this way in both positive and negative z-directions out to infinity. Finally, the images of a current source at P occupy positions with period c in the z-direction as shown in Figure 2.4.

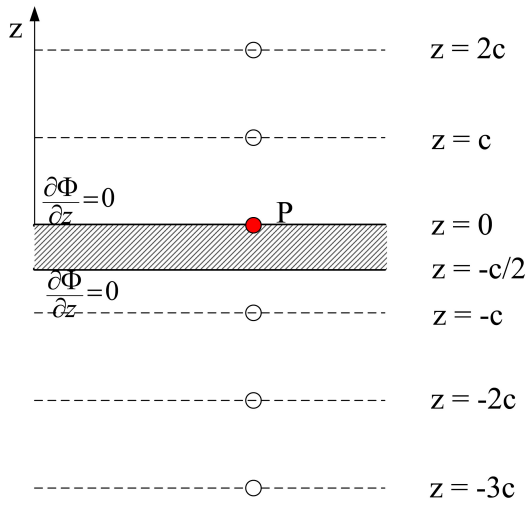

Figure 2.4 Current source at P and image sources (open circles) required to satisfy the interface conditions at the surfaces of a laterally-infinite conductive plate, here located at $z = 0$ and $z = -c/2$.

From the method of images, a source at P_2 and a sink at P_1 give rise to a potential at Q on the surface that is a generalization of equation (2.3);

$$f(\rho) = \sum_{n=-\infty}^{+\infty} \left[\frac{1}{\sqrt{\rho_2^2 + (nc)^2}} - \frac{1}{\sqrt{\rho_1^2 + (nc)^2}} \right]$$

$$= \frac{1}{\rho_2} - \frac{1}{\rho_1} + 2\sum_{n=1}^{+\infty}\left[\frac{1}{\sqrt{\rho_2^2 + (nc)^2}} - \frac{1}{\sqrt{\rho_1^2 + (nc)^2}}\right], \tag{2.6}$$

where $\rho_j = |\bar{Q} - \bar{P}_j| = \sqrt{\left(x - x'_j\right)^2 + \left(y - y'_j\right)^2}$, $j = 1, 2$ and the potential drop can be evaluated as in equation (2.4) where

$$f_i(\rho) = \sum_{n=-\infty}^{+\infty}\left[\frac{1}{\sqrt{\rho_{i2}^2 + (nc)^2}} - \frac{1}{\sqrt{\rho_{i1}^2 + (nc)^2}}\right] \tag{2.7}$$

should now replace (2.5) and $\rho_{ij} = |\bar{Q}_i - \bar{P}_j| = \sqrt{\left(x_i - x'_j\right)^2 + \left(y_i - y'_j\right)^2}$, $i, j = 1, 2$. Note, when $c \to \infty$ only the terms with $n = 0$ survive in the summations in (2.6) and (2.7), giving the half-space results (2.3) and (2.5).

For numerical evaluation, the sum in equation (2.6) must be approximated by truncating at a finite number of terms. In the case of a thick plate the number of terms needed for good convergence is relatively small, whereas a large number of terms is necessary in the case of a thin plate due to the slow convergence of the summation for thin plates. For example, 7 terms ($n = -3$ to $+3$) are required to give 0.1% calculation accuracy for a plate with thickness 3 times the probe length P_1P_2, Figure 2.1, whereas 25 terms ($n = -12$ to $+12$) are required to obtain the same calculation accuracy for a plate with thickness 1/5 of the probe length (8).

2.3.3 Finite Thickness Conductor with One Edge

When applying the method of images to obtain a solution for the measured potential drop when the probe is near an edge of a conductive plate, it is necessary to satisfy the Von Neumann boundary condition on the three surfaces of the conductor. Let the surfaces be at ($0 \le y \le \infty$, $z = 0$), ($0 \le y \le \infty$, $z = -c/2$) and ($-c/2 \le z \le 0$, $y = 0$), as shown in Figure 2.5. First, balance the source at P with an image source of the same polarity placed symmetrically on the y-axis. Then, by the argument of the previous section, there are two corresponding groups of images aligned in the z-direction with period c as introduced in Figure (2.5).

Thus the potential at a field point Q due to a current source and sink on the surface $z = 0$ can be written as a generalization of equation (2.6):

$$f(\rho) = \sum_{q=1}^{2}\sum_{n=-\infty}^{\infty}\left[\frac{1}{\sqrt{\rho_{2_q}^2 + (nc)^2}} - \frac{1}{\sqrt{\rho_{1_q}^2 + (nc)^2}}\right]. \tag{2.8}$$

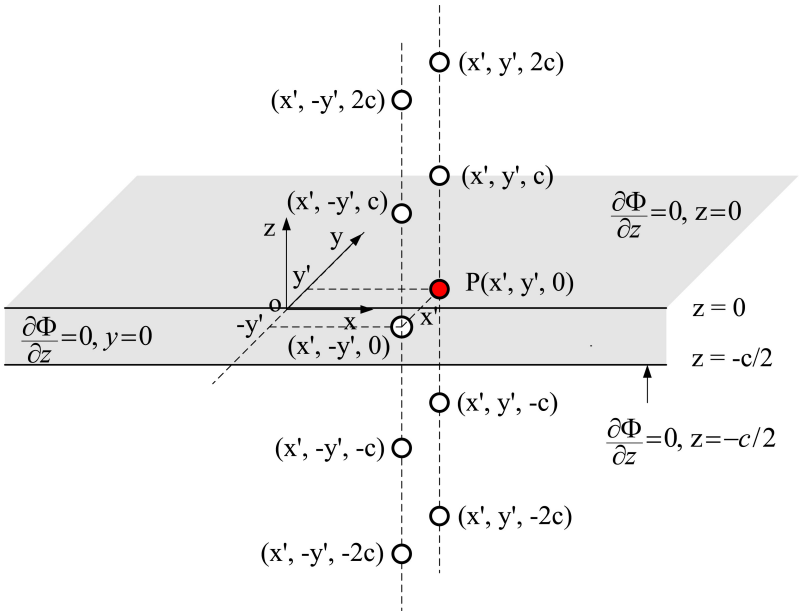

Figure 2.5 Current source at P and image sources (open circles) required to satisfy the interface conditions near the edge of a semi-infinite conductive plate.

Here, $\rho_{j_q} = \sqrt{\left(x - x'_j\right)^2 + \left[y - (-1)^q y'_j\right]^2}$ with $j, q = 1, 2$. Again, by using equation (2.4) the potential drop can be obtained. In the limiting case in which the source is moved well away from the edge; $0 \leq y \leq +\infty$, $y' \to +\infty$, agreement with the case of the large plate of finite thickness is obtained, equation (2.6). In the limiting case in which the source is moved to the edge; $0 \leq y \leq +\infty$, $y' \to +0$, equation (2.8) can be transformed to obtain

$$f(\rho) = 2 \sum_{n=-\infty}^{\infty} \left[\frac{1}{\sqrt{\rho_2^2 + (nc)^2}} - \frac{1}{\sqrt{\rho_1^2 + (nc)^2}} \right] \tag{2.9}$$

precisely two times equation (2.6) in which case the electrodes are centred on a large plate. This result has been verified experimentally as discussed in (9).

2.3.4 Fourier Series Solution

The infinite summations (2.6) and (2.8) do not converge very quickly for a plate that is thinner than the spacing of the probe points. Convergence can be improved by adopting a Fourier series representation for the infinite sum. The location of the current source and its images shown in Figures 2.4 and 2.5 exhibit periodicity in the direction perpendicular to the

plate surface, the z-direction, with period c. This means that the following identity (10) can be used:

$$\sum_{n=-\infty}^{+\infty} \frac{\exp\left[-\alpha\sqrt{\rho^2+(z-nc)^2}\right]}{\sqrt{\rho^2+(z-nc)^2}} = \frac{2}{c}K_0(\alpha\rho) + \frac{4}{c}\sum_{v=1}^{+\infty} K_0\left[\rho\sqrt{\alpha^2+\left(\frac{2\pi v}{c}\right)^2}\right]\cos(2\pi vz/c), \tag{2.10}$$

in which $\mathrm{Re}(\alpha) > 0$ and $K_0(x)$ is the modified Bessel function of the second kind of order zero. Putting $z = 0$ and $\alpha \to 0$ in (2.10), equation (2.6) can be transformed to obtain

$$f(\rho) = \frac{2}{c}\ln(\rho_1/\rho_2) + \frac{4}{c}\sum_{v=1}^{+\infty}\left\{K_0\left(\frac{2\pi v\rho_2}{c}\right) - K_0\left(\frac{2\pi v\rho_1}{c}\right)\right\}. \tag{2.11}$$

Relation (2.10) was also used in the theory of four-point alternating current potential drop on a metal plate (8). Results (2.6) and (2.11) provide alternative means of evaluating the potential drop measured between pick-up points of a four-point probe on the surface of a metal plate. The infinite sum in equation (2.8) can be transformed similarly, to give the following result for a plate with finite thickness and an edge,

$$f(\rho) = \sum_{q=1}^{2}\left\{\frac{2}{c}\ln(\rho_{1_q}/\rho_{2_q}) + \frac{4}{c}\sum_{v=1}^{+\infty}\left[K_0\left(\frac{2\pi v\rho_{2_q}}{c}\right) - K_0\left(\frac{2\pi v\rho_{1_q}}{c}\right)\right]\right\}. \tag{2.12}$$

Figure 2.6 compares the convergence of equation (2.11) with that of equation (2.6) for a case in which the probe length is 16 times the plate thickness ($L = \rho_1 + \rho_2 = 8c$). In general, equation (2.11) is much more efficient for computing the potential in the case of a plate with thickness smaller than the probe point separation.

2.3.5 Thin Plate Limiting Case

It is possible to show that only the first term on the right-hand side of equation (2.11) is significant when the plate thickness $c/2$ is significantly smaller than the separation between the probe points ρ_j. For large argument x, the following asymptotic expansion for $K_0(x)$ (11) holds:

$$K_0(x) \sim \sqrt{\frac{\pi}{2x}}e^{-x}\left(1 - \frac{1}{8x} + \ldots\right), \qquad x \gg 0. \tag{2.13}$$

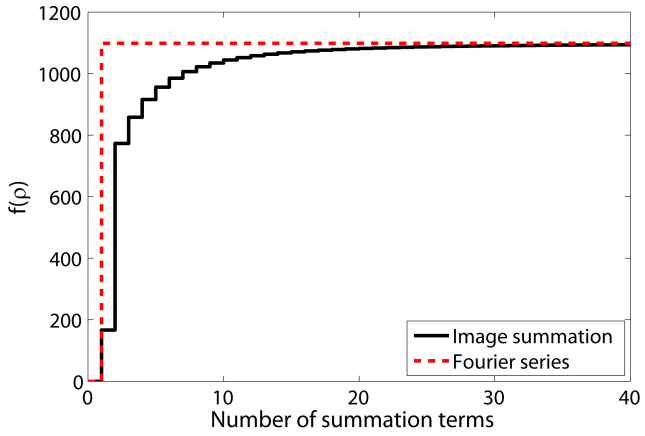

Figure 2.6 Image summation (2.6) converges slowly compared with Fourier series representation (2.11) in this case in which the probe length L is 16 times the plate thickness ($L = \rho_1 + \rho_2 = 6c + 2c = 8c$) and $c = 2$ mm. In (2.6) $n = 1, 2, ..., N$ and in (2.11) $v = 1, 2, ..., N$.

The exponential factor including the dimensionless parameter ρ/c is sufficient to make the summation significantly smaller than the first term in equation (2.11) when $\rho/c \gg 1$ and

$$f(\rho) \approx \frac{2}{c} \ln(\rho_1/\rho_2), \qquad \rho/c \gg 1. \tag{2.14}$$

This result agrees with that shown in reference (12), which followed the work of Uhlir (7).

2.3.6 Conductor with Finite Thickness and Width

By extension of the approach described in section 2.3.3, the method of images can be used to show that the potential in a conductive plate in the region $0 \le y \le b/2$ and $-c/2 \le z \le 0$ can be represented using a two-dimensional lattice of virtual sources, as shown in Figure 2.7. The potential of Q due to the source point P_2 and sink point P_1 on the surface is therefore given by inserting the following expression into equation (2.4);

$$f(\rho) = \sum_{q=1}^{2} \sum_{m=-\infty}^{\infty} \sum_{n=-\infty}^{\infty} \left[\frac{1}{\sqrt{\rho_{2_{mq}}^2 + (nc)^2}} - \frac{1}{\sqrt{\rho_{1_{mq}}^2 + (nc)^2}} \right], \tag{2.15}$$

in which $j, q = 1, 2$, $m = -\infty, .., -1, 0, 1, ..\infty$ and

$$\rho_{j_{mq}} = \sqrt{\left(x - x'_j\right)^2 + \left[y - (-1)^q y'_j - mb\right]^2}.$$

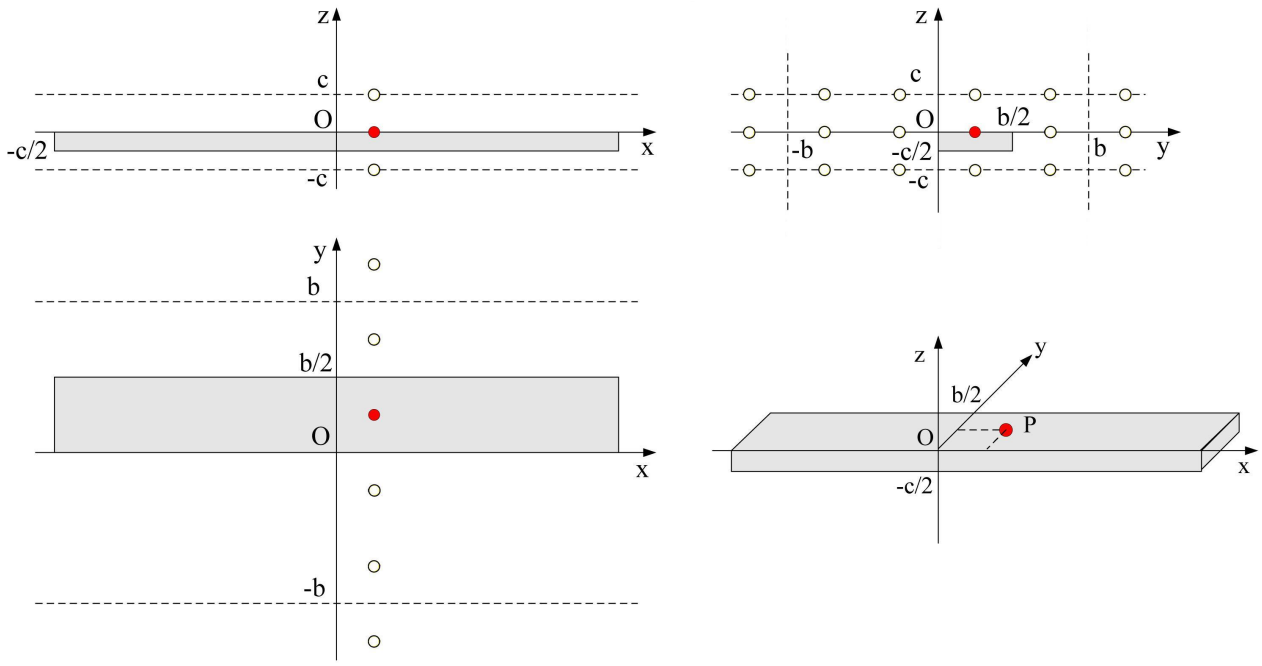

Figure 2.7 Current source at P and two-dimensional lattice of image sources (open circles) required to satisfy the interface conditions at the boundaries of a plate with finite thickness $c/2$ and width $b/2$.

In Fourier series form,

$$f(\rho) = \sum_{q=1}^{2}\sum_{m=-\infty}^{\infty}\left\{\frac{2}{c}\ln\left(\rho_{1_{mq}}/\rho_{2_{mq}}\right) + \frac{4}{c}\sum_{v=1}^{\infty}\left[K_0\left(2\pi v\rho_{2_{mq}}/c\right) - K_0\left(2\pi v\rho_{1_{mq}}/c\right)\right]\right\}. \tag{2.16}$$

2.3.7 Conductor with Finite Thickness, Width and Length

Similarly, applying the method of images shows that the potential generated by a source P_2 and sink P_1 on the surface ($z = 0$) of a finite conductive plate ($0 \le x \le a/2$, $0 \le y \le b/2$ and $-c/2 \le z \le 0$) may be represented in terms of a three-dimensional lattice of images, as shown in Figure 2.8:

$$f(\rho) = \sum_{p=1}^{2}\sum_{q=1}^{2}\sum_{l=-\infty}^{\infty}\sum_{m=-\infty}^{\infty}\sum_{n=-\infty}^{\infty}\left[\frac{1}{\sqrt{\rho_{2_{lmpq}}^2 + (nc)^2}} - \frac{1}{\sqrt{\rho_{1_{lmpq}}^2 + (nc)^2}}\right]. \tag{2.17}$$

Here, $j, p, q = 1, 2$, $l, m = -\infty, .., -1, 0, 1, ..\infty$ and

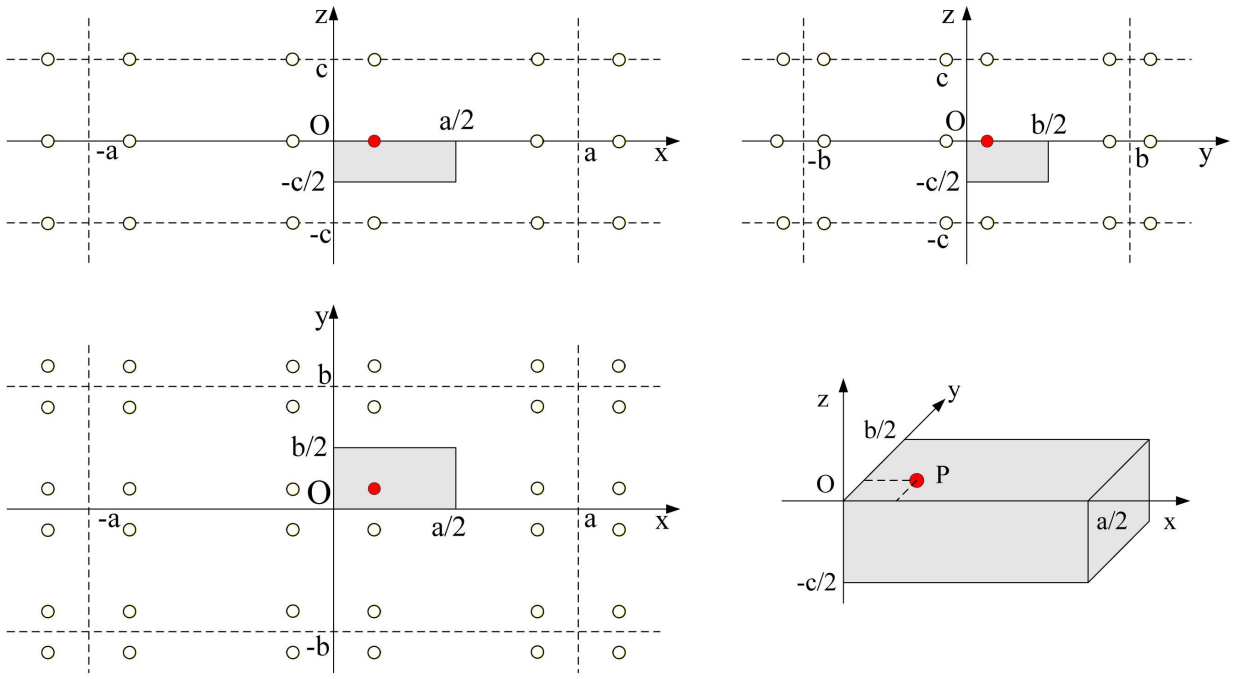

Figure 2.8 Current source at P and three-dimensional lattice of image sources (open circles) required to satisfy the interface conditions at the boundaries of a plate with finite thickness $c/2$, width $b/2$ and length $a/2$.

$$\rho_{j_{lmpq}} = \sqrt{\left(x - (-1)^p x'_j - la\right)^2 + \left[y - (-1)^q y'_j - mb\right]^2}.$$

Notice that the structure of the solution reflects the fact that in the $x-$ and $y-$directions two infinite sets of images are required, represented by the sums over p and q respectively, whereas in the $z-$direction only one infinite image set is required because the source lies at the surface defined by $z = 0$. In Fourier Series form,

$$\begin{aligned} f(\rho) \;=\; & \sum_{p=1}^{2}\sum_{q=1}^{2}\sum_{l=-\infty}^{\infty}\sum_{m=-\infty}^{\infty}\left\{\frac{2}{c}\ln\left(\rho_{1_{lmpq}}/\rho_{2_{lmpq}}\right) + \right. \\ & \left. + \frac{4}{c}\sum_{v=1}^{\infty}\left[K_0\left(2\pi v\rho_{2_{lmpq}}/c\right) - K_0\left(2\pi v\rho_{1_{lmpq}}/c\right)\right]\right\}. \end{aligned} \tag{2.18}$$

2.4 Experiment

In this section, the validation of computed voltage values, obtained using (2.18) in connection with (2.4), by comparison with experimental measurements on small metal plates is

described. A co-linear, symmetric, four-point-probe of the kind shown in Figure 2.1 was used. The probe was constructed by mounting four spring-loaded point contacts in a plastic support block. The separation of the contacts was measured using digital callipers and the dimensions of the probe are listed in Table 2.1. Potential drop measurements were made with the probe in contact with the largest face of six metal plates; three each of aluminium 2024-T3 and spring steel C1074/75. These were cut from the same aluminium and steel stock and their conductivity values measured independently by the DCPD technique applied to large sheets of the stock material, as described in (13). For each of the two metal types, the largest faces of the plates were nominally 6×2 cm^2, 6×4 cm^2 and 6×6 cm^2. The actual dimensions, given in Table 2.2, were measured by taking the average of several measurements of each dimension, made with digital callipers.

Table 2.1 Distance between the outer pair of (current-carrying) probe pins, L, (i.e. the probe length) and distance between the inner pair of voltage pick-up pins, P.

L (mm)	P (mm)
50.88 ± 0.02	20.30 ± 0.02

Table 2.2 Conductivity σ and dimensions, Figure 2.8, of metal plates used in the validation experiment, whose results are shown in Figures 2.9 and 2.10. Uncertainty in σ is ± 0.04 MS/m (13) and in dimensions is 0.01 mm.

Metal	Alloy	σ (MS/m)	$a/2$ (mm)	$b/2$ (mm)	$c/2$ (mm)
Aluminum	2024-T3	18.24	60.16	60.70	1.00
		18.24	60.06	40.29	1.00
		18.24	59.75	20.13	1.00
Spring Steel	C1074/75	5.50	60.61	60.22	1.57
		5.50	60.80	41.53	1.57
		5.50	61.05	20.36	1.57

In the experiment, both the current through the probe and the voltage drop between the pick-up points must be measured in order to validate the theory. The first can be can be monitored by measuring the voltage drop across a precision resistor in series with the drive circuit. The latter can be measured using a high input impedance circuit. Full experimental details are given in (14), where it is shown that ac and dc measurements and theory give

identical results when the frequency is below a certain threshold value that depends on the experimental parameters. In (14), an analytic expression is given for threshold frequency f_s below which the measured PD is real, constant and equal to the dc value for plates that are 'large' compared with the probe dimensions. A large plate is one whose PD measurements agree with theory developed for a plate with infinite lateral dimensions. In Table 2.3, the actual size of a plate needed to satisfy this condition is given to accuracy 1% and 5%. Here, in the case of the finite (small) plate, an analytic expression for f_s is not available, but in general all ACPD measurements show an f_s also exists. Here, low-frequency ac was used rather than direct current. For all of the small plates, which are the subject of this study, it was verified experimentally that the measured potential drop did not change over the frequency range 1 to 10 Hz, which implies that $f_s > 10$ Hz in these cases. In addition note that the skin depth in aluminium and spring steel at 10 Hz is ~37 mm and ~6 mm, respectively, and the relative factors of 37 and 4 times greater than the plate thicknesses which also indicates that the dc regime is applicable. In each measurement, the probe was centered on the plate and aligned with the x-axis, Figure 2.8. The theory of equation (2.18) is compared with experimental data taken on aluminium and steel in Figures 2.9 and 2.10, respectively. In the calculation, there are 10004 terms in total, $(2 \times 2 \times (2L+1) \times (2M+1) \times V$, $L = 30$, $M = 20$ and $V = 1)$ used in the summations and the calculated relative accuracy is 1×10^{-5}. From Figures 2.9 and 2.10 it can be observed that the measured potential drop is smaller in the case of aluminium than in the case of steel, due to the higher conductivity of aluminium compared with steel. It is also obvious that the measured potential drop increases as the plate width decreases, due to the fact that the lines of surface equipotential are forced closer together as the plate becomes smaller. Very good agreement between theory and experimental data shows that the effect of the plate edges is accurately represented by the theory.

The greatest contribution to the uncertainty in the potential drop measurements shown in Figures 2.9 and 2.10 comes from uncertainty in the probe pin positions relative to each other and the plate edges. This arises due to some lateral play in the pin position which can occur as the springs are compressed and because of the difficulty in exactly centering the probe on the test-piece. These effects are small, nonetheless, leading to over-all experimental uncertainty in

Table 2.3 Plate sizes necessary to obtain 5% and 1% agreement between DC potential drop voltages calculated for finite and infinite plates.

		5%	**1%**
plate shape	P/L	$a/(2L)$	
square	1/3	4.0	8.9
	5/7	3.7	8.2
	9/10	3.2	7.2
long, perpendicular	1/3	2.9	8.9
to probe	5/7	2.6	6.6
	9/10	2.4	5.3
		$b/(2L)$	
long, parallel to	1/3	3.4	9.3
probe	5/7	2.9	8.2
	9/10	2.4	7.0

the measured voltage of around 1%.

2.5 Accuracy of Large-plate Formulas Applied to Small Plates

The simplicity of standard formulas provided for potential drop measurements on large plates makes it attractive to employ these formulas generally (15). In this section, the accuracy with which large-plate formulas can be applied to small plates is elucidated in several cases. First define the percentage difference between the DC theory for large, thin plates, obtained using equation (2.14), and that for finite plates, obtained using equation (2.18),

$$\% \text{ difference} = \frac{V_{\text{finite}} - V_{\text{large}}}{V_{\text{large}}} \times 100. \tag{2.19}$$

In Figures 2.11, 2.12 and 2.13, the percentage difference in DC pick-up voltage, calculated using theory for finite and infinite plates, is shown as a function of plate size for various ratios of pick-up length to probe length, P/L. The ratio $P/L = 1/3$ gives a probe whose four points are equally spaced. This configuration is commonly adopted in practice. In Figure 2.11 the plates are square. In Figures 2.12 and 2.13 the plates are long in the dimension perpendicular and parallel to the line of the probe, respectively. In all cases it is seen that the influence of the plate edges becomes more important as the pick-up length decreases relative to the probe

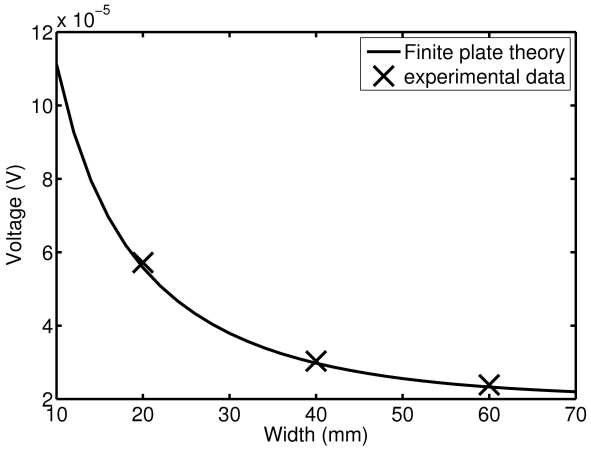

Figure 2.9 Theory, equation (2.18) with (2.4), compared with experimental data measured on aluminium plates with three different widths, Table 2.2. In the theory the plate length $a/2$ is fixed at 60 mm.

length. In other words, the accuracy of the infinite plate theory improves for a given plate size if the pick-up points are moved closer to the current injection points, rather than adopting an arrangement in which the four probe points are equally spaced. In Table 2.3, the plate sizes necessary to achieve 5% and 1% agreement between voltage values calculated using theory for finite and infinite plates are listed. For square plates, 5% agreement can be obtained with plates whose sides are only 3 or 4 times as large as the probe length. For 1% agreement, the plate sides must be approximately 8 times the probe length. For plates which are long in the dimension parallel to the probe (large a), the results are similar to those for square plates. For plates which are long in the dimension perpendicular to the probe (large b), side length a needs to be only 2 or 3 times L for 5% agreement, and between 5 and 9 times L for 1% agreement, depending on the pick-up length. These observations are in agreement with comments relating to plate thickness measurements made in (15) and serve as a useful guide in estimating the accuracy of four-point conductivity measurements interpreted with theoretical formulas developed for large plates.

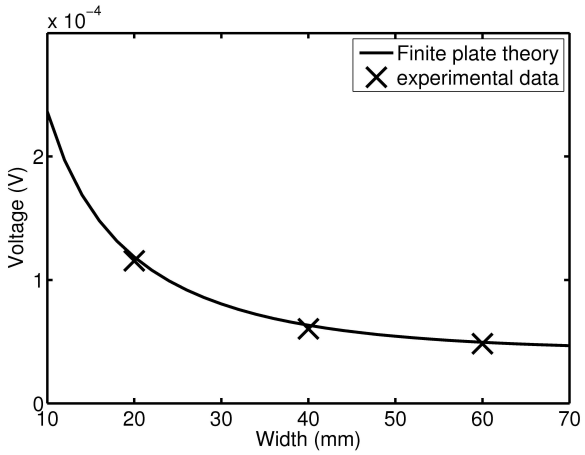

Figure 2.10 As for Figure 2.9 but for spring steel plates, Table 2.2

2.6 Conclusion

In this paper, an analytical solution has been presented to model edge effects in DCPD measurements on metal plates with finite thickness. A method-of-images solution converges quickly for plates somewhat thicker than the probe dimensions. A Fourier series summation, obtained using expressions originally developed to evaluate lattice sums in solid-state physics (10), converges more quickly for thinner plates and effectively reduces the triple infinite summation that results from the method-of-images, expression (2.17), to a double infinite summation, (2.18). The work of this paper focuses on DC potential drop measurements, from which the metal conductivity can be deduced. A similar theoretical approach can be applied to describe AC potential drop measurements as indicated in (8), from which the permeability of ferromagnetic metals can also be deduced (14).

2.7 Acknowledgement

This work was supported by the NSF Industry/University Cooperative Research program at Iowa State University's Center for Nondestructive Evaluation.

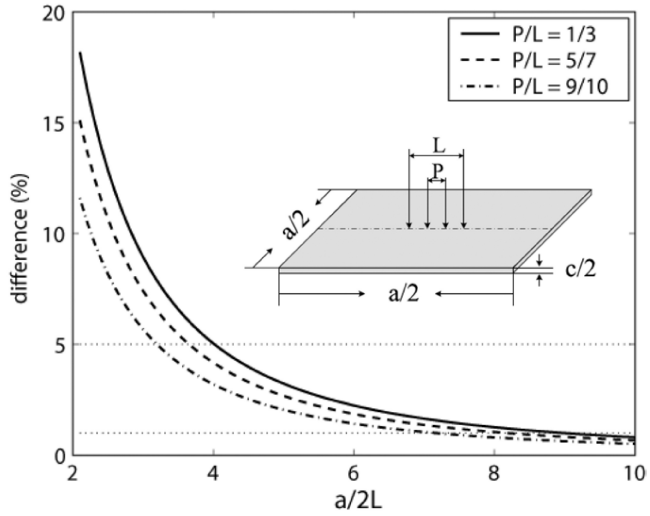

Figure 2.11 Percentage difference in DC pick-up voltage calculated using theory for finite and infinite thin plates, as a function of plate size. Plates are square with side length $a/2$. Probe length is L and pick-up length is P.

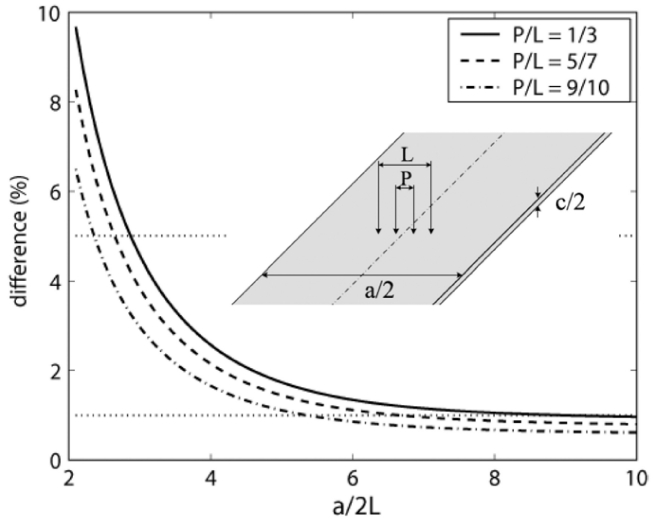

Figure 2.12 As for Figure 2.11 but for thin plates that are long perpendicular to the line of the probe (large b).

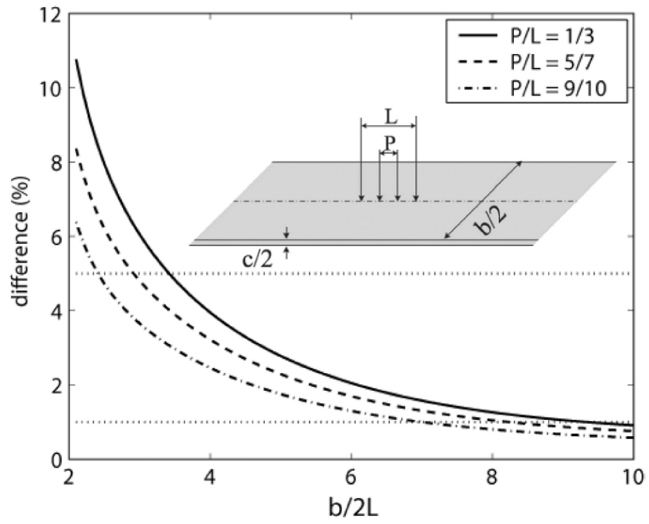

Figure 2.13 As for Figure 2.11 but for thin plates that are long parallel to the line of the probe (large a).

2.8 References

[1] Schroder D K 1998 *Semiconductor Material and Device Characterization* (New York: Wiley)

[2] Wang Y, Schimpf P H, Haynor D R and Kim Y 1998 Geometric effects on resistivity measurements with four-electrode probes in isotropic and anisotropic tissues *IEEE Trans. Biomed. Eng.* **45** 877–84

[3] Parasnis D S 1997 *Principles of Applied Geophysics* 5th edn (London: Chapman and Hall)

[4] Perloff D S 1977 Four-point sheet resistance correction factors for thin rectangular samples *Solid-State Electron.* **20** 681–7

[5] Yamashita M and Agu M 1984 Geometrical correction factor for semiconductor resistivity measurements by four-point probe method *Japan. J. Appl. Phys.* **23** 1499–504

[6] Valdes L B 1954 Resistivity measurements on germanium for transistors *Proc. IRE* **42** 420–7

[7] Uhlir A 1955 The potentials of infinite systems of sources and numerical solutions of problems in semiconductor engineering *Bell Syst. Tech. J.* **34** 105–28

[8] Bowler J R and Bowler N 2007 Theory of four-point alternating current potential drop measurements on conductive plates *Proc. R. Soc. A* **463** 817–36

[9] Lu Y, Bowler J R, Zhang C and Bowler N 2009 Edge effects in four point direct current potential drop measurement *Review of Progress in Quantitative Nondestructive Evaluation* **28** 271–8

[10] Sperb R 1998 An alternative to Ewald sums part I: identities for sums *Molecular Simulation* **20** 179-200

[11] Jeffery A and Dai H (ed) 2008 *Handbook of Mathematical Formulas and Integrals* 4th edn (London: Academic Press)

[12] Bowler N 2006 Theory of four-point direct-current potential drop measurements on a metal plate *Res. Nondestr. Eval.* **17** 29–48

[13] Bowler N and Huang Y 2005 Electrical conductivity measurement of metal plates using broadband eddy-current and four-point methods *Meas. Sci. Technol.* **16** 2193–200

[14] Bowler N and Huang Y 2005 Model-based characterization of homogeneous metal plates by four-point alternating current potential drop measurements *IEEE Trans. Magn.* **41** 2102–10

[15] Moore P O, McIntire P (ed) and Stanley R K (technical ed) 1995 *Nondestructive Testing Handbook* (*Special Nondestructive Testing Methods* vol 9) 2nd edn (Columbus: American Society of Nondestructive Testing)

CHAPTER 3. FOUR-POINT PROBE MEASUREMENTS OF DIRECT CURRENT POTENTIAL DROP ON LAYERED CONDUCTIVE CYLINDERS

A paper published in *The Journal of Measurement Science and Technology*

Yi Lu and John R. Bowler

3.1 Abstract

We have determined the steady state electric field due to direct current flowing via point contacts at the cylindrical surface of a uniformly layered conductive rod of finite length. The solution allows one to use four-point probe potential drop measurements to estimate the conductivity or thickness of the layer assuming the other parameters are known. The electrical potential in the rod has a zero radial derivative at its surface except at the injection and extractions points. This means that the required solution can be expressed in terms of a Green's function satisfying a Neumann boundary condition. Four point measurements have been made to demonstrate the validity of theoretical results.

3.2 Background and Problem Description

We have determined the electrical potential due to a steady current flowing between contact electrodes at the surface of a cylindrical rod of finite length having a uniform surface layer, a homogeneous conductive rod and tube being special cases (1; 2). The results can be used to interpret four point probe potential drop measurements. A typical industrial application is the measurement of the clad thickness on titanium clad copper rods used to carry large electric currents in harsh environments. In a common type of four point probe, current is passed

through a specimen via a pair of spring-loaded pins while the potential drop is measured between a second pair of pin electrodes. The electrodes are often co-linear or can be placed at the corners of a rectangle. In whatever arrangement is chosen, the effect of contact resistance is minimized by connecting the voltage pick-up pins to a relatively high impedance instrument for measuring the potential drop accurately.

In using four point probes for electrical conductivity measurement, a common approach is to work with an elementary formula to compute the conductivity and use a correction to account geometrical factors such as the edge effects of blocks (3; 4; 5) or disks (6; 7; 8), sheets (9) or the influence of the surface curvature on the potential at cylindrical surfaces (10; 11). Although most measurements use direct current, tests can also be performed by injecting alternating current at selected frequencies and the observations interpreted using theoretical predictions of the time harmonic potential. To get a basic solution for an alternating current potential drop (ACPD), closed-form analytical expressions have been derived for the electric field distribution in a conductive plate due to alternating current injected at the surface (12; 13; 14). In addition the four point probe potential drop has been found for transient current injection (15). An analytical expression for the alternating electric field inside a circular metal disk has also been derived, source and sink electrodes being located on opposite faces of the disk (16). Four-point measurements have also been widely used in the semiconductor industry to determine the electrical conductivity of semiconductor wafers (3), and to measure magnetoresistance (MA) as well as resistance area product (RA) of planar magnetic tunnel junction stacks (17). In addition, a new microscale Hall effect measurement method for fast characterization of semiconductor thin film using colinear four-point probes has been developed (18). Recently, microscopic measurements have become possible with the advent of micron scale probes for the study of local material property variations (19; 20; 21). Other applications of four point measurement are aimed at monitoring changes in the condition of metals due to heat treatment (22; 23; 24) or to estimating the dimensions of cracks (25; 26).

For cases where direct current is injected, the electric potential in a piecewise uniform electrical conductor satisfies the Laplace equation and has zero normal gradient at every point on the interior of its outer surface, S_0, except where current is injected or extracted. Here we

consider current contacts on the curved surface of a circular cylinder. By approximating the electrode contact regions as points on the surface, the solution can be represented conveniently in terms of a suitable Green's kernel, $G(\mathbf{r}|\mathbf{r}')$, that satisfies a Neumann boundary condition at the outer surface. This means that $\partial G/\partial n = 0$ on S_0 where n is a local coordinate in the direction of an outward normal.

The seminal work on the development of Green's kernels in cylindrical and spherical coordinates is that of Dougall (27) whose contribution on Dirichlet kernels was highlighted in the text on Bessel functions by Gray, Mathews and MacRobert (28). Much later, the static Neumann kernel for a finite cylinder was determined by Murashima (29) and used by Yamashita, Nishii and Kurihara (1) for computing resistivity correction factors for the four point probe method. Recently, the approach has been extended to provide a four point probe theory for measurements on tubes (2).

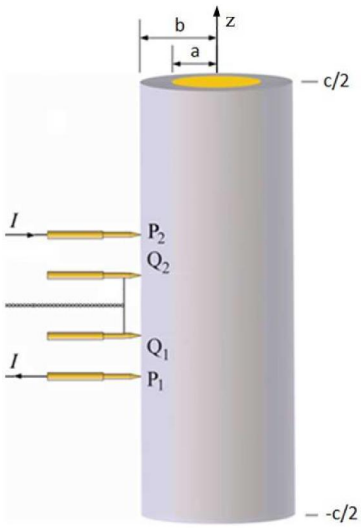

Figure 3.1 Four-point probe on a cylindrical rod with a uniform layer.

In Murashima's analysis, the solution is expressed in terms of Bessel functions of the first kind in which the Neumann boundary condition on the cylindrical surface, radius b, is satisfied using values of the separation parameter κ that are the roots of $J'_m(\kappa b) = 0$ for $m = 0, 1, 2 \ldots$ (1), where $J'_m(\kappa b) = \left.\dfrac{dJ_m(\kappa\rho)}{d\rho}\right|_{\rho=b}$. An alternative is to write the solution in terms of associated Bessel functions (30). Here we consider a layered rod by generalizing the

Murashima kernel to the case in which we have a homogeneous circularly cylindrical core of arbitrary conductivity surrounded by a uniform homogeneous layer as, shown in Figure 3.1.

3.3 Potential in a Layered Cylinder

A brief statement of the mathematical problem that we consider is as follows. The potential $V(\rho, \phi, z)$ in a conductive circular cylinder of outer radius b, length c, having a concentric core radius a satisfies the Laplace equation,

$$\nabla^2 V = 0. \tag{3.1}$$

At the interface between the core and the layer, the potential is continuous,

$$V(a_-, \phi, z) = V(a_+, \phi, z), \tag{3.2}$$

as is the normal component of the current density,

$$\sigma_1 \left.\frac{\partial V}{\partial \rho}\right|_{\rho=a_-} = \sigma_2 \left.\frac{\partial V}{\partial \rho}\right|_{\rho=a_+}, \tag{3.3}$$

where σ_1 is the conductivity of the core and σ_2 that of the outer layer and $\pm$ subscripts, refer to the limit of approach to the value a from a greater or lesser value, respectively. At the ends of the cylinder, the normal component of the current density is zero, hence,

$$\left.\frac{\partial V}{\partial z}\right|_{z=\pm\frac{c}{2}} = 0. \tag{3.4}$$

The radial current density over most of the outer surface is zero except for the points of current injection, $\mathbf{r}'_1 = \{b_-, \phi_1, z_1\}$ and extraction, $\mathbf{r}'_2 = \{b_-, \phi_2, z_2\}$, denoted by P_1 and P_2 respectively in Figure 3.1. Hence the normal gradient of the potential at the outer cylindrical surface can be expressed

$$\left.\frac{\partial V}{\partial \rho}\right|_{\rho=b_-} = \frac{I}{b\sigma_2}[\delta(z - z_1)\delta(\phi - \phi_1) - \delta(z - z_2)\delta(\phi - \phi_2)]. \tag{3.5}$$

One can also consider current injection at the end of the cylinder but this case will not be examined further.

The steady state potential is conveniently expressed in terms of a Neumann kernel, $G(\rho, \phi, z|\rho', \phi', z')$, which is a solution of

$$\nabla^2 G = -\delta(\rho - \rho')\frac{1}{\rho}\delta(\phi - \phi')\delta(z - z'), \tag{3.6}$$

satisfying the continuity conditions

$$G(a_-, \phi, z|\rho', \phi', z') = G(a_+, \phi, z|\rho', \phi', z'), \tag{3.7}$$

and

$$\sigma_1 \left.\frac{\partial G}{\partial \rho}\right|_{\rho=a_-} = \sigma_2 \left.\frac{\partial G}{\partial \rho}\right|_{\rho=a_+}, \tag{3.8}$$

at the interface between the core and the layer. At the ends of the cylinder

$$\left|\frac{\partial G}{\partial z}\right|_{z=\pm\frac{c}{2}} = \beta, \tag{3.9}$$

where β is a constant which need not to be zero because it vanishes in a solution for two injection points of opposite sign. At the outer cylindrical surface, the Neumann boundary condition

$$\left.\frac{\partial G}{\partial \rho}\right|_{\rho=b_-} = 0, \tag{3.10}$$

is imposed.

By applying Green's second theorem to the region bounded by the surface S_2 enclosing the layer we get

$$V(\mathbf{r}) = \int_{S_2} G(\mathbf{r}|\mathbf{r}')\frac{\partial V(\mathbf{r}')}{\partial n'} - V(\mathbf{r}')\frac{\partial G(\mathbf{r}|\mathbf{r}')}{\partial n'}\, dS'. \tag{3.11}$$

A similar integral expression gives the potential in the core region. Using the boundary and interface conditions, one can show that the potential at any point in the conductor is given by

$$V(\mathbf{r}) = \frac{I}{b\sigma_2}[G(\mathbf{r}|\mathbf{r}'_1) - G(\mathbf{r}|\mathbf{r}'_2)], \tag{3.12}$$

since equation (3.5) provides the only locations at which the normal gradient at the bounding surface of the conductive cylinder is non-vanishing. Hence the potential difference between two voltage electrode contact points on the surface of the cylinder, denoted by Q_1 and Q_2 in Figure 3.1, is

$$\Delta V = \frac{I}{b\sigma_2}[G(\mathbf{r}_1|\mathbf{r}'_1) - G(\mathbf{r}_2|\mathbf{r}'_1) - G(\mathbf{r}_1|\mathbf{r}'_2) + G(\mathbf{r}_2|\mathbf{r}'_2)]. \tag{3.13}$$

The problem of predicting the potential thus reduces to one of finding the Neumann kernel, $G(\mathbf{r}|\mathbf{r}')$.

3.4 Derivation of the Neumann Kernel

3.4.1 Elementary Solutions

Initially, we consider the case where the electrical conductivity $s(\rho)$, normalized by dividing by a reference conductivity, is an arbitrary function of of the radial coordinate. Later we revert to a piecewise constant conductivity. The electrostatic potential is, in general, a solution of

$$\nabla \cdot \Big[s(\rho) \nabla V(\rho, \phi, z) \Big] = 0. \tag{3.14}$$

Separation of variables in this equation gives the elementary solutions from which one can draw some general conclusions about the orthogonality of the radially dependent eigenfunctions. We proceed by defining the elementary product solution

$$V(\rho, \phi, z) = R(\rho)\, \Phi(\phi)\, Z(z), \tag{3.15}$$

substituting into (3.14) and dividing the resulting equation by $s(\rho)V(\rho, \phi, z)$ to give

$$\frac{1}{R\rho\, s} \frac{\partial}{\partial \rho} \left[s\rho \frac{\partial R}{\partial \rho} \right] + \frac{1}{\Phi \rho^2} \frac{\partial^2 \Phi}{\partial \phi^2} + \frac{1}{Z} \frac{\partial^2 Z}{\partial z^2} = 0. \tag{3.16}$$

This can be decomposed by equating the ϕ and z dependent terms to suitable separation parameters $-m^2$ and κ^2 respectively. The azimuthal dependence is thereby shown to be a solution of

$$\frac{d^2 \Phi}{d\phi^2} + m^2 \Phi = 0, \tag{3.17}$$

where the function $\Phi(\phi)$ is periodic with a period 2π. We choose an even elementary solution $\cos(m\phi)$, in which $m = 0, 1, 2, \ldots$. The function of the axial variable is a solution of

$$\frac{d^2 Z}{dz^2} - \kappa^2 Z = 0. \tag{3.18}$$

and the function of the radial variable satisfies

$$\left(\frac{d}{d\rho} s\rho \frac{d}{d\rho} - m^2 \frac{s}{\rho} + \kappa^2 \rho s \right) R = 0. \tag{3.19}$$

This equation is of the Sturm-Liouville type and as such its solutions can be expressed in terms of a set of continuous eigenfunctions provided the function $s(\rho)$ is piecewise continuous (31).

Furthermore these eigenfunctions are orthogonal, although, in fact, there are only a few cases for which they may be determined analytically, the case where $s(\rho)$ is piecewise constant being one of them.

We consider a uniform layer over a uniform circular core and normalize the conductivity variation by dividing by the conductivity of the region into which current is injected. Writing $s_1 = \sigma_1/\sigma_2$, the normalized conductivity is thereby defined by

$$s(\rho) = \begin{cases} s_1 & 0 \le \rho < a \\ 1 & a < \rho \le b. \end{cases} \tag{3.20}$$

and equation (3.19) can be expressed for a piecewise constant region as

$$\left[\rho^2 \frac{d^2}{d\rho^2} + \rho \frac{d}{d\rho} + \left(\kappa^2\rho^2 - m^2\right)\right] R = 0. \tag{3.21}$$

This equation is satisfied by a linear combination of Bessel functions of the first and second kinds, $J_m(\kappa\rho)$ and $Y_m(\kappa\rho)$.

The core region solution does not include a term containing $Y_m(\kappa\rho)$ since it is singular at $\rho = 0$. Therefore the required solution of equation (3.21) for a piecewise constant conductivity has the form

$$R(\rho) = \begin{cases} J_m(\kappa\rho) & 0 \le \rho < a \\ \\ P(\kappa)J_m(\kappa\rho) + Q(\kappa)Y_m(\kappa\rho) & a < \rho \le b. \end{cases} \tag{3.22}$$

The coefficients $P(\kappa)$ and $Q(\kappa)$ are determined using the continuity conditions that apply at $\rho = a$, equations (3.2) and (3.3), from which we find

$$P(\kappa) = \frac{\pi\kappa a}{2\sigma_2}\left[\sigma_2 J_m(\kappa a) Y_m'(\kappa a) - \sigma_1 J_m'(\kappa a) Y_m(\kappa a)\right] \tag{3.23}$$

and

$$Q(\kappa) = \frac{\pi\kappa a}{2\sigma_2}(\sigma_1 - \sigma_2) J_m(\kappa a) J_m'(\kappa a). \tag{3.24}$$

In the case where $\sigma_1 = \sigma_2$, then $Q = 0$ and the bracketed term in equation (3.23) becomes a Wronskian relation (32),

$$J_{m+1}(z) Y_m(z) - J_m(z) Y_{m+1}(z) = \frac{2}{\pi z}, \tag{3.25}$$

which can be evaluated to show that $P = 1$. Thus as the conductivity tends towards uniformity, the core and layer solutions in equation (3.22) merge into one, as they should. In general, however, discrete eigenvalues κ_{mn} are determined from the roots of

$$P(\kappa)J'_m(\kappa b) + Q(\kappa)Y'_m(\kappa b) = 0, \tag{3.26}$$

to ensure that the Neumann condition, equation (3.10), is satisfied at the outer cylindrical surface. This yields an infinite series of roots, κ_{mn} indexed by $n = 1, 2, 3\ldots$ at each order m and a corresponding set of eigenfunctions

$$R_{mn}(\rho) = \begin{cases} J_m(\kappa_{mn}\rho) & 0 \le \rho < a \\ \\ P(\kappa_{mn})J_m(\kappa_{mn}\rho) + Q(\kappa_{mn})Y_m(\kappa_{mn}\rho) & a < \rho \le b. \end{cases} \tag{3.27}$$

In one notable case, the first root at zero order, we have $\kappa_{01} = 0$. The zero root occurs because $\lim_{\kappa_{01}\to 0} P(\kappa_{01})J'_0(\kappa_{01}\rho) + Q(\kappa_{01})Y'_0(\kappa_{01}\rho) \to 0$. Then, for the core and layer regions, we find respectively that $\lim_{\kappa_{01}\to 0} J_0(\kappa_{01}\rho) \to 1$, $\lim_{\kappa_{01}\to 0} P(\kappa_{01})J_0(\kappa_{01}\rho) + Q(\kappa_{01})Y_0(\kappa_{01}\rho) \to 1$, and $R_{01}(\rho) = 1$ for $0 \le \rho \le b$.

3.4.2 Orthonormal Set for the Radial Dependence

The fact that equation (3.19) is of the Sturm-Liouville type with a Hermitian operator means that continuous solutions exist for a piecewise continuous conductivity that may possess any number of discontinuities (33). All permissible solutions can be expanded in terms of an orthonormal set of continuous eigenfunctions, written as $f_{mn}(\rho) = c_{mn}R_{mn}(\rho)$, the normalization coefficients, c_{mn}, being derived as follows.

We use a set of integrals that are valid for any two cylinder Bessel functions, ($\mathscr{C}_m$ and $\bar{\mathscr{C}}_m$ which denote J_m or Y_m) (34):

$$\begin{aligned} &\int^z \mathscr{C}_m(kz)\,\bar{\mathscr{C}}_m(lz)\,z\,dz \\ &= \begin{cases} \dfrac{z}{k^2 - l^2}\left[k\bar{\mathscr{C}}_m(lz)\,\mathscr{C}_{m+1}(kz) - l\mathscr{C}_m(kz)\,\bar{\mathscr{C}}_{m+1}(lz)\right] & k \ne l \\ \\ \dfrac{z^2}{4}\left[2\mathscr{C}_m(kz)\,\bar{\mathscr{C}}_m(kz) - \mathscr{C}_{m-1}(kz)\,\bar{\mathscr{C}}_{m+1}(kz) - \mathscr{C}_{m+1}(kz)\,\bar{\mathscr{C}}_{m-1}(kz)\right] & k = l. \end{cases} \end{aligned} \tag{3.28}$$

Based on the above integral properties, and the need to include a weight function $w(\rho) = \rho s(\rho)$ in the orthogonality relationship according to the Sturm-Liouville analysis (31), we can derive the normalization coefficients c_{mn} for the orthonormal eigenfunctions in equation (3.34) from

$$\begin{aligned}
&\int_0^b R_{mn}(\rho)\, R_{ml}(\rho)\, s(\rho)\, \rho d\rho = s_1 \int_0^a J_m(\kappa_{mn}\rho) J_m(\kappa_{m\ell}\rho)\, \rho d\rho \\
&+\int_a^b \left[P(\kappa_{mn})J_m(\kappa_{mn}\rho)+Q(\kappa_{mn})Y_m(\kappa_{mn}\rho)\right]\left[P(\kappa_{m\ell})J_m(\kappa_{m\ell}\rho)+Q(\kappa_{m\ell})Y_m(\kappa_{m\ell}\rho)\right]\rho d\rho \\
&= \begin{cases} 0 & n \neq \ell \\ \dfrac{(s_1-1)\,A_{mn}+B_{mn}}{2\kappa_{mn}^2} & n = \ell. \end{cases}
\end{aligned} \tag{3.29}$$

Here,

$$A_{mn} = \left(\kappa_{mn}^2 a^2 - m^2\right) J_m^2(\kappa_{mn}a) - s_1 \kappa_{mn}^2 a^2 \left[J_m'(\kappa_{mn}a)\right]^2 \tag{3.30}$$

and

$$B_{mn} = \left(\kappa_{mn}^2 b^2 - m^2\right) \left[P(\kappa_{mn})J_m(\kappa_{mn}b) + Q(\kappa_{mn})Y_m(\kappa_{mn}b)\right]^2. \tag{3.31}$$

Hence

$$c_{mn} = \frac{\sqrt{2}\kappa_{mn}}{\sqrt{(s_1-1)\,A_{mn}+B_{mn}}}. \tag{3.32}$$

We can now write an arbitrary solution $F_m(\rho)$ of (3.19) as

$$F_m(\rho) = \sum_{n=0}^{\infty} C_{mn} f_{mn}(\rho). \tag{3.33}$$

and determine the coefficients C_{mn} by applying

$$\int_0^b f_{mn}(\rho) f_{m\ell}(\rho) s(\rho) \rho\, d\rho = \delta_{n\ell} \tag{3.34}$$

defined with respect to a weight function $s(\rho)\rho$, identified according the the general theory (31) from the third term in (3.19) , where $s(\rho)$ is given by (3.20) in the present case and $\delta_{n\ell}$ is a Kronecker delta; unity if $\ell = n$ and zero otherwise.

3.4.3 Green's Function

The orthogonality property allows one to expand the radial delta function to give a completeness relationship

$$\frac{\delta(\rho-\rho')}{\rho'} = \sum_{n=1}^{\infty} f_{mn}(\rho) f_{mn}(\rho'). \tag{3.35}$$

For the azimuthal dependence, we use another completeness relationship

$$\delta\left(\phi-\phi'\right)=\frac{1}{2\pi}\sum_{m=0}^{\infty}\varepsilon_m\cos[m(\phi-\phi')] \tag{3.36}$$

in which $\varepsilon_m=1$ for $m=0$ and $\varepsilon_m=2$ otherwise. By expressing the Green's function as

$$G\left(\rho,\phi,z|\rho',\phi',z'\right)=\frac{1}{2\pi}\sum_{m=0}^{\infty}\varepsilon_m\cos\left[m(\phi-\phi')\right]\sum_{n=1}^{\infty}f_{mn}\left(\rho\right)f_{mn}\left(\rho'\right)g_{mn}(z|z'), \tag{3.37}$$

and substituting (3.35) -(3.37) into (3.6), we find that the z dependence is a solution of

$$\frac{d^2g_{mn}\left(z|z'\right)}{dz^2}-\kappa_{mn}^2g_{mn}\left(z|z'\right)=-\delta\left(z-z'\right), \tag{3.38}$$

satisfying equation (3.9) with $\beta=0$. The required function has the form $E_{\pm}\cosh\left[\kappa_{mn}\left(\frac{c}{2}\mp z\right)\right]$ where the $E_{\pm}$ are constants and the $\mp$ sign depends on whether $z>z'$ or $z<z'$ respectively. The coefficients are found using a standard procedure for a Green function in one dimension. By integrating equation (3.38) between $z'-\varepsilon$ and $z'+\varepsilon$ and taking the limit as $\varepsilon\to 0$ we can get

$$\left.\frac{dg_{mn}\left(z|z'\right)}{dz}\right|_{z'_+}-\left.\frac{dg_{mn}\left(z|z'\right)}{dz}\right|_{z'_-}=-1, \tag{3.39}$$

integrating a second time and taking the limit gives

$$g_{mn}\left(z|z'\right)\big|_{z'_+}-g_{mn}\left(z|z'\right)\big|_{z'_-}=0. \tag{3.40}$$

Characteristically, the one dimensional Green function has a jump in the first derivative of -1 and its value is continuous. By using equations (3.39) and (3.40) we find that

$$g_{mn}\left(z|z'\right)=\frac{\cosh\left[\kappa_{mn}\left(\frac{c}{2}-z_>\right)\right]\cosh\left[\kappa_{mn}\left(\frac{c}{2}+z_<\right)\right]}{\kappa_{mn}\sinh\left(\kappa_{mn}c\right)}, \tag{3.41}$$

where $z_>$ is the greater and $z_<$ the lesser of z and z'. For the case where $\kappa_{01}=0$, the solution, $g_{01}\left(z|z'\right)=-\left|z-z'\right|/2$ satisfies the Neumann boundary condition at the ends of the cylinder, equation (3.9), with β non-zero but with two singular sources of opposite polarity, as with the four-point probe, the normal gradient at the surfaces $z=\pm\frac{c}{2}$ are zero.

Based on the above analysis, it is a relatively simple step to define the Neumann Green's function for a point source in a layered cylinder. This has the form

$$\begin{aligned}G\left(\rho,\phi,z|\rho',\phi',z'\right) &= \frac{-|z-z'|\,f_{01}\left(\rho\right)f_{01}\left(\rho'\right)}{4\pi}+\frac{1}{2\pi}\sum_{n=2}^{\infty}f_{0n}\left(\rho\right)f_{0n}\left(\rho'\right)g_{0n}\left(z|z'\right)\\ &+\frac{1}{\pi}\sum_{m=1}^{\infty}\cos\left[m(\phi-\phi')\right]\sum_{n=1}^{\infty}f_{mn}\left(\rho\right)f_{mn}\left(\rho'\right)g_{mn}\left(z|z'\right).\end{aligned} \tag{3.42}$$

This formula is exact for an arbitrary source and field point. Hence equation (3.13) is applicable for arbitrary electrode placement.

3.5 Two Special Cases

In many applications, the probe is located on the outer surface of the layered cylinder which means the source point is at the outer surface of the layer, as shown in Figure 3.1. Two special cases arise as follows.

3.5.1 Homogeneous Cylinder

When $a = 0$ or $\sigma_1 = \sigma_2$, the two-layered cylinder becomes a homogeneous one and $s_1 = \sigma_1/\sigma_2 = 1$. In which case equation (3.23) simplifies using the Wronskian (4.17) to give $P = 1$, $Q = 0$ from (3.24). Then $R_{mn}(\rho) = J_m(\kappa_{mn}\rho)$ and the $f_{mn}(x)$ functions in the Neumann Green's Function simplify to give:

$$f_{mn}(x) = \begin{cases} \dfrac{\sqrt{2}}{b} & m = 0,\ n = 1 \\ \dfrac{\sqrt{2}}{bJ_0(\kappa_{0n}b)} J_0(\kappa_{0n}x) & m = 0,\ n > 1 \\ \dfrac{\sqrt{2}\kappa_{mn}}{\sqrt{(\kappa_{mn}^2 b^2 - m^2)} J_m(\kappa_{mn}b)} J_m(\kappa_{mn}x) & m > 0,\ n \geq 1. \end{cases} \tag{3.43}$$

3.5.2 Hollow Cylinder

Similarly when $\sigma_1 = 0$, a layered cylinder becomes a hollow one, $R_{mn}(\rho) = P(\kappa_{mn})J_m(\kappa_{mn}\rho)$ $+Q(\kappa_{mn})Y_m(\kappa_{mn}\rho)$ and $s_1 = \sigma_1/\sigma_2 = 0$. In which case equation (3.23) simplifies to give

$$P(\kappa_{mn}) = \frac{\pi\kappa_{mn}a}{2} J_m(\kappa_{mn}a)\, Y'_m(\kappa_{mn}a), \tag{3.44}$$

and (3.24) reduces to

$$Q(\kappa_{mn}) = -\frac{\pi\kappa_{mn}a}{2} J_m(\kappa_{mn}a)\, J'_m(\kappa_{mn}a). \tag{3.45}$$

In the Neumann Green's Function, the $f_{mn}(x)$ become

$$f_{mn}(x)=\begin{cases}\dfrac{\sqrt{2}}{\sqrt{b^2-a^2}} & m=0,\ n=1\\ \dfrac{\sqrt{2}}{\sqrt{b^2R_{0n}^2(b)-a^2J_0^2(\kappa_{0n}a)}}R_{0n}(x) & m=0,\ n>1\\ \dfrac{\sqrt{2}\kappa_{mn}}{\sqrt{(\kappa_{mn}^2b^2-m^2)R_{mn}^2(b)-(\kappa_{mn}^2a^2-m^2)J_m^2(\kappa_{mn}a)}}R_{mn}(x) & m>0,\ n\geq 1.\end{cases} \tag{3.46}$$

3.6 Experiments and Discussion

The above theory is applicable for arbitrary relative placement of the four probe points on the convex surface of the cylinder. Two different four-point probes are in general use, one with rectangular arrangement of contact points and one in which the contact points are co-linear. In this section, we consider a collinear probe, with pins aligned parallel to the axis of the cylinder. In the experiments, both the current through the probe and the voltage drop between the pick-up points are measured in order to validate the theory. The first is monitored by measuring the potential drop across a precision resistor in series with the drive circuit. Voltage is measured using a SR830 DSP lock-in amplifier. More experimental details are given in (35; 36).

The theoretical expression for the potential drop at a layered conductive cylinder has been validated experimentally. Two four-point probes with co-linear pins are used. The four pins are mounted in a plastic support block and the separations of the contacts are measured using a traveling microscope. The dimensions of the probes are listed in Table 3.1 as shown in Figure 3.2.

In the experiments, first, a copper rod and a titanium alloy rod are measured to confirm the predictions for homogeneous rods. We also made measurements on an inconel 600 tube and a titanium clad copper rod for the layered case. The latter is manufactured to act as a bus bar for carrying high current in a hostile environment.

The copper rod has the same conductivity as the copper core in the titanium clad copper rod. The dimensions of the titanium alloy rod are measured using a traveling microscope and

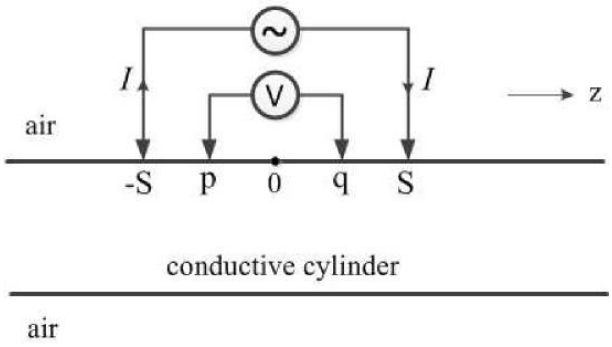

Figure 3.2 Schematic showing the arrangement of a four-point probe.

Table 3.1 Probe parameters in the experiments. Uncertainty 0.02 mm.

Probe	**S (mm)**	**p (mm)**	**q (mm)**
I	9.00	-3.06	3.00
II	20.14	-17.76	17.34

others are measured with a digital calliper. The conductivities of the copper rod and the titanium alloy rod are measured independently using a two-point DCPD method (37) which gives a more accurate result. The conductivities of the inconel 600 tube and the outer layer of the titanium clad copper rod are provided by the test-piece vendor. The test-piece parameters are shown in Table 3.2.

3.6.1 Homogeneous Cylinder

In this experiment, the copper rod is measured using four-point Probe I, which is put at the center of the rod, and the measured and calculated DC pick-up voltages are listed in Table 3.3. The latter is calculated using equations (3.13), (3.42) and (3.43), which is in good agreement with the experiment. Figure 3.3 shows the calculated potential drop decrease as the radius of

Table 3.2 Test-piece parameters in the experiments.

Metal	**2a (mm)**	$\boldsymbol{\sigma_1}$ **(MS/m)**	**2b (mm)**	$\boldsymbol{\sigma_2}$ **(MS/m)**	**c (mm)**
Copper Rod	N/A	N/A	15.96±0.01	57.23	200
Ti-6Al-4V	N/A	N/A	12.63±0.01	0.594	307
Inconel 600 Tube	15.75±0.01	N/A	19.05±0.01	0.986	200
Ti clad Cu Rod	15.54±0.02	57.23	19.78±0.02	1.798	200

Table 3.3 Calculated and measured DC pick-up voltages on test-pieces.

Test-piece	**Calculated (V)**	**Measured (V)**	**Error (%)**
Copper Rod	8.723×10^{-7}	8.834×10^{-7}	1.26
Inconel 600 Tube	1.488×10^{-4}	1.527×10^{-4}	2.55
Ti clad Cu Rod	2.883×10^{-5}	2.927×10^{-5}	1.50

the copper rod increases.

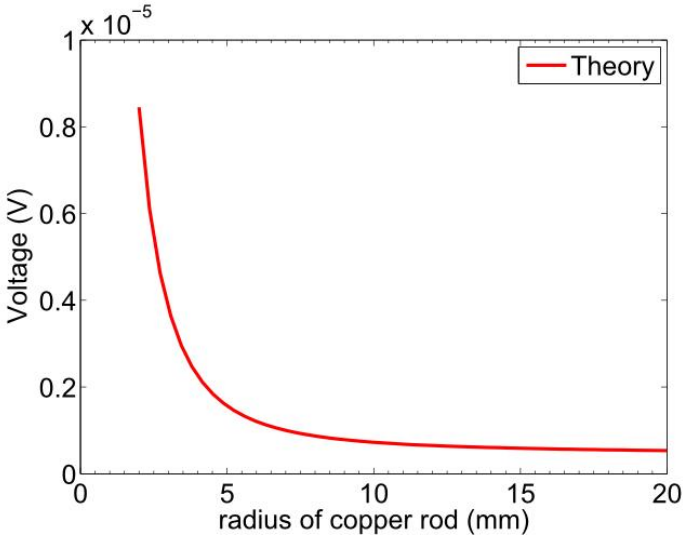

Figure 3.3 Calculated DC pick-up voltage (V) by a collinear four-point Probe I on a homogeneous copper rod, as a function of the radius of the rod.

A titanium alloy rod has been measured with the Probe II with the probe at various positions on the cylinder relative to the end of the rod. The experimental data are compared with the theory curve in Figure 3.4. In the figure, an obvious edge effect can be observed and the good agreement shows that the edge effect can be accurately predicted by the theory.

3.6.2 Hollow Cylinder

A homogeneous inconel 600 tube is measured with the Probe I to verify the tube predictions. In the experiment, the probe is placed at the center of tube with the line of the probe parallel to the tube axis and the potential drop between the two inner pins is measured to be compared with the theory. The tube's dimensions and conductivity are given in Table 3.2. The potential drop is calculated by equations (3.13), (3.42) and (3.46), which shows an agreement with the

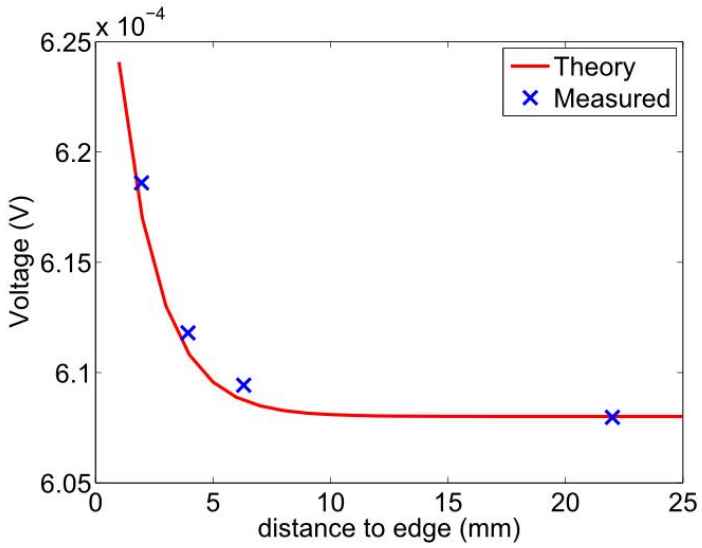

Figure 3.4 DC potential drop (V) measured using collinear four-point Probe II on a homogeneous titanium alloy rod (crosses), compared with the theory (solid line), as a function of the probe position.

measurement as shown in Table 3.3. If the measurement position, the outer radius and length of the specimen are kept fixed, the voltage increases significantly as the tube wall thickness decreases, particularly below about 1mm, as shown in Figure 3.5. This means this method is very sensitive and can be used to monitor the wall thicknesses of thin tubes.

3.6.3 Layered Cylinder

In this experiment, a titanium clad copper rod is measured by placing the Probe II at the center, parallel to the axis of the rod. The dimension and conductivity parameters are listed in Table 3.2. The measured and calculated potential drops are given in Table 3.3, which shows a small difference between the theory and experiment.

Similarly, if keeping the dimension of the copper rod fixed and just changing the thickness of the titanium layer, as shown in Figure 3.6, the voltage of the Probe II increases with the thickness of titanium layer.

In this way, we can monitor the change of thickness or conductivity for the outer metal layer.

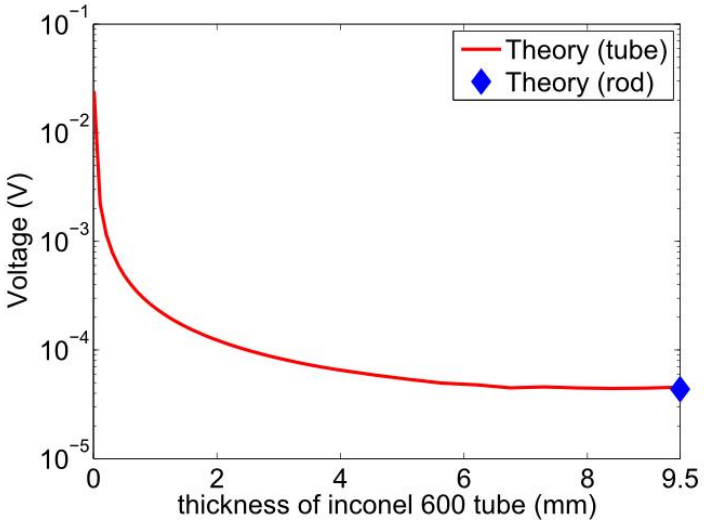

Figure 3.5 Calculated pick-up voltage (V) of collinear four-point Probe I on an inconel 600 tube (the outer radius and length are fixed), compared with the rod theory (filled diamond marker), as a function of the wall thickness.

3.7 Conclusion

In this paper, an analytical solution is presented to model the electric field of a uniform-layered conductive cylinder with finite length. Green's function satisfying Neumann boundary conditions is applied to derive the theory solution. And a group of four-point DCPD experiments are used to verify the theory solution, showing good agreements between the theory and experiment. These analytic solutions offer a non-destructive determination of the thickness or electrical conductivity of the layered cylinder if the other parameters are given. However, with more than four electrodes or by connecting electrodes in different configurations (38) one can determine both thickness and conductivity. Because DCPD method has the advantage of being independent of the magnetic permeability of the conductor, this technique can be applied to ferrous metals, while eddy current measurement can not (39; 40). Besides, this method can also work well for low conductivity materials such as semiconductors (41). In future, the analysis of four-point ACPD on a uniform-layered metal cylinder will be examined.

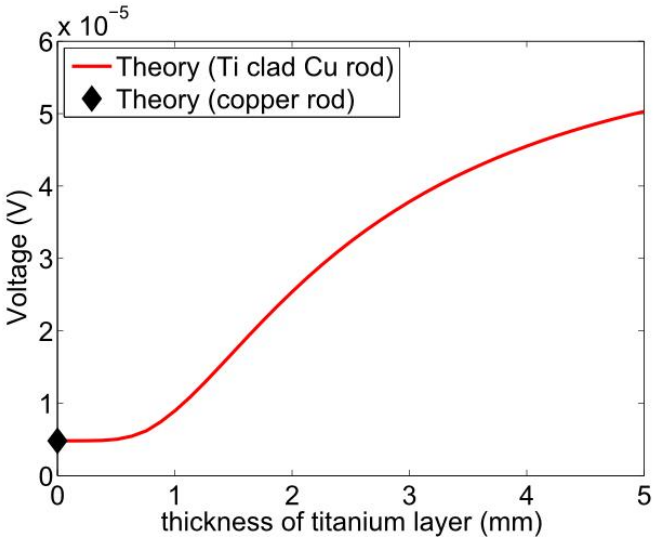

Figure 3.6 Calculated pick-up voltage (V) of the Probe II on a titanium clad copper rod (the radius of copper is fixed), compared with the rod theory (filled diamond marker), as a function of the thickness of titanium.

3.8 Acknowledgement

This work was supported by the NSF Industry University Cooperative Research Consortium at the Center for Nondestructice Evaluation, Iowa State University.

3.9 References

[1] Yamashita M, Nishii T and Kurihara H 1996 Resistivity correction factor for the four-point probe method on cylindrical materials *Jpn. J. Appl. Phys.* **35** 1948–53

[2] Yamashita M 2006 Measuring resistivity of hollow conducting cylinders with a four-probe array *Meas. Sci. Technol.* **17** 3323–7

[3] Valdes L B 1954 Resistivity measurements on germanium for transistors *Proc. IRE* **42** 420–7

[4] Lu Y, Bowler J R, Zhang C and Bowler N 2009 Edge effects in four point direct current potential drop measurement *Review of Progress in Quantitative Nondestructive Evaluation* vol 28 ed Thompson D O and Chimenti D E (New York: Plenum) pp 271–8

[5] Lu Y, Bowler N, Bowler J R and Huang Y 2009 Edge effects in four-point direct current potential drop measurements on metal plates *J. Phys. D: Appl. Phys.* **42** 135004

[6] Yamashita M 1987 Resistivity correction factor for four-probe method on circular semiconductors I *Jpn. J. Appl. Phys.* **26** 1550–4

[7] Kelekanjeri V S K G and Gerhardt R A 2008 A closed-form solution for the computation of geometric correction factors for four-point resistivity measurements on cylindrical specimens *Meas. Sci. Technol.* **19** 025701

[8] Yamashita M 1988 Resistivity correction factor for four-probe method on circular semiconductors II *Jpn. J. Appl. Phys.* **27** 1317–21

[9] Smits F M 1958 Measurement of sheet resistivities with the four-point probe *Bell Syst. Tech. J.* **37** 711–8

[10] Gegenwarth H H 1968 Correction factors for the four-point probe resistivity measurement on cylindrical semiconductors *Solid-State Electron.* **11** 787–9

[11] Murashima S, Kanamori H and Ishibashi F 1970 Correction devisors for the four-point probe resistivity measurement on cylindrical semiconductors *Jpn. J. Appl. Phys.* **9** 58–67

[12] Bowler N 2004 Analytical solution for the electric field in a half space conductor due to alternating current injected at the surface *J. Appl. Phys.* **95** 344–8

[13] Bowler N 2004 Electric field due to alternating current injected at the surface of a metal plate *J. Appl. Phys.* **96** 4607–13

[14] Bowler J R and Bowler N 2007 Theory of four-point alternating current potential drop measurements on conductive plates *Proc. R. Soc.* **463** 817–36

[15] Bowler J R 2011 Evaluation of the transient potential drop of a four-point probe *Appl. Phys. Lett.* **98** 264105

[16] Kelekanjeri V S K G and Gerhardt R A 2007 Electric field distribution within a metallic cylindrical specimen for the case of an ideal two-probe impedance measurement *J. Appl. Phys.* **101** 044904

[17] Worledge D C and Trouilloud P L 2003 Magnetoresistance measurement of unpatterned magnetic tunnel junction wafers by current-in-plane tunneling *Appl. Phys. Lett.* **83** 84–6

[18] Petersen D H, Hansen O, Lin R and Nielsen P F 2008 Micro-four-point probe Hall effect measurement method *J. Appl. Phys.* **104** 013710

[19] Petersen D H, Hansen O, Hansen T M, Bϕggild P and Lin R et al. 2010 Review of electrical characterization of ultra-shallow junctions with micro four-point probes *J. Vac. Sci. Technol. B* **28** C1C27-33

[20] Ju Y, Ju B and Saka M 2005 Microscopic four-point atomic force microscope probe technique for local electrical conductivity measurement *Rev. Sci. Instrum.* **76** 086101

[21] Shiraki I, Nagao T, Hasegawa S, Petersen C L, Bϕggild P, Hansen T M and Grey F 2000 Micro-four-point probes in a UHV scanning electron microscope for in-situ surface-conductivity measurements *Surf. Rev. Lett.* **7** 533–7

[22] Panseri C and Federighi T 1960 A resistometric study of pre-precipitation in Al-10% Zn *Acta Met.* **8** 217–38

[23] White R J, Fisher S B, Miller K M and Swallow G A 1974 A resistometric study of ageing in nimonic alloys (I). PE16 *J. Nucl. Mater.* **52** 51–8

[24] Bowler N 2006 Theory of four-point alternating current potential drop measurements on a metal half-space *J. Phys. D: Appl. Phys.* **39** 584–9

[25] Saguy H and Rittel D 2007 Application of ac tomography to crack identification *Appl. Phys. Lett.* **91** 084104

[26] Connolly M P, Michael D H and Collins R 1988 The inversion of surface potential measurements to determine crack size and shape *J. Appl. Phys.* **64** 2638–47

[27] Dougall J 1900 The determination of Green's function by means of cylindrical or spherical harmonics *Proc. Edin. Math. Soc.* **18** 33–83

[28] Gray A, Mathews G B and MacRobert M 1966 *A Treatise on Bessel Functions and Their Applications to Physics* 2nd edn (New York: Dover)

[29] Murashima S 1973 Neumann functions for Laplace's equation for a circular cylinder of finite length *Jpn. J. Appl. Phys.* **12** 1232–43

[30] Marshall S L and Redey L 1990 Mathematical analysis of a four-point conductivity probe for cylindrical samples *Rev. Sci. Instrum.* **61** 2659–65

[31] Felsen L B and Marcuvitz N 1973 *Radiation and Scattering of Waves* (Englewood Cliffs, NJ: Prentice-Hall)

[32] Abramowitz M and Stegun I A (ed) 1972 *Handbook of Mathematical Functions with Formulas, Graphs, and Mathematical Tables* (New York: Dover)

[33] Friedman B 1956 *Priciples and Techniques of Applied Mathematics* (New York: John Wiley and Sons)

[34] McLachlan N W 1948 *Bessel Functions for Engineers* (Oxford: Clarendon)

[35] Bowler N and Huang Y 2005 Model-based characterization of homogeneous metal plates using four-point alternating current potential drop measurements *IEEE Trans. Magn.* **41** 2102–10

[36] Bowler N and Huang Y 2005 Electrical conductivity measurement of metal plates using broadband eddy-current and four-point methods *Meas. Sci. Technol.* **16** 2193–200

[37] Bowler J R, Huang Y, Sun H, Brown J and Bowler N 2008 Alternating current potential-drop measurement of the depth of case hardening in steel rods *Meas. Sci. Technol.* **19** 075204

[38] Wang F, Petersen D H, Hansen T M, Henriksen T R, Bϕggild P and Hansen O 2010 Sensitivity study of micro four-point probe measurements on small samples *J. Vac. Sci. Technol. B* **28** C1C34-40

[39] Bowler N 2006 Theory of four-point direct-current potential drop measurements on a metal plate *Res. Nondestr. Eval.* **17** 29–48

[40] Bowler N 2011 Four-point potential drop measurements for materials characterization *Meas. Sci. Technol.* **22** 012001

[41] Schroder D K 1998 *Semiconductor Material and Device Characterization* (New York: Wiley)

CHAPTER 4. AN ANALYTICAL MODEL OF A FERRITE-CORED INDUCTOR USED AS AN EDDY CURRENT PROBE

A paper published in *The Journal of Applied Physics*

Yi Lu, John R. Bowler and Theodoros P. Theodoulidis

4.1 Abstract

An analytical model of an axisymmetric eddy current ferrite-cored probe above a multi-layered conducting half-space has been developed using a procedure in which the domain of the problem is truncated radially. This means that solutions can be expressed in the form of generalized Fourier-Bessel series. The expansion coefficients are found by matching the field across the interfaces between subregions of the problem. Initially the magnetic vector potential of a simple circular current filament is expanded in a series form. The solution is then modified to accommodate an infinitely long coaxial ferrite core and the principle of superposition is invoked to derive a coil field from the filament field in the presence of the core. Next we consider a semi-infinite core and then one of finite length. Finally the effects of a multi-layered conductor are included. Numerical predictions of probe impedance have been compared with experimental data showing excellent agreement.

4.2 Introduction

Eddy current nondestructive testing is widely used for the detection of surface and sub-surface flaws in conductive materials. The technique can also provide a means of measuring the conductivity of non-ferrous materials and to determine the thickness and conductivity of uniform metal layers (1). A ferrite core in an eddy current probe usually improves the signal-

to-noise ratio and resolution of defect detection, especially at a relative low working frequency (2). Compared with air-cored probes, the ferrite cored probe usually has a better performance, particular for the detection and characterization of deep surface flaws (3).

The use of an air-cored coil above a layered half space has been studied extensively (4; 5; 6; 1) due to the fact that the coil characteristics are relative easy to predict theoretically and measurements can be readily interpreted in terms of a well known model (7). Although there are a number of numerical methods available to predict ferrite cored probe fields (8; 9), it is of value to have instead an accurate analytical or semi-analytical method for finding the field and impedance of such probes, especially one that is relatively simple and easy to implement. This is possible for an axially symmetric ferrite cored probe whose core is a finite circular cylinder with linear material properties. Based on earlier analytical studies (10; 11; 12), expressions for the impedance and field of such a probe over a layered conductor have been developed by using the truncated region eigenfunction expansion (TREE) method (13). By radially truncating the domain of the problem, solutions can be developed in the form of series rather than by using integral forms. Imposing a boundary condition such as a zero tangential electric field on the truncation boundary, means that errors are introduced compared with the unbounded domain solution but the truncation errors can be made as small as desired by controlling the radius of the truncation boundary. The positive benefit of truncation is that it leads to a natural method of creating a discrete system of equations to solve for the series coefficients and thereby determine the probe field.

Integral forms involving Bessel functions of the first and second kinds can be used to represent the fields in the different strata shown in Figure 4.1, including those containing the ferrite core. However, in order to satisfy the field continuity conditions in an unbounded domain at planes through the ends of the ferrite cylinder, integral equations arise. Typically these would be solved using numerical schemes but a more natural approach is via a series solution that satisfies the field equations, albeit in a radially truncated domain. Rather than making a direct assault on the full truncated domain problem, as previously (13), the present development is incremental, proceeding via intermediate results that are useful in themselves. The approach provides insight into the way components of the problem introduced at different stages of de-

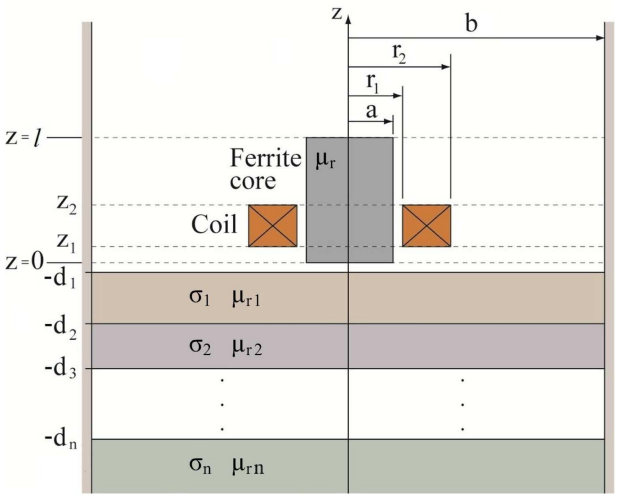

Figure 4.1 An axially symmetric ferrite-cored probe above a multi-layered conductive half space.

velopment are related in the end result. Starting with the field of a circular current filament in a radially truncated domain, we next construct a solution for a filament and a rectangular cross-section coil with an infinitely long circularly cylindrical ferrite core. Then deduce the field and impedance of a probe with finite length core. In constructing the finite core solution, we introduce reflection and transmission coefficient matrices that account for the core end effects. Finally the effect of a multi-layered conductor below the probe is taken into account.

4.3 Filament and Coil Field

4.3.1 Filament

It is helpful to compare an expression for the filament field in free space with that in a radially truncated domain in order to clarify the relationship between the two types of solution. In the quasi-static limit, the magnetic vector potential of a circular filament in the plane $z = z_0$ carrying a current I in an unbounded nonconducting space is a solution of a vector Laplace equation in two dimensions, having the form of an inverse Hankel transform,

$$\overset{\circ}{A}_\phi(\rho, z) = \int_0^\infty f(\kappa) J_1(\kappa\rho) e^{-\kappa|z-z_0|}\, \kappa d\kappa. \tag{4.1}$$

This expression takes account of the fact that the azimuthal electric field is continuous at $z = z_0$, a condition we write as $[E_\phi]_{z_0} = E_\phi(\rho, z_{0+}) - E_\phi(\rho, z_{0-}) = 0$. Subscripts $\pm$ refer to the limit of approach, in this case to z_0, from above and below respectively. The radial magnetic field on the other hand is discontinuous at $z = z_0$, the discontinuity being written $[H_\rho]_{z_0} = I\delta(\rho - \rho_0)$. By expressing this as

$$\left.\frac{\partial \mathring{A}_\phi}{\partial z}\right|_{z_{0+}} - \left.\frac{\partial \mathring{A}_\phi}{\partial z}\right|_{z_{0-}} = -\mu_0 I\delta(\rho - \rho_0), \tag{4.2}$$

and using the Hankel transform, one finds that $f(\kappa) = \frac{\mu_0 I\rho_0}{2\kappa} J_1(\kappa\rho_0)$ and that the vector potential for a circular current filament is

$$\mathring{A}_\phi(\rho, z) = \frac{\mu_0 I\rho_0}{2}\int_0^\infty J_1(\kappa\rho) J_1(\kappa\rho_0)\, e^{-\kappa|z-z_0|} d\kappa. \tag{4.3}$$

To find the equivalent expression for a radially truncated region radius b, using the TREE approach, assuming the tangential electric field vanishes on the truncation boundary, we express the vector potential as a Fourier-Bessel series,

$$\mathring{A}_\phi(\rho, z) = \sum_{i=1}^{\infty} c_i J_1(\kappa_i\rho)\, e^{-\kappa_i|z-z_0|}, \tag{4.4}$$

where κ_i, $i = 1, 2 \ldots \infty$ denotes the positive zeros of $J_1(\kappa_i b) = 0$. Using equation (4.2) and the orthogonality properties of the Bessel function $J_1(\kappa_i\rho)$ (14; 15), equation (4.62) of the Appendix, one finds that

$$\begin{aligned}\mathring{A}_\phi(\rho, z) &= \frac{\mu_0 I\rho_0}{b^2}\sum_{i=1}^{\infty}\frac{J_1(\kappa_i\rho) J_1(\kappa_i\rho_0)}{\kappa_i[J_0(\kappa_i b)]^2} e^{-\kappa_i|z-z_0|} \\ &= \mu_0 I\left\langle J_1(\boldsymbol{\kappa}\rho)\left|\frac{1}{2}\boldsymbol{\kappa}^{-1} e^{-\boldsymbol{\kappa}|z-z_0|}\mathring{\mathbf{A}}\right|\rho_0 J_1(\boldsymbol{\kappa}\rho_0)\right\rangle.\end{aligned} \tag{4.5}$$

The vector Dirac notation, considered from right to left, consist of a column vector multiplied by a matrix and by a row vector forming a scalar product. In general, this form represents a double summation but the main intension is to represent, in a clear symbolic way, the cross coupling between source and field vectors at horizontal planes due to the end effects of a ferrite core. However, in this case the matrix is diagonal and therefore only one summation is needed. The matrix includes the z-dependence of the vector potential as well as the term

$$\mathring{\mathbf{A}} = \mathbf{C}^{-1}, \tag{4.6}$$

where $\mathbf{C} = \frac{b}{2}[J_0(\boldsymbol{\kappa}\rho)]^2$ is defined in terms of the orthogonality properties of the Bessel functions as shown in Appendix A. Usually only 30 terms are used in the series for the calculation in air, for example, at $\rho = 1.5\rho_0$, $z = \rho_0$ and $z_0 = 0$, equation (4.4) gives a relative convergence error of 0.003% and a truncation error of about 0.15% with $b = 15\rho_0$. Incidentally, it is of interest to note that as $b \to \infty$, the summation of equation (4.5) becomes equivalent to the integral form equation (4.3) in the limit.

4.3.2 Coil Field and Impedance

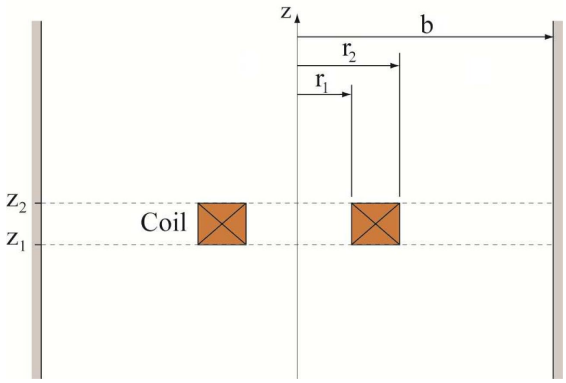

Figure 4.2 Air-cored coil of rectangular cross section.

For a coil cross section with a constant width, $r_2 - r_1$, finite length $z_2 - z_1$ and having N turns, Figure 4.2, the factor $\nu = N/[(r_2 - r_1)(z_2 - z_1)]$ is the coil turns density. The magnetic vector potential $A(\rho, z)$, of such a coil is found by approximating the current density in the coil as $\mathbf{J} = \nu I \mathbf{a}_\phi$ and integrating the filament potential over the cross-sectional area to give

$$\begin{aligned} A(\rho, z) &= \nu \int_{z_1}^{z_2} \int_{r_1}^{r_2} \overset{\circ}{A}_\phi(\rho, z)\, d\rho_0 dz_0 \\ &= \frac{\mu_0 I \nu}{2} \left\langle J_1(\boldsymbol{\kappa}\rho) \left| \boldsymbol{\kappa}^{-4} \left[2\mathbf{I} - e^{-\boldsymbol{\kappa}(z-z_1)} - e^{\boldsymbol{\kappa}(z-z_2)} \right] \overset{\circ}{\mathbf{A}} \right| \chi(\boldsymbol{\kappa} r_1, \boldsymbol{\kappa} r_2) \right\rangle, \end{aligned} \tag{4.7}$$

where

$$\chi(s_1, s_2) = \int_{s_1}^{s_2} x J_1(x)\, dx, \tag{4.8}$$

which can be evaluated in terms of Struve and Bessel functions(16). The complex power, $I^2 Z_0$ where Z_0 is the coil impedance, is given by

$$I^2 Z_0 = -\int_{\Omega_0} \mathbf{E}(\mathbf{r}) \cdot \mathbf{J}(\mathbf{r})\, d\mathbf{r}, \tag{4.9}$$

where Ω_0 is the coil region and ohmic losses are omitted. In this region, $\mathbf{E}$ is the electrical field and the current density $\mathbf{J} = \nu I \mathbf{a}_\phi$. Expressing the coil impedance in terms of the vector potential gives

$$\begin{aligned} Z_0 &= \frac{2\pi\jmath\omega\nu}{I}\int_{z_1}^{z_2}\int_{r_1}^{r_2} A(\rho,z)\,\rho d\rho dz \\ &= 2\pi\jmath\omega\mu_0\nu^2 \\ &\quad \left\langle \chi(\boldsymbol{\kappa}r_1,\boldsymbol{\kappa}r_2)\left|\boldsymbol{\kappa}^{-7}\left[(z_2-z_1)\boldsymbol{\kappa}-\mathbf{I}+e^{-\boldsymbol{\kappa}(z_2-z_1)}\right]\mathring{\mathbf{A}}\right|\chi(\boldsymbol{\kappa}r_1,\boldsymbol{\kappa}r_2)\right\rangle, \end{aligned} \tag{4.10}$$

which is purely imaginary and gives the self-inductance of the coil from $Z_0 = \jmath\omega L_0$.

4.4 Infinite Core

An infinite, circularly cylindrical, lossless, linear ferrite core, radius a, encircled by a coaxial current filament, Figure 4.3, gives rise to a vector potential of the form

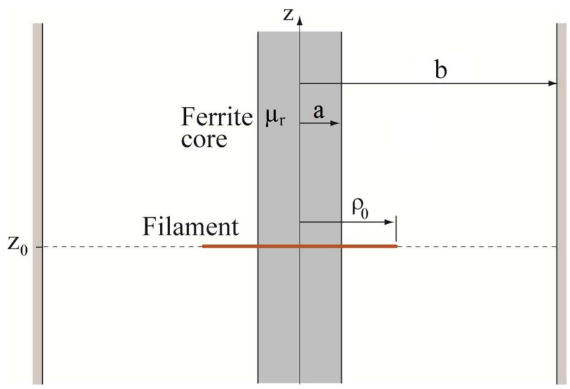

Figure 4.3 Filamentary coil with infinite long cylindrical ferrite core.

$$\begin{aligned} A_\phi(\rho,z) &= \mu_0 I\rho_0\sum_{i=1}^{\infty}\Psi_1(q_i\rho)\frac{e^{-q_i|z-z_0|}}{2q_i}A_i F_1(q_i\rho_0) \\ &= \mu_0 I\left\langle \Psi_1(\mathbf{q}\rho)\left|\frac{1}{2}\mathbf{q}^{-1}e^{-\mathbf{q}|z-z_0|}\mathbf{A}\right|\rho_0 F_1(\mathbf{q}\rho_0)\right\rangle, \end{aligned} \tag{4.11}$$

where

$$\Psi_n(q_i\rho) = \begin{cases} \mu_r J_n(q_i\rho) & (0\le\rho\le a) \\ F_n(q_i\rho) & (a<\rho\le b) \end{cases}, \tag{4.12}$$

and $F_1(\mathbf{q}\rho)$ is defined according to

$$F_n(\mathbf{q}\rho) = A_c(\mathbf{q}a)\,J_n(\mathbf{q}\rho) - B_c(\mathbf{q}a)\,Y_n(\mathbf{q}\rho), \tag{4.13}$$

with $n = 0, 1$. To ensure $A_\phi(b, z) = 0$, we define the q_i as the positive roots of $F_1(q_i b) = 0$. Then from the continuity of B_ρ and H_z at the ferrite core surface, at $\rho = a$, it is found that

$$A_c(q_i a) = \frac{\pi q_i a}{2}\left[\mu_r J_1(q_i a) Y_0(q_i a) - J_0(q_i a) Y_1(q_i a)\right] \tag{4.14}$$

and

$$B_c(q_i a) = \frac{\pi q_i a}{2}(\mu_r - 1) J_0(q_i a) J_1(q_i a). \tag{4.15}$$

The diagonal matrix $\mathbf{A}$ in (4.11), is determined by the discontinuity in the magnetic field at the plane $z = z_0$ of the filament, which, we recall, can be written $[H_\rho]_{z_0} = I\delta(\rho - \rho_0)$. As in the absence of the core, we use the discontinuity and the orthogonality properties of the radial eigenfunctions to define the coefficient matrix. In this case,

$$\mathbf{A} = \mathbf{D}^{-1}, \tag{4.16}$$

where $\mathbf{D}$ is given by equation (4.63). For $\mu_r = 1$ (air-cored case), the bracketed term in equation (4.14) become a Wronskian relation (15):

$$J_{m+1}(z) Y_m(z) - J_m(z) Y_{m+1}(z) = \frac{2}{\pi z}. \tag{4.17}$$

Then $A_c = 1$, $B_c = 0$, $F_n(\mathbf{q}\rho) = J_n(\mathbf{q}\rho)$, $\mathbf{q} = \boldsymbol{\kappa}$, $\mathbf{A} = \mathring{\mathbf{A}}$ and equation (4.11) reduces to equation (4.5), as it should.

The magnetic vector potential $A(\rho, z)$ in the region occupied by the turns of a rectangular cross-section circular coil is given by integrating with respect to the source coordinates over the coil cross-section, Figure 4.4, as in equation (4.7), to give

$$A(\rho, z) = \frac{\mu_0 I \nu}{2}\left\langle F_1(\mathbf{q}\rho)\left|\mathbf{q}^{-4}\left[2\mathbf{I} - e^{-\mathbf{q}(z-z_1)} - e^{\mathbf{q}(z-z_2)}\right]\mathbf{A}\right|\chi_F(\mathbf{q}r_1, \mathbf{q}r_2)\right\rangle \tag{4.18}$$

where

$$\chi_F(s_1, s_2) = \int_{s_1}^{s_2} x F_1(x)\, dx, \tag{4.19}$$

The corresponding impedance, accounting for the presence of an infinite linear lossless core, omitting ohmic losses, is found by integrating over the field coordinates to give,

$$Z = 2\pi\jmath\omega\mu_0\nu^2 \left\langle \chi_F(\mathbf{q}r_1, \mathbf{q}r_2)\left|\mathbf{q}^{-7}\left[(z_2 - z_1)\mathbf{q} - \mathbf{I} + e^{-\mathbf{q}(z_2 - z_1)}\right]\mathbf{A}\right|\chi_F(\mathbf{q}r_1, \mathbf{q}r_2)\right\rangle. \tag{4.20}$$

For $\mu_r = 1$, equation (4.20) reduces to equation (4.10), the core-free impedance, as required. This bring us to the point where the formalism can be extended to allow for core end effects.

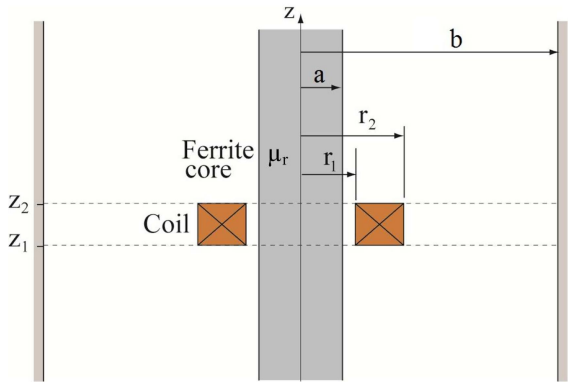

Figure 4.4 Rectangular cross coil with infinite long cylindrical ferrite core.

4.5 Semi-infinite Core

4.5.1 Filament Field

We consider next a semi-infinite core, Figure 4.5 by dividing the solution space at the base plane of the core where $z = 0$. The vector potential above the base plane is $A_\phi^{(1)}$ and below it is $A_\phi^{(0)}$. For region (1), the vector potential consists of the infinite core solution plus a term accounting for the core end effect. The latter is conveniently represented with the aid of a reflection matrix $\mathbf{R}_0$ and transmission matrix $\mathbf{T}_0$ coupling all radial eigenfunctions of the problem at the plane $z = 0$. Thus, the vector potential for region (1) is written

$$\begin{aligned} A_\phi^{(1)}(\rho,z) &= \mu_0 I \rho_0 \sum_{i=1}^{\infty} \Psi_1(q_i\rho)\frac{1}{2q_i}\left[e^{-q_i|z-z_0|}A_i F_1(q_i\rho_0) + e^{-q_i z}\sum_{j=1}^{\infty} R_{0ij}e^{-q_j z_0}A_j F_1(q_j\rho_0)\right] \\ &= \mu_0 I\left\langle \Psi_1(\mathbf{q}\rho)\left|\frac{1}{2}\mathbf{q}^{-1}(e^{-\mathbf{q}|z-z_0|} + e^{-\mathbf{q}z}\mathbf{R}_0 e^{-\mathbf{q}z_0})\mathbf{A}\right|\rho_0 F_1(\mathbf{q}\rho_0)\right\rangle, \end{aligned} \tag{4.21}$$

and for region (0),

$$\begin{aligned} A_\phi^{(0)}(\rho,z) &= \mu_0 I\rho_0 \sum_{i=1}^{\infty} J_1(\kappa_i\rho)\frac{e^{\kappa_i z}}{2\kappa_i}\sum_{j=1}^{\infty} T_{0ij}e^{-q_j z_0}A_j F_1(q_j\rho_0) \\ &= \mu_0 I\left\langle J_1(\boldsymbol{\kappa}\rho)\left|\frac{1}{2}\boldsymbol{\kappa}^{-1}e^{\boldsymbol{\kappa}z}\mathbf{T}_0 e^{-\mathbf{q}z_0}\mathbf{A}\right|\rho_0 F_1(\mathbf{q}\rho_0)\right\rangle. \end{aligned} \tag{4.22}$$

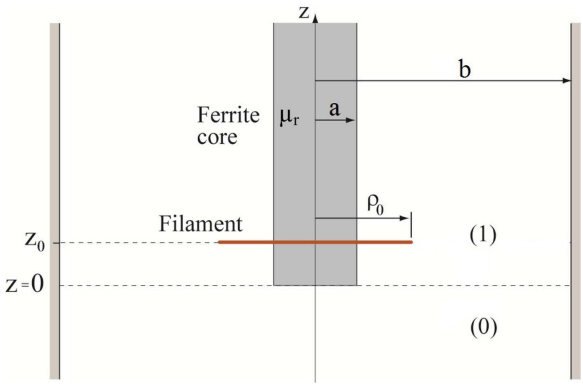

Figure 4.5 Filamentary current loop coil encircling a semi-infinite cylindrical ferrite core. The plane through the base of the core divides the space into regions (0) and (1) as shown.

The continuity of the radial magnetic field at the base plane, written $[H_\rho]_0 = \left[-\frac{1}{\mu(\rho)}\frac{\partial A_\phi}{\partial z}\right]_0 = 0$, is satisfied in the weak sense (17) at the plane $z = 0$ by taking moments of the z-derivative of equations (4.21) and (4.22) with $J_1(\kappa_i\rho)$. As a result, one obtains a relationship of the form

$$\mathbf{U}(\mathbf{I} - \mathbf{R}_0) = \mathbf{C}\mathbf{T}_0. \tag{4.23}$$

Similarly, the continuity of the normal magnetic flux density, written $[B_z]_0 = \left[\frac{1}{\rho}\frac{\partial(\rho A_\phi)}{\partial\rho}\right]_0 = 0$, is applied by taking moments of equations (4.21) and (4.22) using $J_0(\kappa_i\rho)$ to give

$$\mathbf{V}(\mathbf{I} + \mathbf{R}_0) = \mathbf{C}\mathbf{T}_0, \tag{4.24}$$

where $\mathbf{U}$ and $\mathbf{V}$ are defined in Appendix A along with and $\mathbf{C}$ which was referred to previously. Solving for the reflection and transmission matrices gives

$$\mathbf{R}_0 = (\mathbf{U} + \mathbf{V})^{-1}(\mathbf{U} - \mathbf{V}) \tag{4.25}$$

and

$$\mathbf{T}_0 = \frac{1}{2}\mathbf{C}^{-1}\left[(\mathbf{U} + \mathbf{V}) - (\mathbf{U} - \mathbf{V})\,\mathbf{R}_0\right]. \tag{4.26}$$

When $z_0 \to \infty$, $e^{-\mathbf{q}z_0} \to 0$, then equation (4.21) reduces to the expression for the infinite core vector potential, equation (4.11), as required.

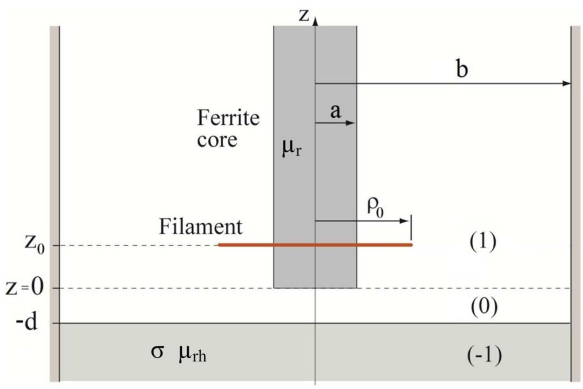

Figure 4.6 Filamentary current loop coil encircling a semi-infinite cylindrical ferrite core above a uniform conductive half-space.

4.5.2 Effect of a Uniform Conductor

The introduction of a half-space conductor can now be taken into account by recognizing that its effect in region (1), Figure 4.6, can be represented by a modified core-base reflection matrix. equation (4.21), is therefore adapted by replacing $\mathbf{R}_0$ with $\mathbf{R}$, which is to be determined. With this change, the vector potential for region (1) is written

$$A_\phi^{(1)}(\rho,z) = \mu_0 I\left\langle \Psi_1(\mathbf{q}\rho)\left|\frac{1}{2}\mathbf{q}^{-1}(e^{-\mathbf{q}|z-z_0|}+e^{-\mathbf{q}z}\mathbf{R}e^{-\mathbf{q}z_0})\mathbf{A}\right|\rho_0 F_1(\mathbf{q}\rho_0)\right\rangle. \quad (4.27)$$

Similarly equation (4.22) is replaced by one with a modified transmission matrix and a term included to account for reflection from the conductor. The latter does not couple eigenfunctions with dissimilar eigenvalues and therefore it can be represented by a diagonal matrix, $\mathbf{\Gamma}$ say. Thus instead of $e^{\boldsymbol{\kappa}z}\mathbf{T}_0e^{-\mathbf{q}z_0}$ in equation (4.22) we have $(e^{\boldsymbol{\kappa}z}+e^{-\boldsymbol{\kappa}z}\mathbf{\Gamma})\,\mathbf{T}e^{-\mathbf{q}z_0}$. Then for region (0), Figure 4.6, the vector potential has the form

$$A_\phi^{(0)}(\rho,z) = \mu_0 I\left\langle J_1(\boldsymbol{\kappa}\rho)\left|\frac{1}{2}\boldsymbol{\kappa}^{-1}(e^{\boldsymbol{\kappa}z}+e^{-\boldsymbol{\kappa}z}\mathbf{\Gamma})\,\mathbf{T}e^{-\mathbf{q}z_0}\mathbf{A}\right|\rho_0 F_1(\mathbf{q}\rho_0)\right\rangle. \quad (4.28)$$

The reflection coefficient due a uniform conductor, well known in a variety contexts, we deduce for the quasi-static limit by considering the continuity of the tangential electromagnetic field at the surface $z=-d$. This yields the expression

$$\mathbf{\Gamma} = e^{-2\boldsymbol{\kappa}d}(\boldsymbol{\kappa}+\boldsymbol{\gamma})^{-1}(\boldsymbol{\kappa}-\boldsymbol{\gamma}), \quad (4.29)$$

where $\boldsymbol{\gamma} = [\gamma_{ij}]$ and $\gamma_{ij} = \sqrt{\kappa_{ij}^2 + \jmath\omega\mu_0\mu_{rh}\sigma}\delta_{ij}/\mu_{rh}$. Here δ_{ij} is the Kronecker delta, equal to unity for $i = j$ and zero otherwise. Appendix B gives the corresponding reflection coefficient for a piecewise uniform stratified conductive region.

The remaining task for this section is to determine $\mathbf{R}$ and $\mathbf{T}$ accounting for the presence of the conductor. Applying the continuity of H_ρ and B_z at $z = 0$, using equations (4.27), and (4.28) and taking moments as before, one finds that

$$\mathbf{U}(\mathbf{I} - \mathbf{R}) = (\mathbf{I} - \boldsymbol{\Gamma})\mathbf{C}\mathbf{T} \tag{4.30}$$

and

$$\mathbf{V}(\mathbf{I} + \mathbf{R}) = (\mathbf{I} + \boldsymbol{\Gamma})\mathbf{C}\mathbf{T}. \tag{4.31}$$

Solving for the reflection and transmission matrices gives

$$\mathbf{R} = \left[(\mathbf{U} + \mathbf{V}) + \boldsymbol{\Gamma}\,(\mathbf{U} - \mathbf{V})\right]^{-1}\left[(\mathbf{U} - \mathbf{V}) + \boldsymbol{\Gamma}\,(\mathbf{U} + \mathbf{V})\right] \tag{4.32}$$

and

$$\mathbf{T} = \frac{1}{2}\mathbf{C}^{-1}\left[(\mathbf{U} + \mathbf{V}) - (\mathbf{U} - \mathbf{V})\,\mathbf{R}\right]. \tag{4.33}$$

For $\sigma = 0$ (without the conducting region), we find that $\boldsymbol{\gamma} = \boldsymbol{\kappa}$, $\boldsymbol{\Gamma} = \mathbf{0}$, $\mathbf{R} = \mathbf{R}_0$ and $\mathbf{T} = \mathbf{T}_0$. Then equation (4.27) reduces to equation (4.21) and equation (4.28) to equation (4.22). Having established a procedure to account for a conductive region, we can extend it to deal with the case of a finite length core. First, however, we consider a finite core in the absence of a conductor.

4.6 Finite Length Core

4.6.1 Filament Field

To find the field of a finite length circularly cylindrical ferrite core, Figure 4.7, the solution space is divided at the end planes of the core, at $z = l$ and $z = 0$. The vector potential for the three regions thus created, can be written in the general form

$$A_\phi^{(2)}(\rho, z) = \mu_0 I \left\langle J_1(\boldsymbol{\kappa}\rho) \left| \frac{1}{2}\boldsymbol{\kappa}^{-1} e^{-\boldsymbol{\kappa}(z-l)}\mathbf{T}_{t0}\mathbf{A} \right| \rho_0 F_1(\mathbf{q}\rho_0) \right\rangle, \tag{4.34}$$

$$A_\phi^{(1)}(\rho, z) = \mu_0 I \left\langle \Psi_1(\mathbf{q}\rho) \left| \frac{1}{2}\mathbf{q}^{-1}\left[e^{-\mathbf{q}|z-z_0|} + e^{-\mathbf{q}z}\mathbf{R}_{b0} + e^{\mathbf{q}(z-l)}\mathbf{R}_{t0}\right]\mathbf{A} \right| \rho_0 F_1(\mathbf{q}\rho_0) \right\rangle \tag{4.35}$$

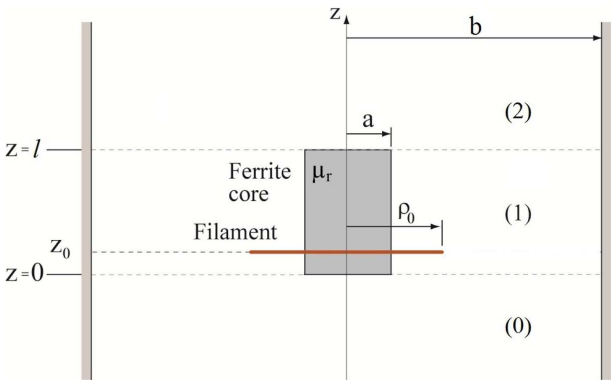

Figure 4.7 A filamentary current loop is shown coaxial with a finite length cylindrical ferrite core. The plane through the base of the core divides the space into regions (0), (1) and (2) as shown.

and

$$A_{\phi}^{(0)}(\rho, z) = \mu_0 I \left\langle J_1(\boldsymbol{\kappa}\rho) \left| \frac{1}{2} \boldsymbol{\kappa}^{-1} e^{\boldsymbol{\kappa} z} \mathbf{T}_{\mathrm{b0}} \mathbf{A} \right| \rho_0 F_1(\mathbf{q}\rho_0) \right\rangle, \tag{4.36}$$

where $\mathbf{T}_{\mathrm{t0}}$, $\mathbf{T}_{\mathrm{b0}}$, $\mathbf{R}_{\mathrm{b0}}$ and $\mathbf{R}_{\mathrm{t0}}$ are matrices that can be related to those already defined, namely $\mathbf{T}_0$ and $\mathbf{R}_0$ and we need to find these relationships. Note that the subscripts t and b refer to the top and bottom of the core respectively. Given the properties of the reflection matrix defined for the semi-infinite core, $\mathbf{R}_0$, one can take account of multiple reflections between the planes at the ends of the finite core by noting that

$$\mathbf{R}_{\mathrm{b0}} = \mathbf{R}_0 \left(e^{-\mathbf{q}z_0} + e^{-\mathbf{q}l} \mathbf{R}_{\mathrm{t0}} \right). \tag{4.37}$$

Similarly for the field at $z = l$, we find that

$$\mathbf{R}_{\mathrm{t0}} = \mathbf{R}_0 e^{-\mathbf{q}l} \left(e^{\mathbf{q}z_0} + \mathbf{R}_{\mathrm{b0}} \right). \tag{4.38}$$

Solving equations (4.37) and (4.38) for $\mathbf{R}_{\mathrm{b0}}$ and $\mathbf{R}_{\mathrm{t0}}$, we get

$$\mathbf{R}_{\mathrm{b0}} = \mathbf{G}^{-1} \mathbf{R}_0 \left[\mathbf{I} + e^{-\mathbf{q}l} \mathbf{R}_0 e^{-\mathbf{q}(l-2z_0)} \right] e^{-\mathbf{q}z_0} \tag{4.39}$$

and

$$\mathbf{R}_{\mathrm{t0}} = \mathbf{G}^{-1} \mathbf{R}_0 \left[\mathbf{I} + e^{-\mathbf{q}l} \mathbf{R}_0 e^{\mathbf{q}(l-2z_0)} \right] e^{-\mathbf{q}(l-z_0)}, \tag{4.40}$$

where

$$\mathbf{G} = \mathbf{I} - \mathbf{R}_0 e^{-\mathbf{q}l} \mathbf{R}_0 e^{-\mathbf{q}l}. \tag{4.41}$$

In equations (4.34) and (4.36), $\mathbf{T}_{t0}$ and $\mathbf{T}_{b0}$ are transmission matrices defined with respect to the interfaces at $z = l$ and $z = 0$. Applying the continuity of H_ρ and B_z at $z = l$ as in Section IV, we get

$$\mathbf{C}\mathbf{T}_{t0} = \mathbf{U}\left[e^{-\mathbf{q}(l-z_0)} + e^{-\mathbf{q}l}\mathbf{R}_{b0} - \mathbf{R}_{t0}\right] \tag{4.42}$$

and

$$\mathbf{C}\mathbf{T}_{t0} = \mathbf{V}\left[e^{-\mathbf{q}(l-z_0)} + e^{-\mathbf{q}l}\mathbf{R}_{b0} + \mathbf{R}_{t0}\right]. \tag{4.43}$$

Solving equations (4.42) and (4.43) for $\mathbf{T}_{t0}$ gives

$$\mathbf{T}_{t0} = \mathbf{T}_0 e^{-\mathbf{q}l}\left(e^{\mathbf{q}z_0} + \mathbf{R}_{b0}\right). \tag{4.44}$$

Similarly,

$$\mathbf{T}_{b0} = \mathbf{T}_0\left(e^{-\mathbf{q}z_0} + e^{-\mathbf{q}l}\mathbf{R}_{t0}\right). \tag{4.45}$$

For $l \to \infty$, $e^{-\mathbf{q}l} \to 0$, $\mathbf{G} \to \mathbf{I}$, $\mathbf{R}_{b0} \to \mathbf{R}_0 e^{-\mathbf{q}z_0}$, $\mathbf{R}_{t0} \to 0$, $\mathbf{T}_{t0} \to 0$, $\mathbf{T}_{b0} \to \mathbf{T}_0 e^{-\mathbf{q}z_0}$ and $A_\phi^{(2)}(z, \rho) \to 0$, then equations (4.35) and (4.36) agree with equations (4.21) and (4.22).

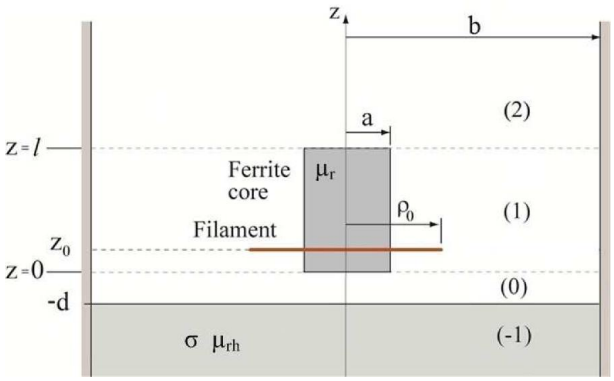

Figure 4.8 Filamentary coil with a finite long cylindrical ferrite core above a uniform conductive half-space.

4.6.2 Effect of a Uniform Conductor

Our final change to the structure is to introduce the effect of the conductor located below a finite length cylindrical ferrite probe, Figure 4.8. In constructing the updated solution, one can reuse equations (4.34) and (4.35) but $\mathbf{T}_t$, $\mathbf{R}_b$ and $\mathbf{R}_t$ replace $\mathbf{T}_{t0}$, $\mathbf{R}_{b0}$ and $\mathbf{R}_{t0}$ to account

for the modified field. In place of equation (4.36) we have

$$A_{\phi}^{(0)}(\rho,z) = \mu_0 I\left\langle J_1(\boldsymbol{\kappa}\rho)\left|\frac{1}{2}\boldsymbol{\kappa}^{-1}\left(e^{\boldsymbol{\kappa}z}+e^{-\boldsymbol{\kappa}z}\boldsymbol{\Gamma}\right)\mathbf{T}_{\mathrm{b}}\mathbf{A}\right|\rho_0 F_1(\mathbf{q}\rho_0)\right\rangle, \tag{4.46}$$

where $\boldsymbol{\Gamma}$ is given by equation (4.29) and $\mathbf{T}_{\mathrm{b0}}$ is replaced by $\mathbf{T}_{\mathrm{b}}$ to account for the presence of the conductor. The field at the plane $z = 0$ is characterized by a reflection coefficient $\mathbf{R}$, equation (4.32), that compounds effects of the core base and the conductor. Using this coefficient, we find that

$$\mathbf{R}_{\mathrm{b}} = \mathbf{R}\left(e^{-\mathbf{q}z_0}+e^{-\mathbf{q}l}\mathbf{R}_{\mathrm{t}}\right) \tag{4.47}$$

and

$$\mathbf{R}_{\mathrm{t}} = \mathbf{R}_0 e^{-\mathbf{q}l}\left(e^{\mathbf{q}z_0}+\mathbf{R}_{\mathrm{b}}\right). \tag{4.48}$$

Then solving for $\mathbf{R}_{\mathrm{b}}$ and $\mathbf{R}_{\mathrm{t}}$ gives

$$\mathbf{R}_{\mathrm{b}} = \mathbf{G}_1^{-1}\mathbf{R}\left[\mathbf{I}+e^{-\mathbf{q}l}\mathbf{R}_0 e^{-\mathbf{q}(l-2z_0)}\right]e^{-\mathbf{q}z_0} \tag{4.49}$$

and

$$\mathbf{R}_{\mathrm{t}} = \mathbf{G}_2^{-1}\mathbf{R}_0\left[\mathbf{I}+e^{-\mathbf{q}l}\mathbf{R}e^{\mathbf{q}(l-2z_0)}\right]e^{-\mathbf{q}(l-z_0)}, \tag{4.50}$$

where

$$\mathbf{G}_1 = \mathbf{I}-\mathbf{R}e^{-\mathbf{q}l}\mathbf{R}_0 e^{-\mathbf{q}l}, \tag{4.51}$$

$$\mathbf{G}_2 = \mathbf{I}-\mathbf{R}_0 e^{-\mathbf{q}l}\mathbf{R}e^{-\mathbf{q}l}. \tag{4.52}$$

Applying the continuity of H_ρ and B_z at $z = 0$ gives,

$$(\mathbf{I}-\boldsymbol{\Gamma})\,\mathbf{C}\mathbf{T}_{\mathrm{b}} = \mathbf{U}\left(e^{-\mathbf{q}z_0}-\mathbf{R}_{\mathrm{b}}+e^{-\mathbf{q}l}\mathbf{R}_{\mathrm{t}}\right) \tag{4.53}$$

and

$$(\mathbf{I}+\boldsymbol{\Gamma})\,\mathbf{C}\mathbf{T}_{\mathrm{b}} = \mathbf{V}\left(e^{-\mathbf{q}z_0}+\mathbf{R}_{\mathrm{b}}+e^{-\mathbf{q}l}\mathbf{R}_{\mathrm{t}}\right). \tag{4.54}$$

From equations (4.53) and (4.54) we get

$$\mathbf{T}_{\mathrm{b}} = \mathbf{T}\left(e^{-\mathbf{q}z_0}+e^{-\mathbf{q}l}\mathbf{R}_{\mathrm{t}}\right), \tag{4.55}$$

where $\mathbf{T}$ is given by equation (4.33). Similarly, using the continuity of H_ρ and B_z at $z = l$ gives

$$\mathbf{T}_{\mathrm{t}} = \mathbf{T}_0 e^{-\mathbf{q}l}\left(e^{\mathbf{q}z_0}+\mathbf{R}_{\mathrm{b}}\right). \tag{4.56}$$

For the special case $\sigma = 0$, $\boldsymbol{\gamma} = \boldsymbol{\kappa}$, $\boldsymbol{\Gamma} = \mathbf{0}$, $\mathbf{R} = \mathbf{R}_0$, $\mathbf{T} = \mathbf{T}_0$, $\mathbf{G}_1 = \mathbf{G}_2 = \mathbf{G}$, equation (4.46) reduces to equation (4.36). Having found the required reflection and transmission coefficients for the problem, we summarize below, the probe field and impedances expressions for an inductor with a finite length core.

4.6.3 Coil Field and Impedance

The vector potential in region (1) where $a < \rho \leq b$, due to a circular filament radius ρ_0 concentric with a finite length ferrite core above a uniform conductor, Figure 4.8, is

$$A_{\phi}^{(1)}(\rho, z) = \mu_0 I \Big\langle F_1(\mathbf{q}\rho) \Big| \frac{1}{2}\mathbf{q}^{-1}\left[e^{-\mathbf{q}|z-z_0|} + e^{-\mathbf{q}z}\mathbf{R}_{\mathrm{b}} + e^{\mathbf{q}(z-l)}\mathbf{R}_{\mathrm{t}}\right]\mathbf{A} \Big| \rho_0 F_1(\mathbf{q}\rho_0) \Big\rangle. \quad (4.57)$$

By integrating the filament potential, the magnetic vector potential of the ferrite cored probe in the presence of the conductor is given by

$$\begin{aligned} A(\rho, z) &= \nu \int_{z_1}^{z_2}\int_{r_1}^{r_2} A_{\phi}^{(1)}(\rho, z)\, d\rho_0 dz_0 \\ &= \frac{\mu_0 I \nu}{2}\Big\langle F_1(\mathbf{q}\rho) \Big| \mathbf{q}^{-1}\Big\{2\mathbf{I} - e^{\mathbf{q}(z-z_1)} - e^{-\mathbf{q}(z-z_2)} \\ &\quad + e^{-\mathbf{q}z}\mathbf{G}_1^{-1}\left[\mathbf{R}\left(e^{-\mathbf{q}z_1} - e^{-\mathbf{q}z_2}\right) + \left(e^{\mathbf{q}z_2} - e^{\mathbf{q}z_1}\right)\right] \\ &\quad + e^{\mathbf{q}(z-l)}\mathbf{G}_2^{-1}\left[e^{\mathbf{q}l}\left(e^{-\mathbf{q}z_1} - e^{-\mathbf{q}z_2}\right) + \mathbf{R}_0 e^{-\mathbf{q}l}\left(e^{\mathbf{q}z_2} - e^{\mathbf{q}z_1}\right)\right]\Big\}\mathbf{q}^{-3}\mathbf{A} \Big| \chi_F(\mathbf{q}r_1, \mathbf{q}r_2)\Big\rangle. \end{aligned} \quad (4.58)$$

As in equation (4.10), the coil impedance can be found by integrating with respect to the field coordinates over the coil region. This gives

$$\begin{aligned} Z &= \jmath\omega\pi\mu_0\nu^2\Big\langle \chi_F(\mathbf{q}r_1, \mathbf{q}r_2) \Big| \mathbf{q}^{-4}\Big\{2(z_2 - z_1)\mathbf{q} + 2\mathbf{I} - 2e^{\mathbf{q}(z_2 - z_1)} \\ &\quad + \left(e^{-\mathbf{q}z_1} - e^{-\mathbf{q}z_2}\right)\mathbf{G}_1^{-1}\left[\mathbf{R}\left(e^{-\mathbf{q}z_1} - e^{-\mathbf{q}z_2}\right) + \left(e^{\mathbf{q}z_2} - e^{\mathbf{q}z_1}\right)\right] \\ &\quad + \left(e^{\mathbf{q}z_2} - e^{\mathbf{q}z_1}\right)e^{-\mathbf{q}l}\mathbf{G}_2^{-1}\left[e^{\mathbf{q}l}\left(e^{-\mathbf{q}z_1} - e^{-\mathbf{q}z_2}\right) + \mathbf{R}_0 e^{-\mathbf{q}l}\left(e^{\mathbf{q}z_2} - e^{\mathbf{q}z_1}\right)\right]\Big\}\mathbf{q}^{-3}\mathbf{A} \Big| \chi_F(\mathbf{q}r_1, \mathbf{q}r_2)\Big\rangle. \end{aligned} \quad (4.59)$$

An important special case, Figure 4.9, is that of a lossless ferrite-cored inductor in free space whose impedance can be obtained from equation (4.59) by removing the effects of the conductor. This gives

$$Z_0 = \jmath\omega\pi\mu_0\nu^2\Big\langle \chi_F(\mathbf{q}r_1, \mathbf{q}r_2) \Big| \mathbf{q}^{-4}\Big\{2(z_2 - z_1)\mathbf{q} + 2\mathbf{I} - 2e^{\mathbf{q}(z_2 - z_1)}$$

$$+\left(e^{-\mathbf{q}z_1}-e^{-\mathbf{q}z_2}\right)\mathbf{G}^{-1}\left[\mathbf{R}_0\left(e^{-\mathbf{q}z_1}-e^{-\mathbf{q}z_2}\right)+\left(e^{\mathbf{q}z_2}-e^{\mathbf{q}z_1}\right)\right]$$
$$+\left(e^{\mathbf{q}z_2}-e^{\mathbf{q}z_1}\right)e^{-\mathbf{q}l}\mathbf{G}^{-1}\left[e^{\mathbf{q}l}\left(e^{-\mathbf{q}z_1}-e^{-\mathbf{q}z_2}\right)+\mathbf{R}_0e^{-\mathbf{q}l}\left(e^{\mathbf{q}z_2}-e^{\mathbf{q}z_1}\right)\right]\Big\}\mathbf{q}^{-3}\mathbf{A}\Big|\chi_F\left(\mathbf{q}r_1,\mathbf{q}r_2\right)\Big\rangle. \tag{4.60}$$

Because the free-space inductor is lossless, putting $Z_0=\jmath\omega L_0$ gives the self inductance.

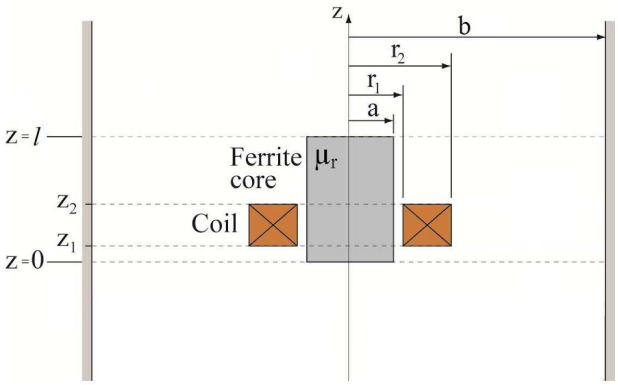

Figure 4.9 An axially symmetric ferrite-cored probe.

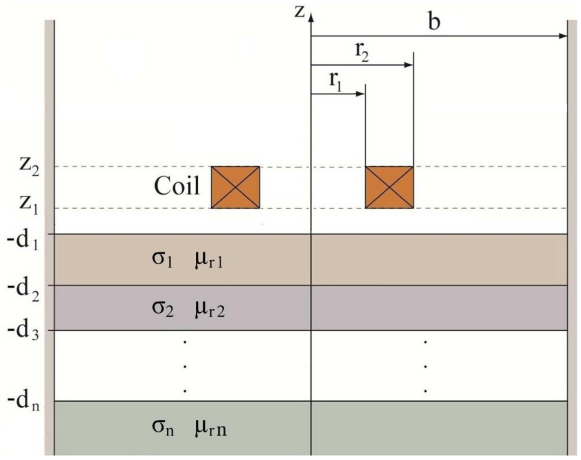

Figure 4.10 An axially symmetric air-cored probe above a multi-layered conductive half space.

In addition, we deduce from (4.59) the impedance of a coil without a core above a multi-layered planar conductor in a radially truncated domain, Figure 4.10. This impedance can be found by putting $\mathbf{q}=\boldsymbol{\kappa}$, $\mathbf{A}=\mathring{\mathbf{A}}$, $\chi_F\left(\mathbf{q}r_1,\mathbf{q}r_2\right)=\chi\left(\boldsymbol{\kappa}r_1,\boldsymbol{\kappa}r_2\right)$, $\mathbf{R}_0=0$, $\mathbf{R}=\boldsymbol{\Gamma}$, and $\mathbf{G}_1=\mathbf{G}_2=\mathbf{G}=\mathbf{I}$, to give

$$Z = \jmath\omega\pi\mu_0\nu^2\Big\langle\chi\left(\boldsymbol{\kappa}r_1\boldsymbol{\kappa}r_2\right)\Big|\boldsymbol{\kappa}^{-7}\Big\{2\left(z_2-z_1\right)\boldsymbol{\kappa}-2\mathbf{I}$$

$$+2e^{-\boldsymbol{\kappa}(z_2-z_1)} + \left(e^{-\boldsymbol{\kappa}z_1} - e^{-\boldsymbol{\kappa}z_2}\right)\boldsymbol{\Gamma}\left(e^{-\boldsymbol{\kappa}z_1} - e^{-\boldsymbol{\kappa}z_2}\right)\Big\}\mathring{\mathbf{A}}\Big|\chi\left(\boldsymbol{\kappa}r_1, \boldsymbol{\kappa}r_2\right)\Big\rangle. \quad (4.61)$$

Without the conductor, $\boldsymbol{\Gamma} = 0$ and equation (4.61) reduces to equation (4.10).

4.7 Experiment and Discussion

To verify the analytical results, we have performed experiments using an eddy current probe with a ferrite core on layered test pieces. The probe dimensions are shown in Table 4.1 and Table 4.2 gives the test piece parameters. The experiment results are obtained by using an Agilent 4294A Precision Impedance Analyzer.

Table 4.1 Parameters of the coil and ferrite core. Unit of dimensions is mm and uncertainty is 0.01 mm.

Coil		**Ferrite core**	
Inner diameter $2r_1$	10.05	Diameter $2a$	7.76
Outer diameter $2r_2$	20.40	Length l	29.95
Length $z_2 - z_1$	18.18	Liftoff d_1	0.59
Offset z_1	2.65	Rel. permeability μ_r	250
Number of turns N	776		
DC resistance	8.09 Ω		

Table 4.2 Parameters of metal plates. Conductivity σ, thickness T and lateral dimensions $w \times l$. Uncertainty in thickness is 0.01 mm and in lateral dimensions is 1 mm.

Metal	$\boldsymbol{\sigma}$ **(MS/m)**	**T (mm)**	$\boldsymbol{w \times l}$ (mm)
Aluminum (7075)	20.4±0.4	25.37	615×616
Brass (C2600)	16.42±0.09	5.66	615×616
Aluminum (2042)	17.58±0.09	1.59	152×203
Ti-6Al-4V	0.58±0.01	12.47	318×331

The radius of the truncated domain b is selected to ensure that the truncation error is of the order of 0.2%. With the given dimensions of the coil and ferrite core, b is chosen to be 15 times the outer radius of the coil and 100 terms are used in the summation to achieve a good convergence in the numerical calculations, even if there is a nonconducting layer in the test piece. By using equations (4.10) and (4.60), we can get the impedances of the probe, without and with a ferrite core in air and hence the self-inductance L_0 can be found for both cases. The calculated and measured values of free-space self-inductance are given in Table 4.3.

Table 4.3 Calculated and measured DC inductance for the coil with and without the ferrite core.

μ_r	Measured (mH)	Calculated (mH)
1	4.149	4.155
250	19.27	19.32

4.7.1 Truncated Half-space Conductor

For this case, the test piece is a large aluminum 7075 plate. Its thickness is at least 5 times that of the skin depth at the lowest measurement frequency and the surface of the plate large enough that edge effects can be neglected. Calculations using a conductor of infinite thickness should therefore approximate the measurements. The comparison of the analytical evaluations and experimental results in Figure 4.11 shows a good agreement. On average, the difference between theoretical predictions and experimental measurements of absolute impedance is 0.5%.

4.7.2 Two-layer Case

To verify the model predictions for a two-layer case, a large thin brass C2600 plate (as the upper layer) is used in the experiment with the air below being the second layer. The experimental coil impedance data are compared with the theory curves in Figure 4.12. For the two layer case, only $\mathbf{\Gamma}_1$ must be calculated in advance to determine $\mathbf{\Gamma}$ as required for equations (4.66)-(4.68). Figure 4.12, shows that the experiment results are predicted accurately by the two-layer model, which can be used to determine the thickness and conductivity of a conductive plate. Furthermore, especially in the low frequency range, there are obvious differences between the calculated results based on the models of the two-layer and half-space structure, which verifies that at low frequency, the thin plate can not be treated as a half-space conductor.

4.7.3 Three-layer Case

A thin aluminum 2042 plate and a thicker titanium Ti-6Al-4V plate were chosen to validate the three-layer model. In the experiment, the aluminum plate is the upper layer, the titanium alloy plate is the middle layer and air is the bottom layer. In Figure 4.13, the coil impedance

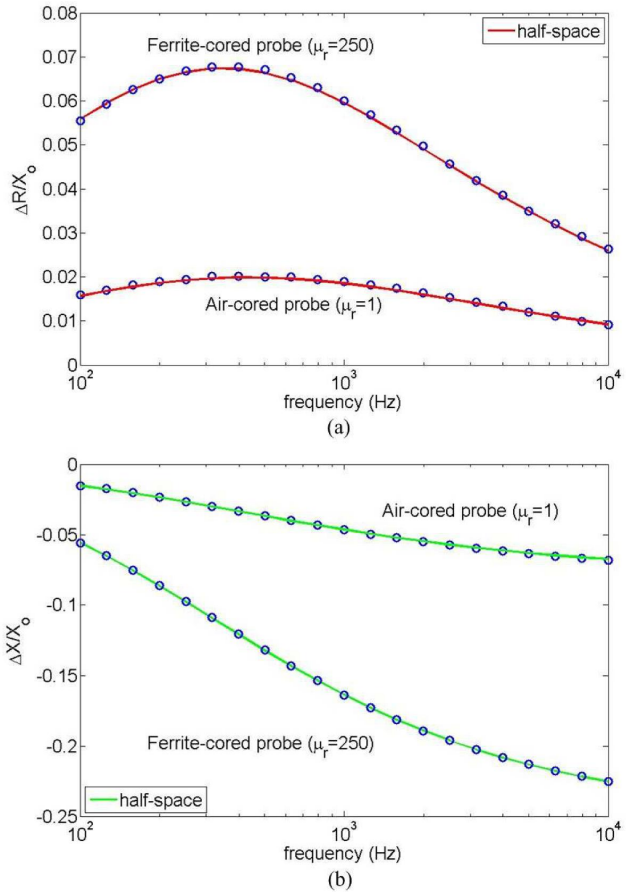

Figure 4.11 Normalized impedance change as a function of frequency for an air-cored coil (μ_r=1) and ferrite-cored coils (μ_r=250) due to the aluminum 7075 plate. Circles are experiment data and solid lines are theory results.

measurements are compared with the theoretical calculation. In this case, $\mathbf{\Gamma}_2$, $\mathbf{\Gamma}_1$ and $\mathbf{\Gamma}$ are derived in sequence. The agreement is also quite good for this case.

4.8 Conclusion

In this article, the TREE method for a ferrite-cored coil above a multi-layered conducting plates has been studied. Reflection and transmission coefficient matrices due to the end effects of the ferrite core have been introduced. By using a recursion relationship we have determined the reflection coefficient of a conductor with an arbitrary number of uniform layers. This relationship is used, together with the ferrite core probe model to predict probe impedances for a simple ferrite core probe above a multi-layered conductor. For multi-frequency modeling

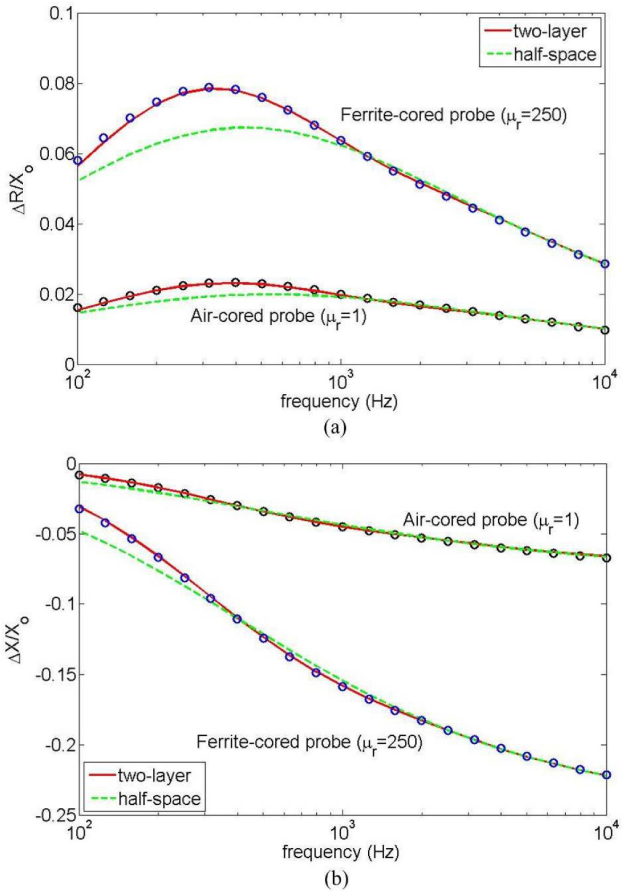

Figure 4.12 Normalized impedance change as a function of frequency for an air-cored coil (μ_r=1) and ferrite-cored coil (μ_r=250) due to the brass C2600 plate. Circles are experiment data, solid lines are theory results of the two-layer model and dash lines of half-space model.

only the reflection matrix, $\mathbf{\Gamma}$, changes with frequency and therefore the calculations can be done efficiently. Furthermore, this approach can be extended to other axisymmetric ferrite core shapes (19), such as U-shape and E-shape. It is also possible to extend this approach to 3D problems in Cartesian coordinates using a double truncated series.

4.9 Acknowledgments

This work was supported by the NSF Industry/University Cooperative Research program at Iowa State University's Center for Nondestructive Evaluation.

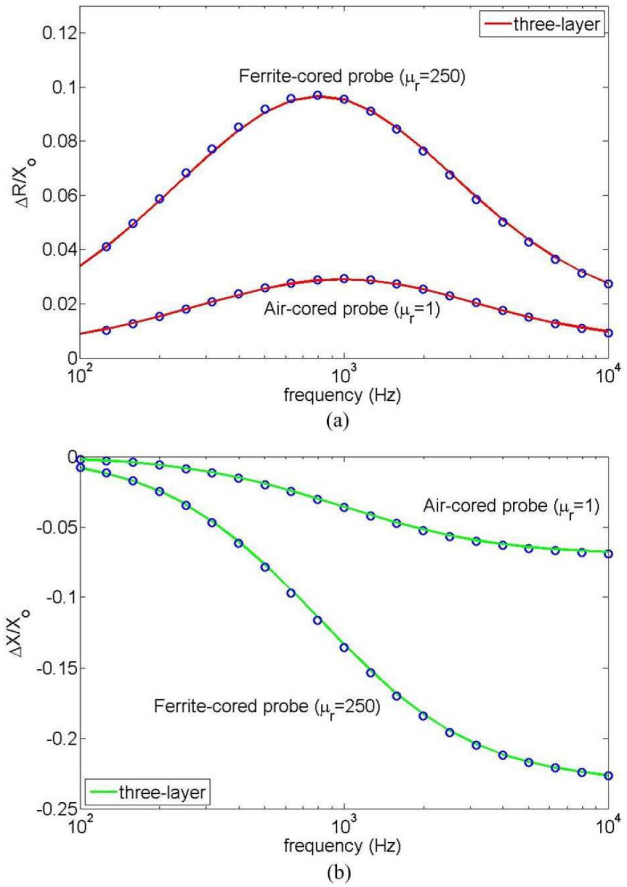

Figure 4.13 Normalized impedance change as a function of frequency for an air-cored coil (μ_r=1) and ferrite-cored coil (μ_r=250) due to the plates (Al on Ti). Circles are experiment data and solid lines are the three-layer theoretical predictions.

4.10 Appendix

4.10.1 Matrix Definitions

In the matrices evaluated here, the κ_i are the roots of $J_1(\kappa_i b) = 0$ and the q_j are roots of $F_1(q_j b) = 0$ where $F_1(\mathbf{q}b)$ is given by (4.13)-(4.15).

$$\begin{aligned} \mathbf{C} &= [c_{ij}] \\ c_{ij} &= \int_0^b J_0(\kappa_i\rho) J_0(\kappa_j\rho)\,\rho d\rho = \int_0^b J_1(\kappa_i\rho) J_1(\kappa_j\rho)\,\rho d\rho \\ &= \begin{cases} 0 & i \neq j \\ \frac{b^2}{2} J_0^2(\kappa_j b) & i = j. \end{cases} \end{aligned} \tag{4.62}$$

Using Ψ_1 given by (4.12)-(4.15), we define

$$\begin{aligned}
\mathbf{D} &= [d_{ij}] \\
d_{ij} &= \frac{1}{\mu_r}\int_0^a \Psi_1(q_i\rho)\,\Psi_1(q_j\rho)\,\rho d\rho + \int_a^b \Psi_1(q_i\rho)\,\Psi_1(q_j\rho)\,\rho d\rho \\
&= \mu_r\int_0^a J_1(q_i\rho)\,J_1(q_j\rho)\,\rho d\rho + \int_a^b F_1(q_i\rho)\,F_1(q_j\rho)\,\rho d\rho \\
&= \begin{cases} 0 & i \neq j \\ \frac{b^2}{2}F_0^2(q_jb) + \frac{a^2(\mu_r-1)}{2}\left[J_0^2(q_ja) - \mu_r J_1^2(q_ja)\right] & i = j. \end{cases}
\end{aligned} \tag{4.63}$$

Similarly we define

$$\begin{aligned}
\mathbf{U} &= [u_{ij}] \\
u_{ij} &= \frac{1}{\mu_r}\int_0^a J_1(\kappa_i\rho)\,\Psi_1(q_j\rho)\,\rho d\rho + \int_a^b J_1(\kappa_i\rho)\,\Psi_1(q_j\rho)\,\rho d\rho \\
&= \int_0^a J_1(\kappa_i\rho)\,J_1(q_j\rho)\,\rho d\rho + \int_a^b J_1(\kappa_i\rho)\,F_1(q_j\rho)\,\rho d\rho \\
&= \begin{cases} \frac{a}{\kappa_i^2-q_j^2}\kappa_i J_0(\kappa_ia)\,J_1(q_ja)\,(\mu_r-1) & \kappa_i \neq q_j \\ \frac{b^2}{2}J_0(q_jb)\,F_0(q_jb) - \frac{a^2}{2}J_1^2(q_ja)\,(\mu_r-1) & \\ \quad + \frac{aJ_0(q_ja)J_1(q_ja)}{2q_j}\,(\mu_r-1) & \kappa_i = q_j. \end{cases}
\end{aligned} \tag{4.64}$$

Using Ψ_0 given by (4.12)-(4.15), we define

$$\begin{aligned}
\mathbf{V} &= [v_{ij}] \\
v_{ij} &= \int_0^b J_0(\kappa_i\rho)\,\Psi_0(q_j\rho)\,\rho d\rho \\
&= \mu_r\int_0^a J_0(\kappa_i\rho)\,J_0(q_j\rho)\,\rho d\rho + \int_a^b J_0(\kappa_i\rho)\,F_0(q_j\rho)\,\rho d\rho \\
&= \begin{cases} \frac{a}{\kappa_i^2-q_j^2}\kappa_i J_1(\kappa_ia)\,J_0(q_ja)\,(\mu_r-1), & \kappa_i \neq q_j \\ \frac{b^2}{2}J_0(q_jb)\,F_0(q_jb) + \frac{a^2}{2}J_0^2(q_ja)\,(\mu_r-1) & \kappa_i = q_j. \end{cases}
\end{aligned} \tag{4.65}$$

4.10.2 Reflection Coefficient for a Piecewise Uniform Layered Conductor

For a multi-layered conductor as shown in Figure 4.1, the expression for the ferrite-cored coil impedance is the same as equation (4.59) where $\mathbf{\Gamma}$ is now considered to be the corresponding reflection coefficients for a piecewise uniform layered conductor including a possibly nonconducting layer. The reflection coefficient, $\mathbf{\Gamma}$, is then defined with respect to the surface of the

conductor at $z = -d_1$, includes the effects of multiple interfaces and is given by,

$$\boldsymbol{\Gamma} = e^{-2\boldsymbol{\kappa} d_1}[(\boldsymbol{\kappa}+\boldsymbol{\gamma}_1)+\boldsymbol{\Gamma}_1(\boldsymbol{\kappa}-\boldsymbol{\gamma}_1)]^{-1}[(\boldsymbol{\kappa}-\boldsymbol{\gamma}_1)+\boldsymbol{\Gamma}_1(\boldsymbol{\kappa}+\boldsymbol{\gamma}_1)], \tag{4.66}$$

where $\boldsymbol{\Gamma}_1$ is the reflection coefficient defined with respect to the interface at $z = -d_2$. In general for a n-layer conductor, one finds, using an approach similar to one given previously (18), that

$$\boldsymbol{\Gamma}_i = e^{-2\boldsymbol{\gamma}_i(d_{i+1}-d_i)}[(\boldsymbol{\gamma}_i+\boldsymbol{\gamma}_{i+1})+\boldsymbol{\Gamma}_{i+1}(\boldsymbol{\gamma}_i-\boldsymbol{\gamma}_{i+1})]^{-1}[(\boldsymbol{\gamma}_i-\boldsymbol{\gamma}_{i+1})+\boldsymbol{\Gamma}_{i+1}(\boldsymbol{\gamma}_i+\boldsymbol{\gamma}_{i+1})], \quad i = 1, 2, ..., n-2 \tag{4.67}$$

and

$$\boldsymbol{\Gamma}_{n-1} = e^{-2\boldsymbol{\gamma}_{n-1}(d_n-d_{n-1})}(\boldsymbol{\gamma}_{n-1}+\boldsymbol{\gamma}_n)^{-1}(\boldsymbol{\gamma}_{n-1}-\boldsymbol{\gamma}_n), \tag{4.68}$$

where $\boldsymbol{\gamma}_m = [\gamma_{mij}]$, $\gamma_{mij} = \sqrt{\kappa_{ij}^2 + \jmath\omega\mu_0\mu_{rm}\sigma_m}\delta_{ij}/\mu_{rm}$, $m = 1, 2, ..., n$ and $\boldsymbol{\Gamma}_i$ is the reflection coefficient defined at the interface $z = -d_{i+1}$. In the case of a uniform half-space, for example, $d_2 \to \infty$, $\boldsymbol{\Gamma_1} \to 0$, and equation (4.66) reduces to equation (4.29).

4.11 References

[1] Moulder J C, Uzal E and Rose J H 1992 Thickness and conductivity of metallic layers from eddy current measurements *Rev. Sci. Instrum.* **63** 3455–65

[2] May P, Zhou E and Morton D 2007 The design of a ferrite-cored probe *Sens. Actuators, A* **136** 221–8

[3] Sollier T, Buvat F, Pichenot G and Premel D 2004 Eddy current modeling of ferrite-core probes, application to the simulation of eddy current signals from surface breaking flaws in austenitic steel *Proceedings of the 16th World Conference on NDT, Montreal*

[4] Norton S J, Kahn A H and Mester M L 1989 Reconstructing electrical conductivity profiles from variable-frequency eddy current measurements *Res. Nondestruct. Eval.* **1** 167–79

[5] Nair S M and Rose J H 1990 Reconstruction of three-dimensional conductivity variations from eddy current (electromagnetic induction) data *Inverse Probl.* **6** 1007–30

[6] Rose J H and Nair S M 1991 Exact recovery of the DC electrical conductivity of a layered solid *Inverse Probl.* **7** L31–6

[7] Dodd C V and Deeds W E 1968 Analytical solutions to eddy-current probe-coil problems *J. Appl. Phys.* **39** 2829–38

[8] Sabbagh H A1987 A model of eddy-current probes with ferrite cores *IEEE Trans. Magn.* **23** 1888–904

[9] Buvat F, Pichenot G, Lesselier D, Lambert M and Voillaume H 2004 A fast model of eddy current ferrite-cored probes for NDE *Electromagnetic Nondestructive Evaluation* **24** 44–51

[10] Hannakam L and Albach M 1981 *Arch. Elektrotech.* **64** 127–34

[11] Timmerberg J 1983 *Arch. Elektrotech.* **66** 289–93

[12] Nethe A 1991 *Arch. Elektrotech.* **74** 389–401

[13] Theodoulidis T P 2003 Model of ferrite-cored probes for eddy current nondestructive evaluation *J. Appl. Phys.* **93** 3071–8

[14] Watson G N 1922 *A Treatise on the Theory of Bessel Functions* (Cambridge: Cambridge University Press)

[15] Abramowitz M and Stegun I A 1970 *Handbook of Mathematical Functions with Formulas, Graphs, and Mathematical Tables* (New York: Dover)

[16] Gradshteyn I S and Ryzhik I M 1980 *Tables of Integrals, Series, and Products* (New York: Academic)

[17] Rektorys K 1977 *Variational Methods in Mathematics, Science, and Engineering* (Boston: D. Reidel)

[18] Luquire J W, Deeds W E and Dodd C V 1970 Alternating current distribution between planar conductors *J. Appl. Phys.* **41** 3983–91

[19] Bayani H, Theodoulidis T P and Sasada I 2007 Application of eigenfunction expansions to eddy current NDE: a model of cup-cored probes *Electromagnetic Nondestructive Evaluation* **28** 57–64

CHAPTER 5. BOBBIN COIL IMPEDANCE CHANGE DUE TO A TUBE SUPPORT PLATE

A paper to be submitted to *The IEEE Transactions on Magnetics*

Yi Lu and John R. Bowler

5.1 Abstract

We have evaluated the signal variation of a differential bobbin coil due to a tube support plate by using a simple semi-analytical method. To find the coil response, the electromagnetic field is determined for a bobbin coil coaxial with a flawless tube passing through a coaxial circular hole in a plate. The field in this axially symmetric configuration has been found analytically by introducing truncation boundaries at planes perpendicular to the axis of the system, remote from the probe and support plate. This means that tangential electric field on the planes can be set to zero without significantly affecting the field in the support plate region. By restricting the problem domain using a truncation boundaries, the solution is expressed as Fourier series for different region of the limited domain, rather than as Fourier transforms. The series coefficients are determine using the continuity properties of the electromagnetic field. This process yields the expansion coefficients expressed in terms of corresponding coefficients of an expansion for the source coil in free space. From the solution, the coil signal due to the support plate is found. The accuracy of the calculation is easily controlled by adjusting the distance between the truncation planes and/or the number of terms in the series expansions. An extension of this analysis will provide an efficient means of computing signals due to tube cracks in the support plate region.

5.2 Introduction

The problem of calculating eddy current probe signals of bobbin coils used for tube inspection has been studied extensively to simulate the testing heat exchangers (1). This is motivated by the use of numerical simulations to improve inspections and to aid in the interpretation of test data. Calculations can be time consuming if the numerical formulation leads to a large number of unknowns but the computational cost can be greatly reduced by using semi-analytical methods. In particular, calculations of the response due to a flaw in a tube can be carried out efficiently using integral methods because one can derive an integral kernel for an infinite tube problem. This means that the kernel embodies the interface conditions at the surface of the tube. Therefore an integral expression for the tube field can be constructed which takes account of these conditions automatically. The problem is usually reduced from one of solving an integral equation to one of computing the solution of a matrix equation by applying the method of moments. In this scheme, the only unknowns in the problem are those which represent the field in the region of an inhomogeneity in the tube wall. The inhomogeneity can, for example, be a crack, which can often be adequately represented using just few hundred volume elements. In which case the flaw signal can be determined accurately, efficiently, and quickly.

If there is a tube support plate present, this must be taken into account. It produces probe signals that are usually larger than those due to cracks and can mask the flaw signals. Accounting for the support plate can be done by rendering it in a discrete form but the computation cost would then escalate. In order to retain the efficiency of the uniform tube calculations, we have sought a better approach in which the effect of the tube support plate is included in the kernel of the integral formulation of the flaw problem. This has been done for a simple case in which the plate has a circle hole in it through which is a coaxial tube. Potentially, the computational burden of doing this is not negligible because the kernel would be more complicated, but the number of unknowns remains unchanged and this is usually a critical cost-dependent parameter. In order to reach the point at which the new kernel can be used, we consider here a preliminary problem in which the probe signal due to the support plate is calculated analyt-

ically. There are two principle versions of the basic support plate problem depending on the probe. The first and simpler one, which will be considered here, involves a bobbin coil coaxial with the tube. In the more complicated case, one considers a rotary pancake coil, defined as one having its axis perpendicular to that of the tube.

The first basic support plate problem is axially symmetric and could be solved numerically with moderate computational cost. However, because we need a solution that can evolve into one that can be used to compute a support plate kernel and thereby give us low cost method of getting flaw signals, we used analytical methods as much as possible. Without the support plate, the bobbin coil field is given by analytical expressions given by Dodd and Deeds (2). These solutions are derived using separation of variables in which the axial dependence is expressed in terms of a Fourier transform and the radial dependence using associated Bessel functions. In the presence of the support plate, the problem is more complicated because the probe field must satisfy field continuity conditions at the surface of the support plate. In order to deal with these extra constraints we truncate the problem domain by introducing an artificial boundary at an axial plane some remote distance for the probe and plate. On this boundary, the field is set to zero. At the axial plane bisecting the support plate we impose a symmetry condition. This allows us to express the general solution as a combination of odd and ever solutions with respect to the $z-$axis whose origin is at the mid-plane of the support plate. The effect of the truncation boundary is to change the z-dependence to one represented by a Fourier series rather than a Fourier transform. In this way the problem reduces to one of computing the coefficient of a series. In effect, the introduction of a boundary has made the problem discrete which means that we can determine coefficients of the series by solving a matrix equation derived using eigenfunctions that will allow us to satisfy the continuity conditions at the surface of the support plate.

The general approach is referred to as the truncated region eigenfunction expansion (TREE) method. By introducing an artificial boundary we have a means of getting an analytical solution to a problem that might be intractable or at least more difficult by other means. The new boundary modifies the problem but because it is remote from the source of the field in a place where the field would otherwise be close to zero anyway, it need not have a significant

effect on the field strength in the source region. In using the TREE method for quasi-static problems(3; 4; 5) we have established a useful guiding principle. This states that if an analytical solution can be found for a source in air near a conductor then you should also be able to find an analytical solution for a dipole source in the conductor by using the same approach. In eddy current problems this implies that if coil field can be found in an analytical form for a given flawless configuration, then you should also be able to find an analytical expression for the Green's kernel representing a singular source in the conductor. That kernel is then available to get a numerical solution to an integral equation using the moment method and thereby determine the effect of a flaw in the conductor.

In this article we make a start on support plate related problems by finding an analytical solution for a bobbin coil in a tube in the presence of a support plate. This will form a base for future work in which we seek the kernel which embodies the boundary conditions on a tube and a support plate and use it in an efficient calculation of the probe response to cracks in a tube in the support plate region.

5.3 Formulation

We consider a differential bobbin coil in a tube passing through a coaxial circular hole in an infinite support plate, Figure 5.1. Both the tube and the support plate are assumed to be homogeneous having linear material properties which are not necessarily the same. The differential probe signal is to be determined as a function of probe position by considering solutions that have odd or even symmetry about a plane $z = 0$ that divides the problem region and the support itself at the mid-plane. Taking the average of the two solutions gives the one required. Because the probe is differential, we can either consider coils with the same current and subtract the voltage signals, or coils with opposite currents and add the voltage signals. Here we follow the second option.

The tube has inner radius b_1 and outer radius b_2. The thickness of the support plate is $2c$ and b_3 is the radius of the hole in the support plate. One can let this radius be the same as b_2 but in general they will be different. It is assumed that the tube has the permeability $\mu_0\mu_{r1}$ and has a uniform conductivity σ_1. Whereas the support plate has a conductivity σ_2 and a permeability

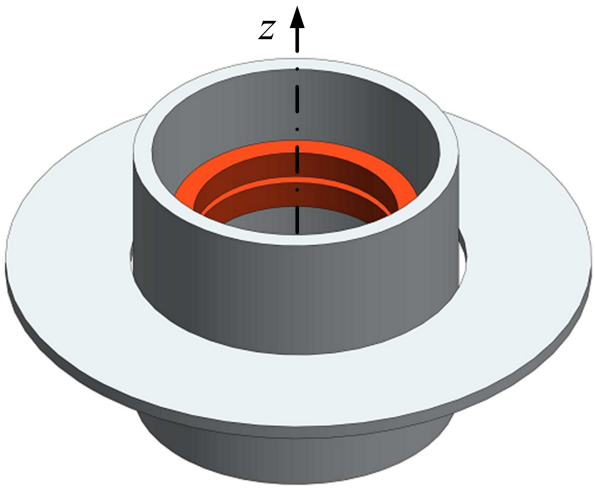

Figure 5.1 Perspective view of a differential bobbin coil in a tube with a support plate.

$\mu_0\mu_{r2}$. Axial symmetry implies that we can determine the quasi-static electromagnetic field using the azimuthal component of the magnetic vector potential (MVP). For a nonconductive region, the MVP satisfies the Laplace equation and for a conductive region, the Helmholtz equation,

$$(\nabla^2 - k_m^2)A = 0, \tag{5.1}$$

where $k_m^2 = \jmath\omega\mu_0\mu_{rm}\sigma_m$ with $m = 1$ for the tube region and $m = 2$ for the plate. We determine the azimuthal MVP for the half the problem domain ($z \geq 0$) assuming, in turn, odd and even symmetry about a plane $z = 0$ bisecting the support plate. For the odd symmetry solution, we impose Dirichlet conditions on the MVP at the dividing plane $z = 0$ and at the truncation boundary, $z = h$. Thus, these two surfaces represent magnetic insulation boundaries. For the even symmetry solution we impose a Dirichlet condition (magnetic insulation boundary) at $z = h$ and a Neumann condition at $z = 0$ (electric insulation boundary).

5.3.1 Odd Solution Analysis

Referring to Figure 5.2, we identify 4 regions separated by cylindrical boundaries and express the magnetic vector potential in these regions in terms of series expansions. Region 1 is defined as the cylindrical zone between the coil and the inner surface of the tube, such that $r_2 \leq \rho \leq b_1$ where r_2 is the outer radius of the coil. In this region, the field, and thus the MVP, is the sum

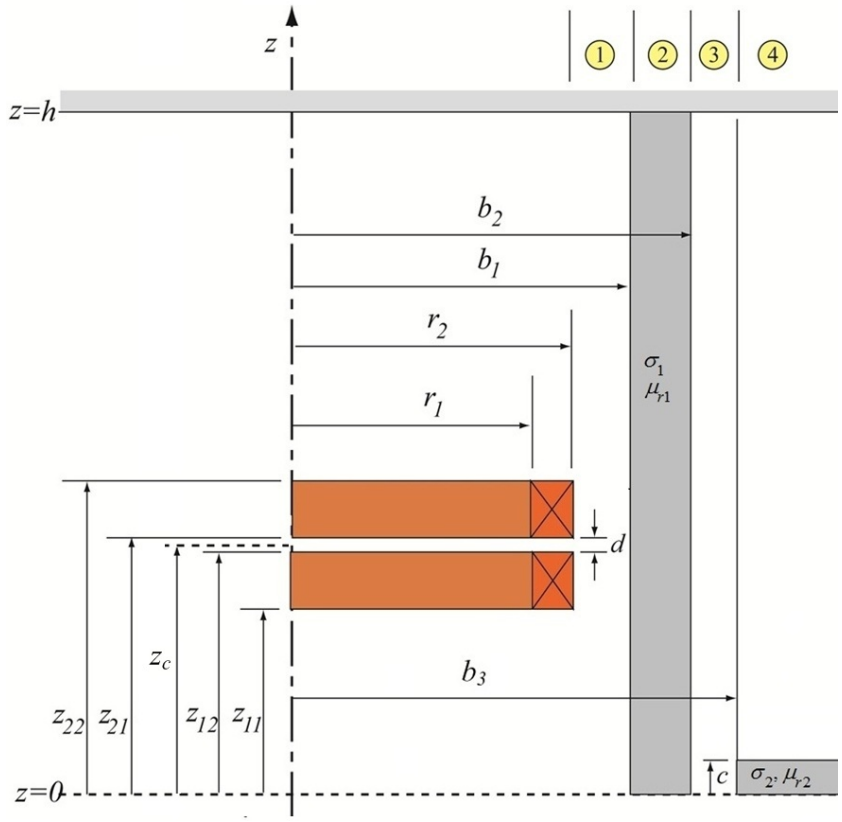

Figure 5.2 Differential bobbin coil in a tube with a support plate. The axis of the tube is shown on the left as line formed with long and short dashes. The dashed horizontal line at the bottom of the diagram, indicate the mid-plane symmetry boundary about which the solution can be odd or even. The symmetry plane bisects the support plate. At the top of the diagram we have shown the truncation boundary.

of a term representing the field due to the source coil in free space plus the reaction field due to eddy currents induced in the tube and support plate. Corresponding expansion coefficients for these terms are written D_i and $C_i^{(1)}$ respectively. Later we will specify source coefficients D_i.

Region 2 is the tube region and region 3 is non-conductive including a small annular gap of width $b_3 - b_2$ between the tube and support plate. Region 4 consists of a non-conductive region where $c < z \leq h$ and a conductive region of the support plate where $0 \leq z \leq c$.

The magnetic vector potentials in the regions 1 through 3 for the odd parity solution have

the forms

$$A_1(\rho,z)=\sum_{i=1}^{\infty}\sin(u_iz)\left[I_1(u_i\rho)C_i^{(1)}+K_1(u_i\rho)D_i\right] \tag{5.2}$$

$$A_2\left(\rho,z\right)=\sum_{i=1}^{\infty}\sin\left(u_iz\right)\left[I_1\left(\gamma_i\rho\right)C_i^{(2)}+K_1\left(\gamma_i\rho\right)D_i^{(2)}\right] \tag{5.3}$$

and

$$A_3\left(\rho,z\right)=\sum_{i=1}^{\infty}\sin\left(u_iz\right)\left[I_1\left(u_i\rho\right)C_i^{(3)}+K_1\left(u_i\rho\right)D_i^{(3)}\right] \tag{5.4}$$

where $u_i=\frac{i\pi}{h}$, $\gamma_i^2=u_i^2+k_1^2$.

For region 4 we ensure the continuity of E_ϕ and the MVP at $z=c$ by writing

$$A_4\left(\rho,z\right)=\sum_{i=1}^{\infty}\begin{bmatrix}\sin(q_iz)\,/\,\sin(q_ic)\\ \sin[p_i\left(h-z\right)]\,/\,\sin[p_i\left(h-c\right)]\end{bmatrix}K_1\left(p_i\rho\right)D_i^{(4)}\quad\begin{matrix}0\le z\le c\\ c<z\le h\end{matrix} \tag{5.5}$$

where $p_i^2=q_i^2+k_2^2$. The eigenvalues of q_i and p_i can be numerically derived from (6)

$$q_i\cos(q_ic)\sin[p_i(h-c)]+\mu_{r2}p_i\sin(q_ic)\cos[p_i(h-c)]=0, \tag{5.6}$$

which is deduced from the continuity of H_ρ at the upper surface of the support plate.

From the continuity of E_ϕ and H_z at $\rho=b_3$, we find that

$$A_3(b_3,z)=A_4(b_3,z) \tag{5.7}$$

and

$$\begin{bmatrix}1\\1\end{bmatrix}\frac{1}{\rho}\frac{\partial\left(\rho A_3\right)}{\partial\rho}\bigg|_{\rho=b_3}=\begin{bmatrix}\frac{1}{\mu_{r2}}\\1\end{bmatrix}\frac{1}{\rho}\frac{\partial\left(\rho A_4\right)}{\partial\rho}\bigg|_{\rho=b_3}\quad\begin{matrix}0\le z<c\\ c\le z\le h.\end{matrix} \tag{5.8}$$

We ensure that the continuity of E_ϕ and H_z are satisfied in the weak sense (7) by taking moments as follow. Substituting (5.4) and (5.5) into (5.7)-(5.8), multiplying $\sin\left(u_iz\right)$ and integrating from 0 to h gives

$$I_1\left(\mathbf{u}b_3\right)\mathbf{C}^{(3)}+K_1\left(\mathbf{u}b_3\right)\mathbf{D}^{(3)}=\mathbf{U}K_1\left(\mathbf{p}b_3\right)\mathbf{D}^{(4)} \tag{5.9}$$

and

$$\mathbf{u}\left[I_0\left(\mathbf{u}b_3\right)\mathbf{C}^{(3)}-K_0\left(\mathbf{u}b_3\right)\mathbf{D}^{(3)}\right]=-\mathbf{V}\mathbf{p}K_0\left(\mathbf{p}b_3\right)\mathbf{D}^{(4)} \tag{5.10}$$

where $\mathbf{u}$, $\mathbf{p}$ and Bessel functions with bold symbol arguments represent diagonal matrices, $\mathbf{C}^{(3)}$ and $\mathbf{D}^{(3-4)}$ are column vectors while $\mathbf{U}$ and $\mathbf{V}$ are matrices whose elements are

$$\begin{aligned} U_{ij} &= \frac{2}{h}\left\{\frac{1}{\sin(q_j c)}\int_0^c \sin(u_i z)\sin(q_j z)\,dz \right. \\ &\left. + \frac{1}{\sin[p_j(h-c)]}\int_c^h \sin(u_i z)\sin[p_j(h-z)]\,dz\right\} \end{aligned} \tag{5.11}$$

and

$$\begin{aligned} V_{ij} &= \frac{2}{h}\left\{\frac{1}{\mu_{r2}\sin(q_j c)}\int_0^c \sin(u_i z)\sin(q_j z)\,dz \right. \\ &\left. + \frac{1}{\sin[p_j(h-c)]}\int_c^h \sin(u_i z)\sin[p_j(h-z)]\,dz\right\}. \end{aligned} \tag{5.12}$$

Equations (5.9) and (5.10) are found by applying the trigonometric orthogonality relation

$$\int_0^h \sin(u_i z)\sin(u_j z)\,dz = \frac{h}{2}\delta_{ij}, \tag{5.13}$$

where, δ_{ij} is the Kronecker delta.

Similarly, using the continuity of E_ϕ and H_ρ at $\rho = b_2$, one gets

$$I_1(\boldsymbol{\gamma} b_2)\,\mathbf{C}^{(2)} + K_1(\boldsymbol{\gamma} b_2)\,\mathbf{D}^{(2)} = I_1(\mathbf{u} b_2)\,\mathbf{C}^{(3)} + K_1(\mathbf{u} b_2)\,\mathbf{D}^{(3)} \tag{5.14}$$

and

$$\boldsymbol{\gamma}\left[I_0(\boldsymbol{\gamma} b_2)\,\mathbf{C}^{(2)} - K_0(\boldsymbol{\gamma} b_2)\,\mathbf{D}^{(2)}\right] = \mu_{r1}\mathbf{u}\left[I_0(\mathbf{u} b_2)\,\mathbf{C}^{(3)} - K_0(\mathbf{u} b_2)\,\mathbf{D}^{(3)}\right]. \tag{5.15}$$

Continuity at $\rho = b_1$, means that

$$I_1(\mathbf{u} b_1)\,\mathbf{C}^{(1)} + K_1(\mathbf{u} b_1)\,\mathbf{D} = I_1(\boldsymbol{\gamma} b_1)\,\mathbf{C}^{(2)} + K_1(\boldsymbol{\gamma} b_1)\,\mathbf{D}^{(2)} \tag{5.16}$$

and

$$\mu_{r1}\mathbf{u}\left[I_0(\mathbf{u} b_1)\,\mathbf{C}^{(1)} - K_0(\mathbf{u} b_1)\,\mathbf{D}\right] = \boldsymbol{\gamma}\left[I_0(\boldsymbol{\gamma} b_1)\,\mathbf{C}^{(2)} - K_0(\boldsymbol{\gamma} b_1)\,\mathbf{D}^{(2)}\right]. \tag{5.17}$$

Here, $\boldsymbol{\gamma}$ is a diagonal matrix. $\mathbf{C}^{(1-2)}$, $\mathbf{D}$ and $\mathbf{D}^{(2)}$ represent column vectors.

By applying matrix and vector manipulations to the equations (5.9)-(5.10) and (5.14)-(5.17), the six unknown coefficient vectors $\mathbf{C}^{(1-3)}$ and $\mathbf{D}^{(2-4)}$ can be expressed in term of the presented source vector $\mathbf{D}$. The expansion coefficients are then given by

$$\mathbf{C}^{(1)} = \mathbf{W}\mathbf{D} = \mathbf{W}_a\mathbf{W}_b^{-1}\mathbf{D} \tag{5.18}$$

$$\mathbf{C}^{(2)} = \frac{1}{b_1}\mathbf{C}_{24}\mathbf{W}_b^{-1}\mathbf{D} \tag{5.19}$$

$$\mathbf{C}^{(3)} = \frac{1}{b_1 b_2}\mathbf{C}_{34}\mathbf{W}_b^{-1}\mathbf{D} \tag{5.20}$$

$$\mathbf{D}^{(2)} = \frac{1}{b_1}\mathbf{D}_{24}\mathbf{W}_b^{-1}\mathbf{D} \tag{5.21}$$

$$\mathbf{D}^{(3)} = \frac{1}{b_1 b_2}\mathbf{D}_{34}\mathbf{W}_b^{-1}\mathbf{D} \tag{5.22}$$

$$\mathbf{D}^{(4)} = \frac{1}{b_1 b_2 b_3}\mathbf{W}_b^{-1}\mathbf{D} \tag{5.23}$$

where $\mathbf{C}_{24}$, $\mathbf{C}_{34}$, $\mathbf{D}_{24}$, $\mathbf{D}_{34}$, $\mathbf{W}_a$ and $\mathbf{W}_b$ are defined as

$$\mathbf{C}_{24} = \boldsymbol{\gamma}\mathbf{K}_0\left(\boldsymbol{\gamma} b_2\right)\mathbf{T}_1 + \mathbf{K}_1\left(\boldsymbol{\gamma} b_2\right)\mathbf{T}_2 \tag{5.24}$$

$$\mathbf{C}_{34} = \mathbf{u}\mathbf{K}_0\left(\mathbf{u} b_3\right)\mathbf{U}\mathbf{K}_1\left(\mathbf{p} b_3\right) - \mathbf{K}_1\left(\mathbf{u} b_3\right)\mathbf{V}\mathbf{p}\mathbf{K}_0\left(\mathbf{p} b_3\right) \tag{5.25}$$

$$\mathbf{D}_{24} = \boldsymbol{\gamma}\mathbf{I}_0\left(\boldsymbol{\gamma} b_2\right)\mathbf{T}_1 - \mathbf{I}_1\left(\boldsymbol{\gamma} b_2\right)\mathbf{T}_2 \tag{5.26}$$

$$\mathbf{D}_{34} = \mathbf{u}\mathbf{I}_0\left(\mathbf{u} b_3\right)\mathbf{U}\mathbf{K}_1\left(\mathbf{p} b_3\right) + \mathbf{I}_1\left(\mathbf{u} b_3\right)\mathbf{V}\mathbf{p}\mathbf{K}_0\left(\mathbf{p} b_3\right) \tag{5.27}$$

$$\mathbf{W}_a = \mathbf{u}\mathbf{K}_0\left(\mathbf{u} b_1\right)\mathbf{W}_1 + \mathbf{K}_1\left(\mathbf{u} b_1\right)\mathbf{W}_2 \tag{5.28}$$

$$\mathbf{W}_b = \mathbf{u}\mathbf{I}_0\left(\mathbf{u} b_1\right)\mathbf{W}_1 - \mathbf{I}_1\left(\mathbf{u} b_1\right)\mathbf{W}_2 \tag{5.29}$$

with

$$\mathbf{T}_1 = \mathbf{I}_1\left(\mathbf{u} b_2\right)\mathbf{C}_{34} + \mathbf{K}_1\left(\mathbf{u} b_2\right)\mathbf{D}_{34} \tag{5.30}$$

$$\mathbf{T}_2 = \mu_{r1}\mathbf{u}\left[\mathbf{I}_0\left(\mathbf{u} b_2\right)\mathbf{C}_{34} - \mathbf{K}_0\left(\mathbf{u} b_2\right)\mathbf{D}_{34}\right] \tag{5.31}$$

$$\mathbf{W}_1 = \mathbf{I}_1\left(\boldsymbol{\gamma} b_1\right)\mathbf{C}_{24} + \mathbf{K}_1\left(\boldsymbol{\gamma} b_1\right)\mathbf{D}_{24} \tag{5.32}$$

$$\mathbf{W}_2 = \frac{1}{\mu_{r1}}\boldsymbol{\gamma}\left[\mathbf{I}_0\left(\boldsymbol{\gamma} b_1\right)\mathbf{C}_{24} - \mathbf{K}_0\left(\boldsymbol{\gamma} b_1\right)\mathbf{D}_{24}\right]. \tag{5.33}$$

Thus, the eddy current density in the tube can be written as

$$J_2\left(\rho, z\right) = -\jmath\omega\sigma_1 A_2\left(\rho, z\right) \tag{5.34}$$

with (5.3), (5.19) and (5.21).

5.3.2 Even Solution Analysis

Following the similar procedure, for the even parity, the azimuthal components of the MVP in each region can be expressed as below:

$$A_1(\rho,z)=\sum_{i=1}^{\infty}\cos(u_i z)\left[I_1(u_i\rho)\,C_i^{(1)}+K_1(u_i\rho)\,D_i\right] \tag{5.35}$$

$$A_2(\rho,z)=\sum_{i=1}^{\infty}\cos(u_i z)\left[I_1(\gamma_i\rho)\,C_i^{(2)}+K_1(\gamma_i\rho)\,D_i^{(2)}\right] \tag{5.36}$$

$$A_3(\rho,z)=\sum_{i=1}^{\infty}\cos(u_i z)\left[I_1(u_i\rho)\,C_i^{(3)}+K_1(u_i\rho)\,D_i^{(3)}\right] \tag{5.37}$$

and

$$A_4(\rho,z)=\sum_{i=1}^{\infty}\begin{bmatrix}\cos(q_i z)\,/\,\cos(q_i c) & 0\le z\le c\\ \sin[p_i(h-z)]\,/\,\sin[p_i(h-c)] & c<z\le h\end{bmatrix}K_1(p_i\rho)\,D_i^{(4)} \tag{5.38}$$

where $u_i=\frac{(2i-1)\pi}{2h}$, $\gamma_i^2=u_i^2+k_1^2$, and $p_i^2=q_i^2+k_2^2$. Similarly, the values of q_i and p_i can be derived numerically from

$$q_i\sin(q_i c)\sin[p_i(h-c)]-\mu_{r2}p_i\cos(q_i c)\cos[p_i(h-c)]=0. \tag{5.39}$$

As for odd parity case, using the continuity conditions that apply to the field at the cylindrical interfaces, one gets the same final expressions with modified source coefficients D_i, matrices $\mathbf{U}$ and $\mathbf{V}$ with their elements, given by

$$\begin{aligned}U_{ij} &= \frac{2}{h}\left\{\frac{1}{\cos(q_j c)}\int_0^c\cos(u_i z)\cos(q_j z)\,dz\right.\\ &\quad\left.+\frac{1}{\sin[p_j(h-c)]}\int_c^h\cos(u_i z)\sin[p_j(h-z)]\,dz\right\}\end{aligned} \tag{5.40}$$

and

$$\begin{aligned}V_{ij} &= \frac{2}{h}\left\{\frac{1}{\mu_{r2}\cos(q_j c)}\int_0^c\cos(u_i z)\cos(q_j z)\,dz\right.\\ &\quad\left.+\frac{1}{\sin[p_j(h-c)]}\int_c^h\cos(u_i z)\sin[p_j(h-z)]\,dz\right\}\end{aligned} \tag{5.41}$$

using the orthogonality property

$$\int_0^h\cos(u_i z)\cos(u_j z)\,dz=\frac{h}{2}\delta_{ij}. \tag{5.42}$$

5.3.3 Source Coefficients

The coefficients D_i describe the field due to the isolated source coil and have been studied for both odd and even configurations (6; 8). For theses two cases, in a truncated non-conductive region, the magnetic vector potential outside the coil has the form

$$A_0^{\text{odd}}(\rho, z) = \sum_{i=1}^{\infty} \sin(u_i z) K_1(u_i \rho) D_i^{\text{odd}} \tag{5.43}$$

and

$$A_0^{\text{even}}(\rho, z) = \sum_{i=1}^{\infty} \cos(u_i z) K_1(u_i \rho) D_i^{\text{even}} \tag{5.44}$$

where

$$D_i^{\text{odd}} = \frac{2\mu_0 \nu I}{h u_i^3} \left[\cos(u_i z_{l2}) - \cos(u_i z_{l1})\right] \chi(u_i r_1, u_i r_2) \tag{5.45}$$

and

$$D_i^{\text{even}} = \frac{2\mu_0 \nu I}{h u_i^3} \left[\sin(u_i z_{l1}) - \sin(u_i z_{l2})\right] \chi(u_i r_1, u_i r_2) \tag{5.46}$$

with ν denoting the wire-turns density of either coil:

$$\nu = \frac{N}{(r_2 - r_1)(z_{\ell 2} - z_{\ell 1})} \qquad \ell = 1, 2 \tag{5.47}$$

and

$$\chi(x_1, x_2) = \int_{x_1}^{x_2} x I_1(x)\, dx. \tag{5.48}$$

5.3.4 Impedance

The impedance change of a coil due to the presence of the tube and support plate is (5)

$$I^2 \Delta Z = \frac{2\pi \jmath \omega}{\mu_0} \int_0^h \left[A_0 \frac{\partial(\rho \Delta A)}{\partial \rho} - \Delta A \frac{\partial(\rho A_0)}{\partial \rho}\right]\Big|_{\rho = b_1} dz \tag{5.49}$$

where A_0 is defined as (5.43) or (5.44) for different configurations and the magnetic vector potential change is given by

$$\Delta A^{\text{odd}}(\rho, z) = \sum_{i=1}^{\infty} \sin(u_i z) I_1(u_i \rho) C_i^{(1)} \tag{5.50}$$

or

$$\Delta A^{\text{even}}(\rho, z) = \sum_{i=1}^{\infty} \cos(u_i z) I_1(u_i \rho) C_i^{(1)}. \tag{5.51}$$

Substituting into (5.49), for both odd and even parities, the impedance change of a single source coil has the form

$$\Delta Z = \frac{\jmath\omega\pi h}{\mu_0 I^2}\mathbf{D}^T\mathbf{C}^{(1)} = \frac{\jmath\omega\pi h}{\mu_0 I^2}\mathbf{D}^T\mathbf{W}\mathbf{D} \tag{5.52}$$

where the matrices $\mathbf{D}$ and $\mathbf{W}$ are dependent on the specific symmetry (odd or even case).

For a differential bobbin coil consisting of two identical coils, the contribution of the tube is canceled and the corresponding impedance change due to the tube support plate is expressed as

$$\Delta Z = \Delta Z_2 - \Delta Z_1. \tag{5.53}$$

5.4 Results

We have compared semi-analytical results using the TREE method with results found using a two-dimensional finite-element method (FEM) package with the problem parameters given in Table 5.1. Figure 5.3 shows the impedance change as a function of the center position of the differential bobbin coil (from $z_c = 0$ mm to $z_c = 10$ mm) at different frequencies, in which, both the tube and the support plate are nonmagnetic material ($\mu_{r1} = \mu_{r2} = 1$). The above shows a good agreement between the TREE and FEM results, and we can also observe that when increasing the frequency, the amplitude of the eddy current signal also increases and the curve rotates clockwise.

Table 5.1 Parameters for the coil and test pieces.

Coil		**Tube**		**Support Plate**	
r_1	7.83 mm	b_1	9.84 mm	b_3	11.21 mm
r_2	8.50 mm	b_2	11.11 mm	$2c$	1 mm
$z_{22} - z_{21}$	2 mm	σ_1	1 MS/m	σ_2	10 MS/m
d	0.5 mm	μ_{r1}	1, 10, 15, 30, 50	μ_{r2}	1, 10, 15
N	70				

As shown in Figure 5.4, the predictions of coil impedance variations with distance from the support plate are compared with FEM at an excitation frequency of 10 kHz. In this case, only the tube is magnetic material ($\mu_{r1} > 1, \mu_{r2} = 1$). Both curves in Figure 5.4 shows excellent agreement to the results of the FEM. By comparing with the nonmagnetic tube result (at 10

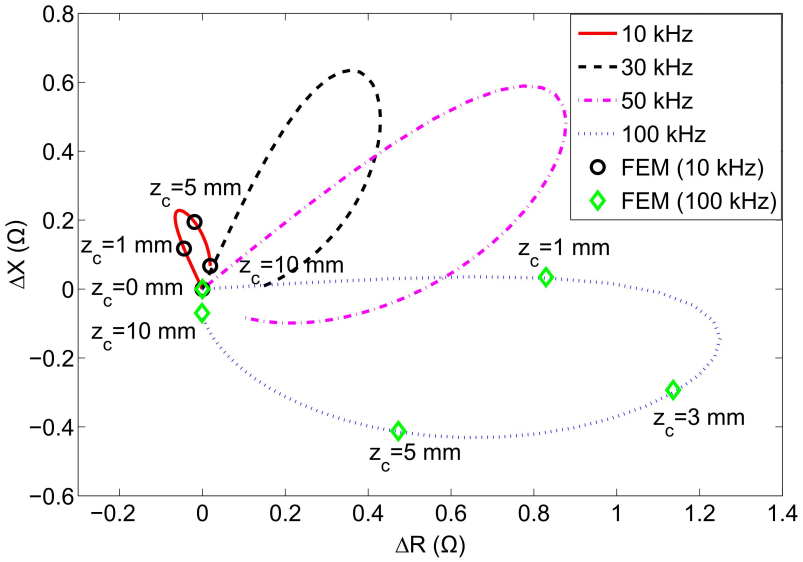

Figure 5.3 Eddy current signal variation from $z_c = 0$ mm to $z_c = 10$ mm at different frequencies compared with FEM results, in which, both the tube and the support plate are non-magnetic material ($\mu_{r1} = \mu_{r2} = 1$).

kHz) in Figure 5.3, we can observe that the signal decreases greatly with the increasement of the relative permeability of the tube.

A more complicated case is shown in Figure 5.5, in which both the tube and the support plate are magnetic materials and the relative permeabilities of the tube and the support plate can be different, though the same as in the figure. Based on the theoretical calculation and numerical computation of FEM, it is observed that the effect due to the support plate is very weak for big relative permeability or high excitation frequencies. As a result, two cases with small relative permeabilities (10 and 15) at 1kHz are analyzed, and show good agreements with FEM results.

5.5 Conclusion

A semi-analytical model of a differential bobbin coil impedance change due to a coaxial circular tube support plate has been developed. Within a truncated domain, the axial dependence of the magnetic vector potential can be represented by a Fourier series and the problem solved to account for effects the tube support plate in one in which the expansion coefficients in this

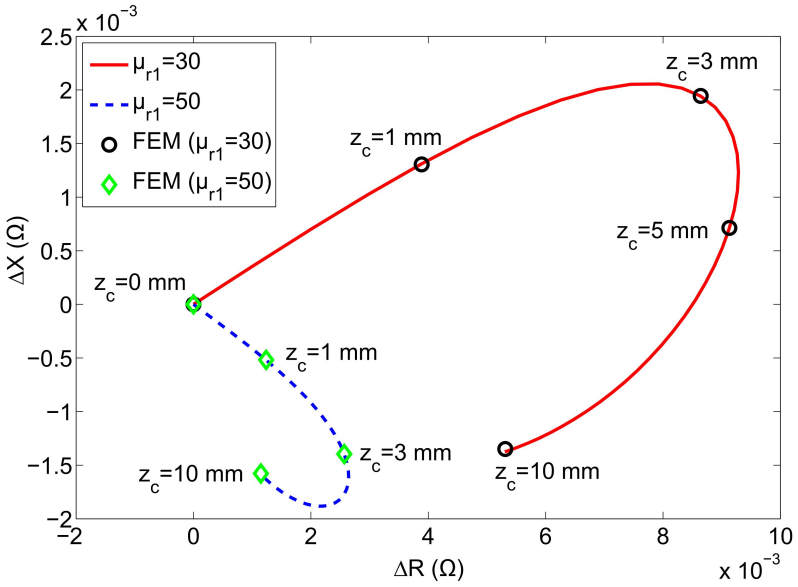

Figure 5.4 Eddy current signal variation from $z_c = 0$ mm to $z_c = 10$ mm at 10 kHz compared with FEM results, in which the tube is magnetic and the support plate is not. $(\mu_{r1} > 1, \mu_{r2} = 1)$.

series is found. The theoretical calculations show an excellent agreement with the numerical results of FEM. Besides, the close-form expression of the magnetic vector potential in a tube is critical for the more complicated 3D model for a support plate problem with a flaw or crack in the adjacent tube. The approach can be extended to deal with other similar symmetric structures, such as a circular internal or external groove in a magnetic tube.

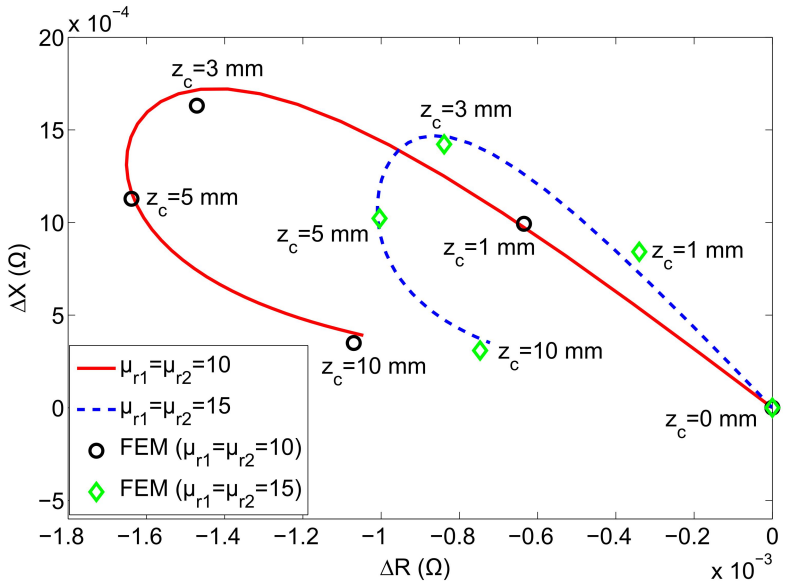

Figure 5.5 Eddy current signal variation from $z_c = 0$ mm to $z_c = 10$ mm at 1 kHz compared with FEM results. Here, both tube and support plate are magnetic material ($\mu_{r1} = \mu_{r2} > 1$).

5.6 References

[1] Cecco VS, VanDrunen G and Sharp FL 1987 *Eddy Current Testing* (Columbia: GP Courseware)

[2] Dodd CV and Deeds WE 1968 Analytical solutions to eddy current probe coil problems *J. Appl. Phys.* **39** 2829-38

[3] Theodoulidis TP 2004 End effect modeling in eddy current tube testing with bobbin coils *Int. J. Appl. Electromagn. Mech.* **19** 207-12

[4] Theodoulidis TP and Bowler JR 2005 Eddy-current interaction of a long coil with a slot in a conductive plate *IEEE Trans. Magn.* **41** 1238-47

[5] Sun H, Bowler JR and Theodoulidis TP 2005 Eddy currents induced in a finite length layered rod by a coaxial coil *IEEE Trans. Magn.* **41** 2455-61

[6] Bowler JR and Theodoulidis TP 2005 Eddy-currents induced in a conducting rod of finite length by a coaxial encircling coil *J. Phys. D: Appl. Phys.* **38** 2861-8

[7] Rektorys K 1977 *Variational Methods in Mathematics, Science, and Engineering* (Boston: D. Reidel)

[8] Theodoulidis TP and Bowler JR 2008 Impedance of an induction coil at the opening of a borehole in a conductor *J. Appl. Phys.* **103** 024905

CHAPTER 6. GENERAL CONCLUSIONS

6.1 General Discussion

For DCPD measurements, an analytical model of edge effects on metal plates with finite thickness has been established. The expression of electrical field for thinner plates represented by a Fourier series overcomes the slow convergence of the triple infinite summation generated from the method-of-images. Comparison between theory and experiments on several aluminium and spring-steel plates of various sizes shows excellent agreement. Additionally, it is shown that the uncertainty is reduced, for a given plate size, if the probe pick-up points are moved closer to the current injection points, rather than adopting the common arrangement in which the four probe points are equally spaced.

The electric field of DCPD on an uniformly layered conductive cylinders with finite length has been determined in Chapter 3 by the analytical solution expressed in terms of a Green's function. A series of four-point DCPD experiments are also designed to verify the theory solution, showing good agreements with theoretic evaluation. These analytic solutions offer a non-destructive determination of the thickness or electrical conductivity of the layered cylinder if the other parameters are given, or both parameters at the same time with more than four electrodes or by connecting electrodes in different configurations. Since this method is very sensitive to the thin tube wall thickness, it is suitably used to monitor the variation of wall thickness of pipes in power or chemical plants.

In Chapter 4, the analytical expression of the impedance and electric field of a ferrite-cored coil over a layered conductor has been developed by using the radially truncated region eigenfunction expansion (TREE) method. Starting with the field of a circular current filament in a radially truncated domain, a solution for a filament and a rectangular cross-section coil

with an infinitely long circularly cylindrical ferrite core has been constructed, then the field and impedance of a probe with finite length core are deduced. During the construction of the finite core solution, the reflection and transmission coefficient matrices that account for the core end effects are introduced and the effect of a multi-layered conductor below the probe is also taken into account. Finally, the numerical prediction for the analytical expression of probe impedance has been compared with experiments, showing an excellent agreement.

The impedance variation of a differential bobbin coil due to a tube support plate has been evaluated by using a semi-analytical method. The solution of electric field in each region can be expressed as Fourier series by applying an axial truncation boundary which satisfies the continuity conditions at the cylindrical boundaries. The theoretical predictions show very good agreement with the numerical results of finite element method (FEM). This will form a base for the future research in which we seek the kernel which embodies the boundary conditions on a tube and a support plate and complete an efficient calculation of the probe response to cracks in a tube near a support plate.

6.2 Recommendations for Future Research

Transient (or pulsed) eddy current testing is widely used to detect and size the surface and subsurface flaws of conductive test pieces due to its broadband signal and it is simple, cheap and convenient in practice. The investigation of transient eddy current probe on layered planar structures has been developed using both analytical and numerical methods. It has been widely applied to the pipeline inspection in power plants, oil and gas transmissions, etc. In most cases, the pipes can be treated as layered plates if the dimension of pipes is much bigger than the coil whose axis is perpendicular to the surface of the pipe. To inspect the whole section of the pipe, the coil has to be moved around the pipe multiple times, which is very time consuming for a long and big pipe. Furthermore it is likely to leave some area uninspected and is not suitable for thin pipe. Fortunately, if the time domain expression of the field due to a transient eddy current coil encircling an arbitrary layered rod, Figure 6.1, can be derived, it will be helpful to offer a quick, convenient and reliable method for pipelines inspection.

As mentioned in Chapter 4, ferrite-cored coils have better signal-to-noise ratio and higher

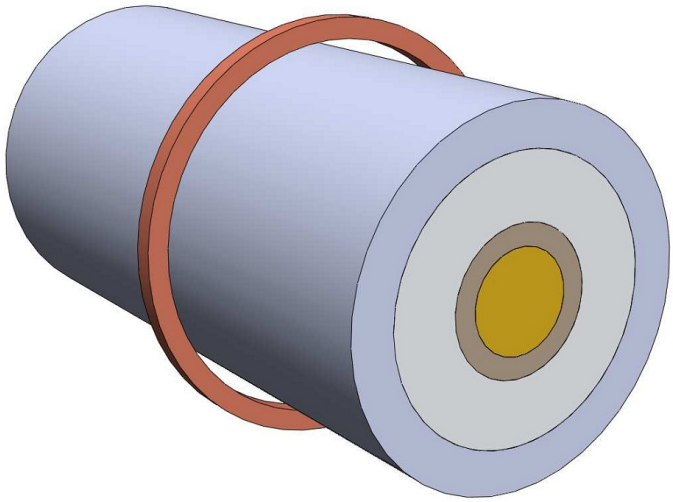

Figure 6.1 A uniformly layered conducting rod of infinite length encircled by a co-axial coil with rectangular cross-section.

detection resolution for crack or corrosion inspections. The model of the ferrite-cored probe due to a surface or subsurface crack in a conductive plate will be investigated in near future. Some experiments and simulations by FEM have been done, experiments configurations as shown in Figure 6.2. Good agreement between numerical results of FEM and experiments data is observed in Figure 6.3 which also shows the ferrite-cored probe has much better performance during the inspection. In addition, this approach can be extended to be applied for other more complicated axisymmetric ferrite core shaped probes, such as in Figure 6.4.

The semi-analytical solution of the field and eddy current probe response in present of the tube and support plate have been derived. Based on this, we can compute the coil impedance variation due to the flaw using discrete volume elements in the flaw region only accurately and efficiently, though usually the surrounding support plate generates much stronger signals in the differential bobbin coil (or rotary pancake coil), which can mask the signals due to the nearby flaws in the tube, as shown in Figure 6.5. Similar method has been used in the problem of a rotary pancake pick-up coil signal change due to a crack in a tube. Furthermore, we will investigate the response of a rotary pancake coil due to a crack in a tube with the presence of a support plate in Figure 6.6.

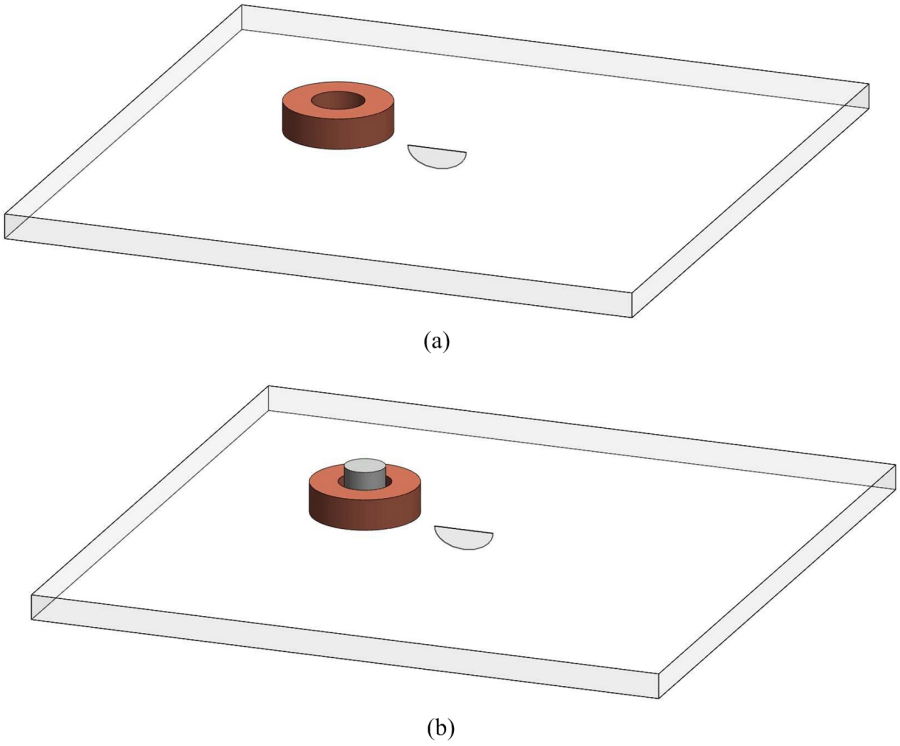

Figure 6.2 Air-cored and ferrite-cored coils scanning a semi-elliptical crack in a conductive plate.

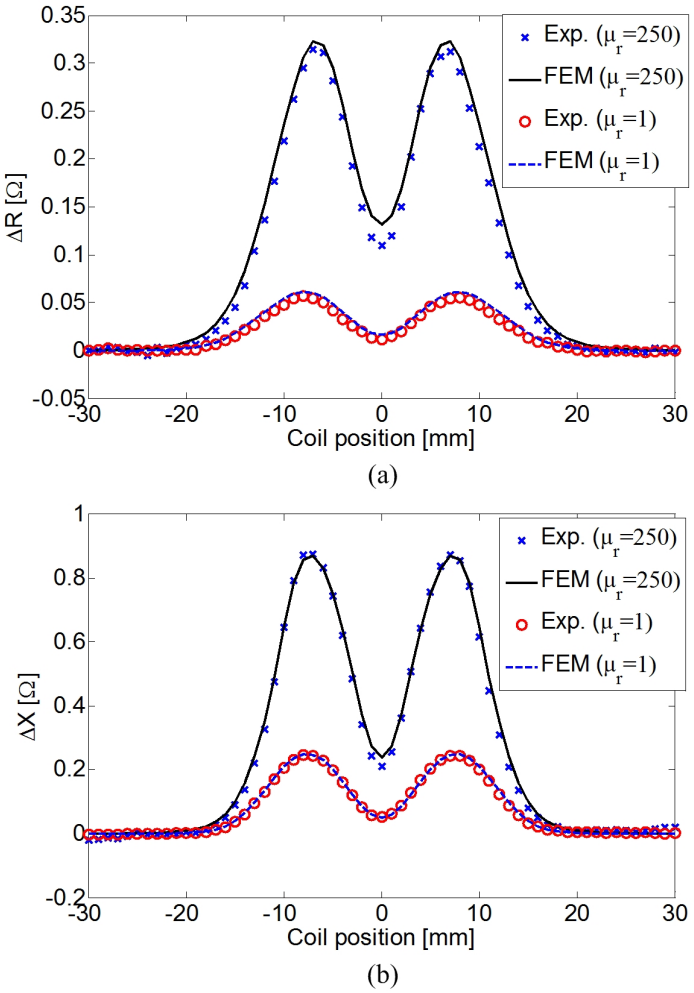

Figure 6.3 Impedance change of air-cored and ferrite-cored coils due to a semi-elliptical crack in a conductive plate as a function of coil position at 10 kHz.

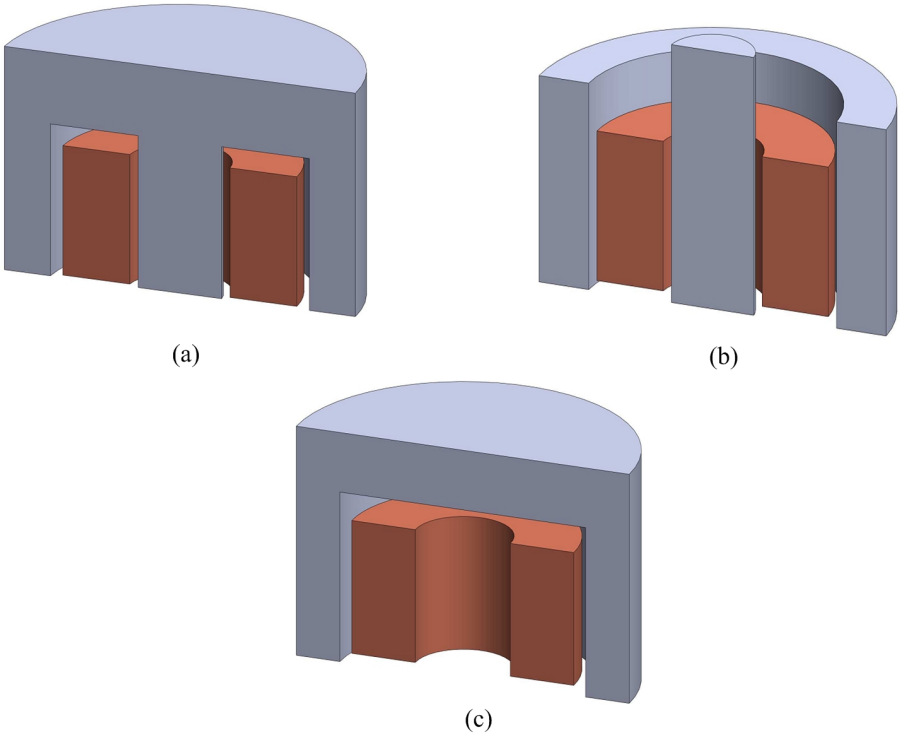

Figure 6.4 Other axisymmetric ferrite core shaped probes.

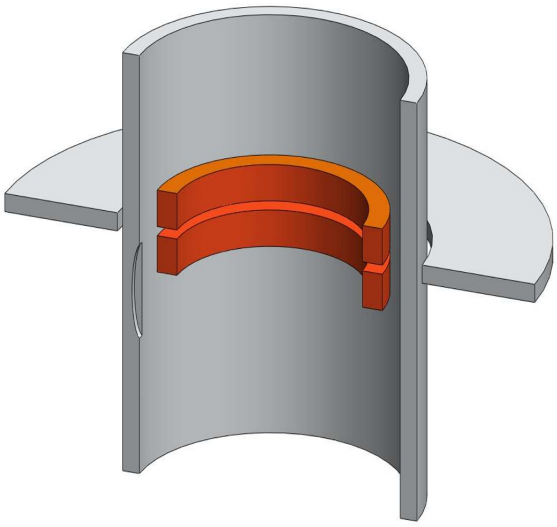

Figure 6.5 Differential bobbin coil inside a tube with a crack adjacent to a support plate.

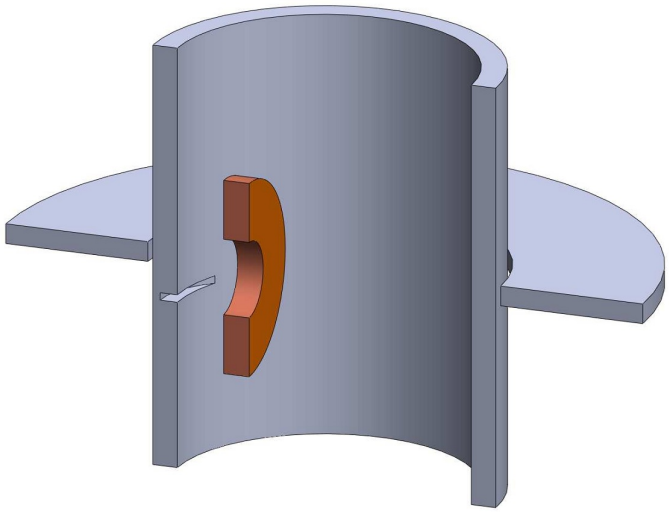

Figure 6.6 Rotary pancake coil inside a tube with a crack near to a support plate.

APPENDIX A. EDGE EFFECTS IN FOUR POINT DIRECT CURRENT POTENTIAL DROP MEASUREMENT

A paper published in *The Review of Progress in Quantitative Nondestructive Evaluation*

Yi Lu, John R. Bowler, Chongxue Zhang and Nicola Bowler

Abstract

The four point direct current potential drop (DCPD) technique is used to measure electrical conductivity and crack depth. It is also used, together with Hall voltage measurements, to evaluate carrier concentration and mobility in semiconductors. Here the theory of DCPD is studied for planar structures in which edge effects may have to be taken into account and correction made to ensure accuracy. The current injected at a point on the surface of an infinite plate of finite thickness gives rise to a field that can be expressed as a summation derived using image theory. Because the images are periodic in the direction perpendicular to the plate surface, the field can also be conveniently expressed in the form of a Fourier series. The two basic formulas; image summation and Fourier series, can be modified for the case where the probe points are near the edge of a plate by further applying image theory and summing image/Fourier terms in two dimensions. Both of these approaches agree with measurement results very well.

Introduction

The direct current potential drop (DCPD) technique is widely used to characterize electrical conductivity of materials in the semiconductor industry (1), in biomedical research (2) and in geophysical applications (3). Compared with other measurement methods such as eddy-current

technology (ECT), DCPD can be applied to measure the conductivity of ferrous metals, being independent of magnetic permeability. Since the measured signal is inversely proportional to the conductivity, a good signal-to-noise ratio can be guaranteed for low-conductivity materials such as semiconductors and geophysical specimens. For DCPD measurements, the four-point probe is one of the most common probe configurations used in practice. Often, although not necessarily, the probe points are arranged in a straight line as shown in Figure A.1. Generally, the current is injected and extracted via the outer two pins (P_1 and P_2) and the floating potential drop is measured across the inner two pins (Q_1 and Q_2) with a high input impedance circuit. When the probe is sufficiently far from the boundary of the specimen (eight or nine times the probe length (4)), the current distribution is not significantly disturbed by the boundary. When the probe is close to the boundary, however, the current can be significantly distorted which results in an increase in the measured potential drop. So, even for a uniformly thick specimen, different voltages can be measured at different probe positions. Figure A.2 shows the relative difference between voltages measured experimentally at the center and near the edge of a large thin plate. The detailed parameters for both the plate and probe utilized in this experiment can be found in Table A.1.

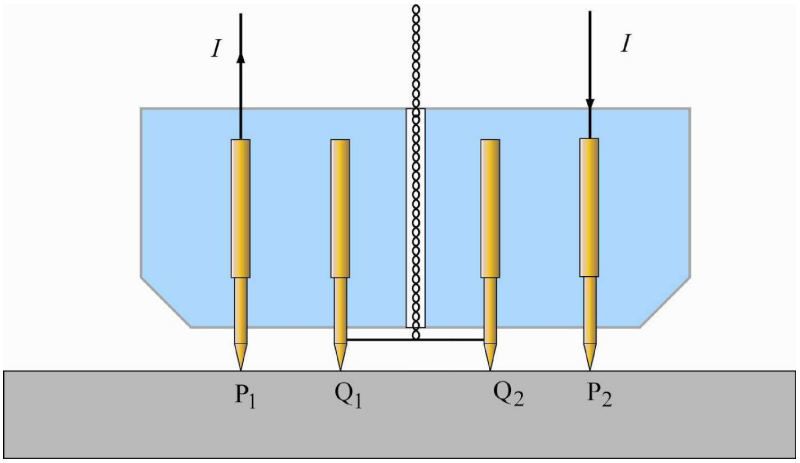

Figure A.1 Co-linear four-point-probe configuration in DCPD system.

For the purpose of modelling the edge effect in four-point DCPD measurements, several approaches have been brought forward. A solution via conformal transformation (5) assumes that the specimen is thin compared to the probe spacing. An analytical solution of the Poisson

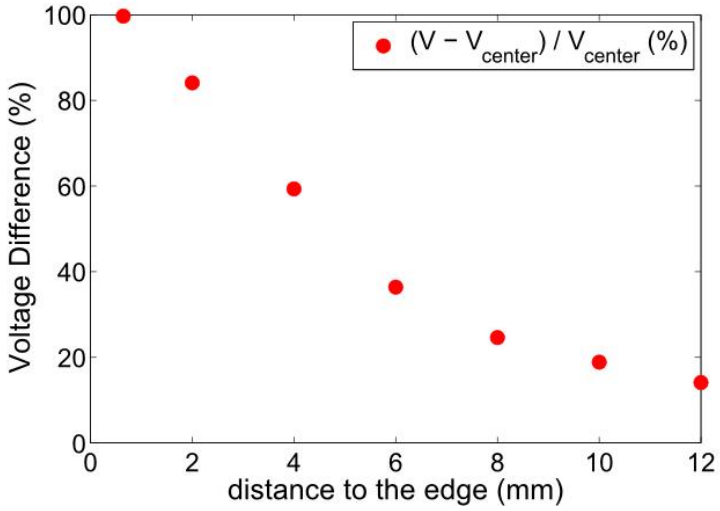

Figure A.2 Voltage relative difference between experimental results with edge effect and center point in a large thin plate.

Table A.1 Probe and plate parameters corresponding to the data shown in Figure 2. L is the separation of the current-carrying electrodes. P is the separation of the voltage pick-up electrodes.

Probe parameters	
L (mm)	18.009 ± 0.003
P (mm)	6.035 ± 0.003
Plate parameters	
Width (mm)	412
Length (mm)	412
Thickness (mm)	1.57 ± 0.01
Conductivity (MS/m)	5.50 ± 0.04

equation given in reference (6) does not restrict the thickness of the specimen, but the form of the solution is complex and the convergence of the solution is poor for thick samples. A conventional method-of-images solution (7) yields a simple and elegant solution form, but generally converges slowly if at least one dimension of the specimen is small relative to the probe spacing. To improve upon numerical calculation of slowly converging infinite summations, Uhlir (8) evaluated some auxiliary functions and tabulated the potentials of several simple image systems, for ease of reference.

This paper focuses on establishing a theoretical model for the situation in which the probe

is close to one edge of a large plate with arbitrary thickness. Previously, an analytical solution for the electric field distribution in a half-space conductor has been formulated in terms of a transverse magnetic (TM) potential (9). Subsequently, the AC potential drop on the surface of a metal half-space was derived and compared with experimental results (10). The electric field distribution in a homogeneous conductive plate with uniform thickness was also solved analytically (11) and good agreement with measured AC potential drop was obtained (12). Here, the method of images is applied to model the edge effect in four-point DCPD and the solution form is simple and elegant. To overcome the mentioned disadvantage of slow convergence, a Fourier Series representation has been employed to obtain much faster convergence for plates thinner than the probe dimension.

Theory

The theoretical model presented here makes some approximations. First, the connecting wires are represented as filaments. Secondly, current and voltage contacts are modelled as infinitesimal points on the specimen surface, which is flat. Last, the plate is homogeneous, isotropic and has linear material properties. These approximations are shown to be reasonable since the theory agrees well with experimental data as shown later.

Half-space Conductor

First, consider the simple problem shown in Figure A.3. Direct current I is injected into a half-space conductor at point P and diverges uniformly. This gives rise to the potential Φ for a point in the conductor given by

$$\Phi = \frac{I}{2\pi\sigma R}, \tag{A.1}$$

where σ is the conductivity of the conductor and $R = \sqrt{(x-x')^2 + (y-y')^2 + (z-z')^2}$ is the distance from the injection point. Unprimed coordinates represent field points and the source coordinates are primed. Choosing the origin of the coordinate system at the surface of the conductor means that $z = z' = 0$ and $R = \rho = \sqrt{(x-x')^2 + (y-y')^2}$.

In four-point probe problem, the potential at one point is the superposition of potentials

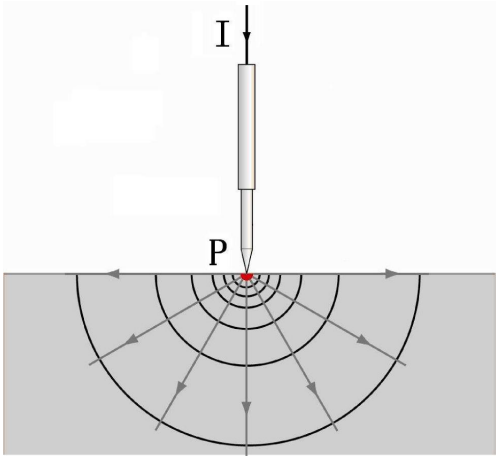

Figure A.3 Injection of DC current at the surface of a half-space conductor.

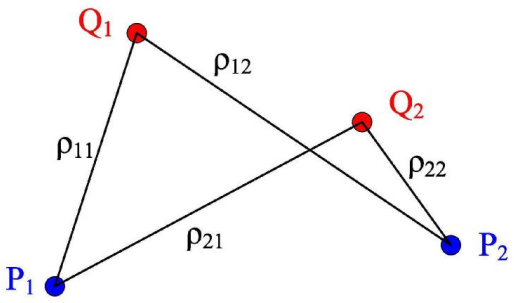

Figure A.4 Contact points for current (P_i) and voltage (Q_i) electrodes on the surface of a planar specimen (plan view).

due to both injected and extracted currents. So, the potential of a field point Q due to a source of current at P_2 and a sink of current at P_1 on the surface is

$$\Phi(\rho) = \frac{I}{2\pi\sigma} f(\rho), \tag{A.2}$$

with

$$f(\rho) = \frac{1}{\rho_2} - \frac{1}{\rho_1}, \tag{A.3}$$

where $\rho_i = |\bar{Q} - \bar{P}_i| = \sqrt{(x - x_i')^2 + (y - y_i')^2}$ and $i = 1, 2$. In addition, the potential drop V between two points Q_1 and Q_2 on the surface of the specimen due to the current through P_1 and P_2, as shown in Figure A.4, can be written with the general form

$$V = \Phi_{Q_2} - \Phi_{Q_1} = \frac{I}{2\pi\sigma} [f_2(\rho) - f_1(\rho)], \tag{A.4}$$

where

$$f_i(\rho) = \frac{1}{\rho_{i2}} - \frac{1}{\rho_{i1}}, \tag{A.5}$$

$\rho_{ij} = |\bar{Q}_i - \bar{P}_j| = \sqrt{\left(x_i - x'_j\right)^2 + \left(y_i - y'_j\right)^2}$ and $i, j = 1, 2$.

Conductor with Finite Thickness

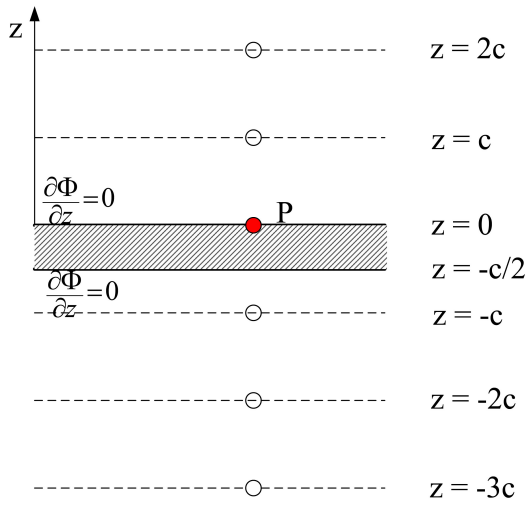

Figure A.5 Images for an infinite plate with finite thickness c/2.

In the half-space problem, the potential due to a single injected current is given by equation (A.1), which satisfies the Von Neumann boundary condition $\partial\Phi/\partial z = 0$ on the surface of the conductor, away from the current injection point. For a large plate of thickness $c/2$ whose upper surface is in the plane $z = 0$, Figure A.5, there is an additional but similar boundary condition at $z = -c/2$. The method of images is employed to satisfy the conditions on both of these surfaces.

Placing an image source at $z = -c$ of the same polarity as the actual source, yields two opposing currents whose z-components exactly balance in the $z = -c/2$ plane. Thus, with one image source added, the Von Neumann boundary condition at $z = -c/2$ is satisfied. But, the boundary condition at $z = 0$ is no longer satisfied because of the effect of the image source. This effect can be balanced by introducing another image source with the same polarity at $z = c$. In fact it is necessary to add images in this way in both positive and negative z-directions out

to infinity. Finally, the images of a current source at P occupy positions with period c in the z-direction as shown in Figure A.5.

From the method of images, a source at P_2 and a sink at P_1 give rise to a potential at Q on the surface that is a generalization of equation (A.3);

$$f(\rho) = \sum_{n=-\infty}^{+\infty} \left[\frac{1}{\sqrt{\rho_2^2 + (nc)^2}} - \frac{1}{\sqrt{\rho_1^2 + (nc)^2}} \right], \tag{A.6}$$

where $\rho_i = |\bar{Q} - \bar{P}_i| = \sqrt{(x - x_i')^2 + (y - y_i')^2}$, $i = 1, 2$ and the potential drop can be evaluated as in equation (A.4). Note, when $c \to \infty$ only the term with $n = 0$ survives in the summations and we obtain

$$f(\rho) = \sum_{n=-\infty}^{+\infty} \left[\frac{1}{\sqrt{\rho_2^2 + (nc)^2}} - \frac{1}{\sqrt{\rho_1^2 + (nc)^2}} \right] \to \left(\frac{1}{\rho_2} - \frac{1}{\rho_1} \right) \tag{A.7}$$

which agrees with the half-space result (A.3).

For numerical evaluation, the sum in equation (A.7) must be approximated by truncating at a finite number of terms. In the case of a thick plate the number of terms needed for good convergence is relatively small, whereas a large number of terms is necessary in the case of a thin plate due to the slow convergence of the summation for thin plates.

Conductor with Finite Thickness and One Edge

When applying the method of images to obtain a solution for the measured potential drop when the probe is near an edge of a conductive plate, it is necessary to satisfy the Von Neumann boundary condition on the three surfaces of the conductor. Let the surfaces be at ($0 \le y \le \infty$, $z = 0$), ($0 \le y \le \infty$, $z = -c/2$) and ($-c/2 \le z \le 0$, $y = 0$), as shown in Figure 6. First, balance the actual source with an image source of the same polarity placed symmetrically on the y-axis. Then, by the argument of the previous section, there are two corresponding groups of images aligned in the z-direction with period c as introduced in Figure A.5. Thus the potential at a field point Q due to a current source and sink on the surface $z = 0$ can be written as a generalization of equation (A.6):

$$f(\rho) = \sum_{j=1}^{2} \sum_{n=-\infty}^{\infty} \left[\frac{1}{\sqrt{\rho_{j2}^2 + (nc)^2}} - \frac{1}{\sqrt{\rho_{j1}^2 + (nc)^2}} \right]. \tag{A.8}$$

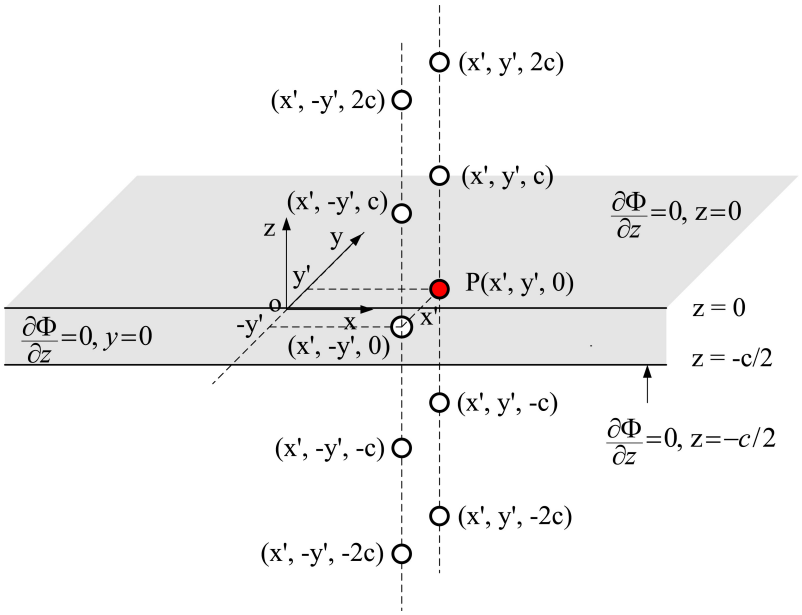

Figure A.6 Images when close to an edge of a large plate with finite thickness.

Here, $\rho_{jk} = \sqrt{(x - x'_k)^2 + \left[y - (-1)^j y'_k\right]^2}$ with $j, k = 1, 2$. Again, by using equation (A.4) the potential drop can be obtained. In the limiting case $0 \le y \le +\infty$, $y' \to +\infty$

$$f(\rho) \approx \sum_{n=-\infty}^{+\infty} \frac{1}{\sqrt{(x - x'_2)^2 + (y - y'_2)^2 + (nc)^2}} - \sum_{n=-\infty}^{+\infty} \frac{1}{\sqrt{(x - x'_1)^2 + (y - y'_1)^2 + (nc)^2}}$$
$$= \sum_{n=-\infty}^{+\infty} \left[\frac{1}{\sqrt{\rho_2^2 + (nc)^2}} - \frac{1}{\sqrt{\rho_1^2 + (nc)^2}} \right] \quad \text{(A.9)}$$

where $\rho_i = |\bar{Q} - \bar{P}_i| = \sqrt{(x - x'_i)^2 + (y - y'_i)^2}$, $i = 1, 2$, we obtain agreement with the case for a large plate of finite thickness, equation (A.6).

Fourier Series Representation

The infinite summations (A.6) and (A.8) do not converge very quickly for a plate that is thinner than the spacing of the probe points. Convergence can be improved by adopting a Fourier series representation for the infinite sum. The location of the current source and its images shown in Figures A.5 and A.6 exhibit periodicity in the direction perpendicular to the

plate surface, z, with period c. This means that the following identity (13) can be used:

$$\sum_{n=-\infty}^{+\infty} \frac{\exp\left[-\alpha\sqrt{\rho^2+(z-nc)^2}\right]}{\sqrt{\rho^2+(z-nc)^2}} = \frac{2}{c}K_0(\alpha\rho) + \frac{4}{c}\sum_{m=1}^{+\infty} K_0\left[\rho\sqrt{\alpha^2+(2\pi m/c)^2}\right]\cos(2\pi mz/c), \tag{A.10}$$

in which $K_0(x)$ is the modified Bessel function of the second kind of order zero. Putting $z = 0$ in (A.10), equation (A.6) can be transformed to obtain

$$f(\rho) = \frac{2}{c}\ln(\rho_1/\rho_2) + \frac{4}{c}\sum_{m=1}^{+\infty}\{K_0[(\rho_2/c)\,2\pi m] - K_0[(\rho_1/c)\,2\pi m]\}. \tag{A.11}$$

Relation (A.10) was also used in the theory of four-point alternating current potential drop on a metal plate (14). Results (A.6) and (A.11) provide alternative means of evaluating the potential drop measured between pick-up points of a four-point probe on the surface of a metal plate. The infinite sum in equation (A.8) can be transformed similarly, to give the following result for a plate with finite thickness and an edge,

$$f(\rho) = \sum_{j=1}^{2}\left\{\frac{2}{c}\ln(\rho_{j1}/\rho_{j2}) + \frac{4}{c}\sum_{m=1}^{+\infty}[K_0(2\pi m\rho_{j2}/c) - K_0(2\pi m\rho_{j1}/c)]\right\}. \tag{A.12}$$

Figure A.7 compares the convergence of equation (A.11) with that of equation (A.6) for a case in which the probe length is 8 times the plate thickness ($L = \rho_1 + \rho_2 = 8c$). In general,

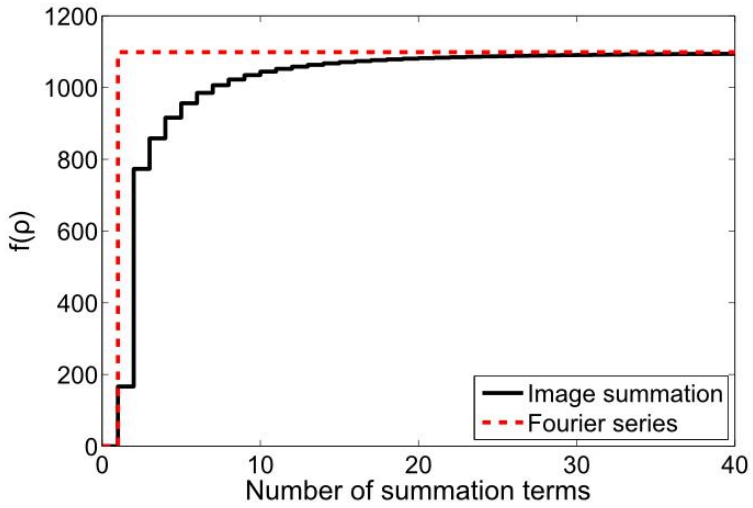

Figure A.7 Image summation (A.6) converges slowly compared with Fourier series representation (A.11) in this case where $\rho_1 = 6c$, $\rho_2 = 2c$, $c = 2mm$.

equation (A.11) is much more efficient for computing the potential in the case of a plate with thickness smaller than the probe point separation.

Limiting Case of A Thin Plate

It is possible to show that only the first term on the right-hand side of equation (A.11) is significant when the plate thickness $c/2$ is significantly smaller than the separation between the probe points ρ_i. For large argument x, the following asymptotic expansion for $K_0(x)$ (15) holds:

$$K_0(x) \sim \sqrt{\frac{\pi}{2x}} e^{-x} \left(1 - \frac{1}{8x} + \ldots\right), \qquad x \gg 0. \tag{A.13}$$

The exponential factor including the dimensionless parameter ρ/c is sufficient to make the summation significantly smaller than the first term in equation (A.12) when $\rho/c \gg 1$ and

$$f(\rho) \approx \frac{2}{c} \ln(\rho_1/\rho_2), \qquad \rho/c \gg 1. \tag{A.14}$$

This result agrees with that shown in reference (16), which followed the work of Uhlir (8).

Experiment

A co-linear symmetric four-point-probe measurement system was designed to verify the theory, as shown in the schematic diagram Figure A.1. Four sprung, point contacts were mounted in a plastic support block, perpendicular to the surface of a large spring-steel plate. The pin separations were measured with a travelling microscope. Parameters of the plate and probe are listed in Table A.1.

In the experiment, a low-frequency alternating current was used rather than direct current, due to several experimental advantages. Full experimental details are given in reference (12), where it is shown that the DC theory is valid for AC when the frequency is below a certain value that depends on the experimental parameters.

In order to validate the theory, both the current through the probe and voltage drop between the pick-up probes must be measured. The first can be can be monitored by measuring the voltage drop across a precision resistor in series with the drive circuit. The latter can be measured by a high input impedance circuit. Values of DCPD both in the center and close

to one edge of the plate were measured, with the probe oriented parallel to the edge. The experimental data are compared with theory in Figure A.8. In the figure, an obvious edge effect is observed and good agreement between theory and experimental data shows that the edge effect is accurately predicted by the theory.

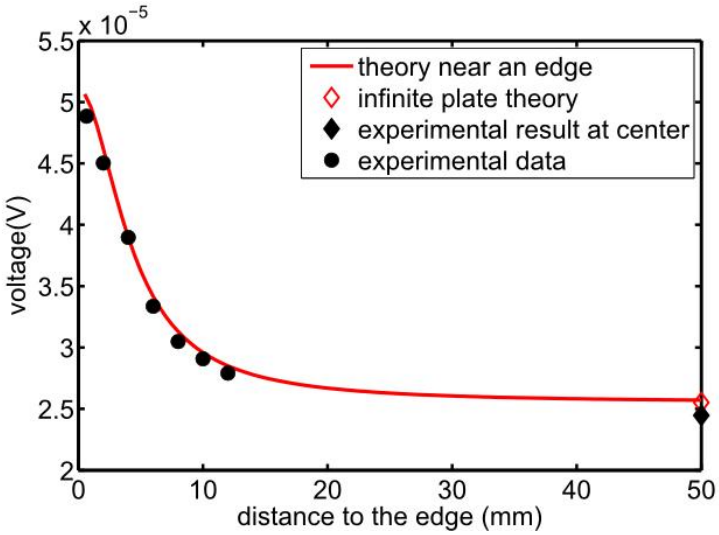

Figure A.8 Comparison between theory and experimental data. Edge effect theory is got from equation (A.14) and the infinite plate theory from equation (A.11).

Conclusion

In this paper, an analytical solution has been presented to model edge effects in DCPD measurements on metal plates with finite thickness. A method-of-images solution converges quickly for plates somewhat thicker than the probe dimensions. A Fourier series summation converges more quickly for thinner plates. In future work, DCPD for finite rectangular blocks and layered cylindrical samples will be studied.

Acknowledgment

This work was supported by the NSF Industry/University Cooperative Research program at Iowa State University's Center for Nondestructive Evaluation.

References

[1] Schroder D K 1998 *Semiconductor Material and Device Characterization* (New York: Wiley)

[2] Wang Y, Schimpf P, Haynor D and Kim Y 1998 Geometric effects on resistivity measurements with four-electrode probes in isotropic and anisotropic tissues *IEEE Trans. BioMed Eng.* **45** 877–84

[3] Parasnis D S 1997 *Principles of Applied Geophysics 5th edn* (London: Chapman and Hall)

[4] Bowler N and Huang Y 2005 *Four-point alternating current potential drop measurements on metal plates: experiment and interpretation*, Center for Nondestructive Evaluation, Iowa State University, Ames, Iowa. Unpublished.

[5] Perloff D S 1977 Four-point sheet resistance correction factors for thin rectangular samples *Solid State Electron.* **20** 681–7

[6] Yamashita M and Agu M 1984 Geometrical correction factor for semiconductor resistivity measurements by four-point probe method *Jpn. J. Appl. Phys.* **23** 1499–504

[7] Valdes L B 1954 Resistivity measurements on germanium for transistors *Proc. IRE* **42** 420–7

[8] Uhlir A 1955 The potentials of infinite systems of sources and numerical solutions of problems in semiconductor engineering *Bell Syst. Tech. J* **34** 105–28

[9] Bowler N 2004 Analytical solution for the electric field in a half space conductor due to alternating current injected at the surface *J. Appl. Phys.* **95** 344–8

[10] Bowler N 2006 Theory of four-point alternating current potential drop measurements on a metal half-space *J. Phys. D Appl. Phys.* **39** 584–9

[11] Bowler N 2004 Electric field due to alternating current injected at the surface of a metal plate *J. Appl. Phys.* **96** 4607–13

[12] Bowler N and Huang Y 2005 Model-based characterization of homogeneous metal plates by four-point alternating current potential drop measurements *IEEE Trans. Mag.* **41** 2102–10

[13] Sperb R 1996 An alternative to Ewald sums part I: identities for sums *Molecular Simulation* **20** 179-200

[14] Bowler J R and Bowler N 2007 Theory of four-point alternating current potential drop measurements on conductive plates *Proc. R. Soc. A* **463** 817–36

[15] Jeffery A and Dai H (ed) 2008 *Handbook of Mathematical Formulas and Integrals* 4th edn (London: Academic Press)

[16] Bowler N 2006 Theory of four-point direct-current potential drop measurements on a metal plate *Res. Nondestr. Eval.* **17** 29–48

ACKNOWLEDGEMENTS

It would not be possible for me to complete this doctoral dissertation without the supports from several people and I would like to express my sincere gratitude for all of them.

First of all, I want to express my deeply-felt thanks to my advisor, Dr. John Bowler, for your constant and thoughtful guidance and warm encouragement during my Ph.D. program. Your in-depth knowledge on a broad spectrum of electromagnetic theories, abilities to select and attack challenging research problems, and high scientific standards set an example for me. Your joys and enthusiasm for the research was also great motivation for me.

I would also like to thank Dr. Nicola Bowler and Dr. Jiming Song, my committee members and instructors for several electromagnetic courses, for the substantial influences that your courses which have had on my research work. And also Dr. Nicola Bowlers kind encouragement and constructive suggestions for my future research career helped me a lot.

I would also like to thank Dr. Jaeyoun Kim and Dr. Gary Tuttle, who served as my committee members, for your time, interests, helpful comments and insightful questions.

I am appreciative of my fellow graduate classmates, Hui Xie, Yuan Ji, Fu-gang Hu, Yifen Liu, Yu Liu, Tianming Chen, Yang Li, Teng Zhao and Hongsheng Xu, for the friendship and camaraderie, making my study life time at Iowa State a more enjoyable life.

Lastly, I am very indebted to my family, brother and my husband, you have always provided encouragement and support at the every stage of my life.

To all of you, thank you.